

無曰己是 無曰遂真

靡革匪因 靡故匪新

馬一浮 (1883-1967)

*Say not that ye have attained the absolute perfection*

*Say not that ye have exhausted the quest for truth*

*There is no change that does not involve inheritance*

*There is nothing established that does not entail renovation*

*Yifu Ma (1883-1967)*

**University of Alberta**

**DNA ELECTROPHORESIS IN  
COLLOIDAL SELF-ASSEMBLED ARRAYS**

by

Wenmin Ye

A thesis submitted to the Faculty of Graduate Studies and Research  
in partial fulfillment of the requirements for the degree of

Doctor of Philosophy

Department of Chemistry

©Wenmin Ye  
Spring 2013  
Edmonton, Alberta

Permission is hereby granted to the University of Alberta Libraries to reproduce single copies of this thesis and to lend or sell such copies for private, scholarly or scientific research purposes only. Where the thesis is converted to, or otherwise made available in digital form, the University of Alberta will advise potential users of the thesis of these terms.

The author reserves all other publication and other rights in association with the copyright in the thesis and, except as herein before provided, neither the thesis nor any substantial portion thereof may be printed or otherwise reproduced in any material form whatsoever without the author's prior written permission.

To my parents and grandparents

# Abstract

---

This thesis investigates electrophoretic separation of DNA molecules in different types of separation media formed by silica nanoparticles. Particle arrays within microfluidic chips are fabricated using evaporation induced colloidal self-assembly. Methods to adjust pore size and the order of the particle lattice were developed, in order to probe the effect of lattice structure and size on separation of DNA.

A stepwise packing procedure was developed to fabricate structures with stepwise gradient in pore size. Monodisperse packed structures yield pore sizes from a few nanometers to a few hundred nanometers according to the particle size being used, but the electrophoresis can only be optimized for a certain range of DNA sizes. By packing separation zones with two different pore sizes, optimal separation can be achieved for larger and smaller DNA size range, by taking advantages from both larger and smaller pore sizes within one device. The separation accomplished in the upstream region is retained as DNA moves across the zone boundary, even when the separated DNA has the same deflection angle in the downstream region. Small DNA not separated in the larger pore size is then separated in the smaller, downstream pore size. The peak capacity is improved by employment of this stepwise pore gradient.

Colloidal arrays with two different sized nanoparticles mixed in various proportions are prepared, yielding structures with different degrees of disorder. The roles of order within a separation matrix on DNA separation in both asymmetric pulsed field angular separation and capillary zone electrophoresis are studied systematically. Radial distribution functions and orientational order parameters are determined to characterize the scale of disorder.

In pulsed field electrophoresis, the DNA separation resolution is quantified for each structure, showing a strong dependence on order within the structure. Ordered structures give better separation resolution than highly disordered structures. However, the variation of separation performance with order is not monotonic, showing a small, but statistically significant improvement in structures with short range order compared to those with long range order.

In capillary zone electrophoresis, regression analysis is conducted for the electrophoretic mobility and the dispersion coefficient. Both parameters exhibit a weak monotonic dependence on matrix order, complementary to the effect of DNA size and pore size. Higher degree of matrix order is favored by higher mobility and lower dispersion coefficient.

# Acknowledgement

---

While writing this section, I am short of words to express my sincere gratitude to a number of people for their support and help over the last four years. My research and life in a new country and culture would not have been such an amazing and unforgettable journey without any one of them.

I feel blessed to have the chance to be a student of Dr. Jed Harrison, the brightest scientists I have ever met. His sharp inspiration, insightful instruction and integrated understanding of multidisciplinary concepts impressed me deeply. His unreserved support and enthusiastic encourage always reassured me from hesitation. His support for my attendance at international conferences offered me excellent opportunities for networking with ingenuities all over the world. His trust and consideration for his students, attitude towards career, and keen sense of humor have become the patterns I'm willing to follow. All of the above will be the priceless asset to my future career development.

I sincerely appreciate the guidance and suggestions from all my supervisory committee members, Professors Charles Lucy, Jonathan Veinot, and Mark McDermott. I learned from them invaluable skill of communication, the understanding of bigger picture in the horizon, and the enthusiasm for outreach. I also thank Prof. Niles Petersen for reviewing my

thesis and serving in my defence, Prof. Subir Bhattacharjee for his insightful comments during my candidacy exam, and Prof. Chong Ahn for the willingness to come to Edmonton as the external examiner in my defence.

I would like to acknowledge NSERC and Alberta Ingenuity Scholarship in Nanotechnology for funding our research. I like to thank the financial support from the Department of Chemistry, the Faculty of Graduate Studies and Research, and the Graduate Student Association, to grant my expenses of living and conference travels. I thank the Nanofab, NINT and NIRF for providing facilities and instruments needed in my experiments, as well as the staff in the general office, electronic and glass shop, and IT service for their kind help.

I am thankful to my lab mates and friends for making my study easier and interesting. I thank Dr. Neda Nazemifard and Ledi Wang who collaborated with me throughout the first two years of my research, especially Neda for her mentorship and inspiration as a senior graduate student. I thank all my group members, previous and recent: Dr. James Bao, Dr. Yajuan Hua, Dr. Qingye Lu, Dr. Josh Wasylcia, Dr. Amr Mahmoud, Huiying Sheng, Chen Peng, Reshma Singh, Hamid Ramezani, Narges Shaabani, Ali Malekpour Kourpaei, Yongxin Zhao, Mohammad Azim, Ya Zhou, and Le Zhang, for their helpful discussions in group meetings and the lab. I also wish to acknowledge all other friends I met here. You all have

made my life in Edmonton full of fun and color.

No words can fully express my gratitude to my parents, grandparents, other family members and beloved ones for their understanding and sacrifice. They have been doing all they can do to support me and ask nothing in return. Their selfless love and constant encouragement are always beside me through ups and downs of life, no matter where they are physically.

# Contents

---

<b>Chapter 1 Introduction .....</b>	<b>1</b>
1.1 Background and Motivation .....	1
1.1.1 Introduction .....	1
1.1.2 Scope of the Thesis.....	5
1.2 Polymer Physics .....	6
1.2.1 DNA Conformation in Free Solutions.....	6
1.2.2 DNA Conformation in Confinements .....	13
1.3 Electrophoresis of DNA .....	16
1.3.1 Fundamentals of Electrophoresis .....	16
1.3.2 DNA Migration Mechanisms .....	20
1.4 Separation Techniques.....	37
1.4.1 Gel Electrophoresis.....	37
1.4.2 Capillary Electrophoresis .....	39
1.4.3 Micro-fluidic Devices.....	41
1.5 References .....	49
<b>Chapter 2 DNA Electrophoresis in Nanoparticle Arrays with Pore Size Gradient.....</b>	<b>60</b>
2.1 Introduction .....	60
2.2 Experimental.....	62

2.2.1	DNA separation microchip.....	62
2.2.2	Asymmetric pulsed field electrophoresis .....	64
2.3	Results and discussion .....	66
2.3.1	Angular separation in monodisperse CSA .....	66
2.3.2	Characterization of particle arrays.....	68
2.3.3	Angular separation within pore size gradient.....	69
2.4	Conclusions .....	74
2.5	References .....	74

**Chapter 3 The Effect of Disorder on DNA Pulsed Field Electrophoresis**  
..... **76**

3.1	Introduction .....	76
3.2	Experimental Section.....	80
3.2.1	DNA Separation .....	80
3.2.2	Self-assembled Nanoparticle Array Structures .....	83
3.3	Results and Discussion .....	83
3.3.1	Characterization of the Packed Structures.....	84
3.3.2	DNA Separation .....	88
3.4	Conclusions .....	97
3.5	References .....	99

**Chapter 4 The Effect of Media Order in DNA Capillary Zone**  
**Electrophoresis** ..... **103**

4.1	Introduction .....	103
-----	--------------------	-----

4.2	Experimental.....	107
4.2.1	Microfluidic chip fabrication.....	107
4.2.2	DNA Zone Electrophoresis Experiment.....	110
4.2.3	Differential Scanning Calorimetry (DSC).....	111
4.3	Results and Discussion .....	112
4.3.1	Characterization of the Matrix Order .....	112
4.3.2	Model of Pore Size Distribution for Binary Packed Structures .....	115
4.3.3	Thermoporosimetry .....	118
4.3.4	Porosity and the Accessible Fraction .....	125
4.3.5	DNA Electrophoretic Mobility.....	129
4.3.6	Dispersion Coefficient.....	134
4.4	Conclusions .....	139
4.5	References .....	144
	<b>Chapter 5 Conclusions and Future Work.....</b>	<b>152</b>
5.1	Concluding Remarks .....	152
5.2	Future Work.....	155
	<b>Appendix Experimental Setup .....</b>	<b>159</b>
A.1	Generating Pulsed Electric Field.....	159
A.2	Generating of DC Field .....	159
A.3	Fluorescent Microscopy .....	159

# List of Tables

---

<b>Table 4.1.</b> Probability and scales of five types of subunits combinations. .....	116
<b>Table 4.2.</b> Regression results of equation 4.19.....	131
<b>Table 4.3.</b> Regression results of equation 4.28.....	139

# List of Figures

---

**Figure 1.1.** Schematic of models of polymer chain. a) DNA in a free solution as a coiled molecule. b) Freely-jointed-chain model. c) Worm-like chain model. d) Rouse bead-spring model. .... 10

**Figure 1.2.** Conformation of a DNA in a) the de Gennes regime, and b) the Odijk regime..... 15

**Figure 1.3.** a) Schematic of an electric double layer around a negatively charged particle in an electrolyte solution. b) Electrophoresis of a negatively charged particle in an electrolyte solution with negatively charged substrate. .... 17

**Figure 1.4.** Three regimes of DNA electrophoresis. a) Ogston sieving, where the pore size in the separation media is larger than the DNA coil size. b) Entropic trapping, where the size of pores in the separation media is around the DNA coil size. c) Reptation regime, where the pore size is much smaller than the DNA coil size. Molecule 1 illustrates reptation with orientation. Hernia and hooking are shown by molecules 2 and 3 respectively..... 23

**Figure 1.5.** Schematic of migration mechanism of DNA in a porous media. Grey arrows indicate directions of net motion. a) The zigzag type motion with one leading head under symmetric pulsed electric fields with an acute

angle. b) The chevron type motion with periodically changing head and tail under symmetric pulsed electric fields with an obtuse angle. c) The ratchet type backtracking motion under asymmetric electric fields..... 31

**Figure 1.6.** a) Schematic of several typical collisions of DNA with a single post. b) The geometration of long DNA in obstacle array with small gaps. .... 36

**Figure 1.7.** Schematic illustration of the general fabrication procedure of a) Si/glass chips, and b) PDMS chips..... 43

**Figure 1.8.** Microfabricated devices for DNA separation. a) Devices with nanopost or nanowall array;[139] b) Anisotropic array for continuous separation by entropic trapping;[141] c) An entropic recoil separation in a dense post array under pulsed field;[131] d) A Brownian ratchet device for continuous separation based on diffusivities;[143] e) A “DNA prism” device using asymmetric pulsed field to sort DNA into streams of different angles;[43] f) A nanofilter device for separating DNA and protein based on entropic trapping and sieving mechanisms;[145] g) A staircase slit device offering a powerful tool to study entropic effects;[146] h) The transport of  $\lambda$ -phage DNA in channels with 50 nm’s width.[147] ..... 45

**Figure 1.9.** a) Schematic of the self-assembled posts of paramagnetic beads aligning with magnetic field.[31] b) SEM image of a hexagonally closed packed 2  $\mu$ m polystyrene colloidal array fabricated within a microchannel. The arrows indicate lattice defects. The scale bar is 10  $\mu$ m.[41] ..... 48

**Figure 2.1.** a) Schematic of the chip design for continuous angular separation by asymmetric pulsed field electrophoresis. b) The packing process of CSA arrays without (left column) and with pore size gradient (right column). c) A photo of a chip packed with silica particle array of 320-100 nm gradient..... 64

**Figure 2.2.** a) Schematic of the angular separation. DNA samples are continuously injected into the separation chamber filled with silica CSA arrays. Pulsed electric fields  $E_1, E_2$  shown on the right are applied across the chamber. Larger DNA have larger deflection angle ( $\theta$ ) relative to the vertical line. Fluorescent images and intensity profiles of optimized separations of 4 DNA mixture (2, 6, 10, 20 kbp) in arrays of b) 100 nm particles at  $E_1 = 160$  V/cm,  $f = 5$  Hz and c) 320 nm at  $E_1 = 160$  V/cm,  $f = 20$  Hz are shown. .... 67

**Figure 2.3.** Centre column: SEM image of the separation chamber. Numbering scheme (i. ii. iii) refers to the larger, boundary and smaller particle packed regions. The top part of the separation chamber is packed with 700 nm particles (i), the middle part is the interface (ii), the bottom part of the separation chamber is packed with 320 nm particles. (iii). Left column: zoomed-in SEM images of the three regions. Right column: fluorescence images of the separation of four sizes of DNA (2, 6, 10, and 20 kbp) injected into the chamber in regions (i) 320 nm particle, (ii) the interface, (iii) 100 nm particle. Scale bar is 50  $\mu$ m.  $E_1 = 160$  V/cm,  $f = 15$

Hz..... 68

**Figure 2.4.** Two-dimensional separation of six different sizes of DNA (2, 4, 6, 10, 15, 20 kbp) in a) 320nm, b) 100 nm structures, and with 320/100 nm size gradient at  $E_1 = 280$  V/cm,  $f = 15$  Hz. i: the separation at the top of separation chamber packed with 320 nm particles. ii: the separation at the interface. iii: the separation at the bottom of the separation chamber packed with 100 nm particles. .... 71

**Figure 2.5.** Analysis of the deflection angle  $\theta$  in 320 nm (hollow square), 100 nm (hollow triangle) and 320/100 nm gradient (solid circle) arrays at  $E_1 = 280$  V/cm,  $f = 15$  Hz. .... 72

**Figure 2.6.** DNA separation inside 700/300 nm particles at  $E_1 = 280$  V/cm,  $f = 15$  Hz. a) in the 700 nm region before the boundary, b) in the 300 nm region after the boundary..... 73

**Figure 3.1.** (a) PDMS microchip for DNA separation. The microchip contains an injection channel which is connected to the separation chamber (the square part in the middle of the microchip) where the separation of DNA molecules occurs. The chamber is connected to different buffer reservoirs in order to apply the electric field (b) SEM image of self-assembled 320 nm silica particles inside the separation chamber. (c) SEM image of the top surface of (b) which shows a uniform hexagonal packed structure. .... 79

**Figure 3.2.** a) Schematic of the DNA separation microchip. b) Fluorescent

image of the junction of the separation chamber and injection channel. A mixture of three different sizes of DNA: 6, 10, and 20 kbp is injected into the separation chamber. c) Fluorescent image of the separated DNA molecules in the middle of the separation chamber. d) and e) fluorescent intensity profiles at the injection and the middle of the separation chamber along the dashed lines in b) and c), respectively. .... 81

**Figure 3.3.** a) SEM images of the self-assembled packed structures of 320 and 700 nm silica particles with different  $\chi_{700}$  from the top:  $\chi_{700} = 0, 0.09, 0.16,$  and  $0.5$ . The first top image is the ideal hexagonal lattice of spheres generated by the image analysis software. b) Radial distribution function calculated for each structure shown in a).  $a_p$  is the particle radius. c) Global orientational order parameter calculated for each structure shown in a). ... 85

**Figure 3.4.** Variation of global orientational order parameter,  $\psi$ , with respect to  $\chi_{700}$ . .... 86

**Figure 3.5.** Probability of the presence of five different pore sizes as a function of the volume fraction of the larger particle,  $\chi_L$ , in the binary packing of spheres with size ratio of 0.45. [29] ..... 87

**Figure 3.6.** Variation of peak distance between 6-10 kbp and 10-20 kbp DNA molecules with respect to  $\chi_{700}$  for (a)  $E_I = 160$  V/cm,  $f = 15$  Hz and (b)  $E_I = 280$  V/cm,  $f = 20$  Hz. .... 90

**Figure 3.7.** Variation of band broadening,  $\sigma_{\text{other}}$  calculated using Eq. 1b, for

6, 10, and 20 kbp DNA molecules with respect to  $\chi_{700}$  for (a)  $E_I = 160$  V/cm,  $f = 15$  Hz and (b)  $E_I = 280$  V/cm,  $f = 20$  Hz..... 92

**Figure 3.8.** Variation of separation resolution,  $R_s$  calculated using Eq. 2, between 6-10 kbp and 10-20 kbp DNA molecules with respect to  $\psi$  for (a)  $E_I = 160$  V/cm,  $f = 15$  Hz and (b)  $E_I = 280$  V/cm,  $f = 20$  Hz..... 93

**Figure 3.9.** Variation of scaled resolution  $R_s^* = R_s/R_{s\chi_{700}=0}$  with respect to  $\chi_{700}$ ..... 96

**Figure 4.1.** Chip structure and experimental setup. a) A PDMS chip on a glass slide. b) Chip design and reservoirs. c) Injection, the picture on the right is the fluorescent image at the crossing region. d) Separation, the right image is the intensity profile from fluorescent imaging signals. .... 108

**Figure 4.2.** a) SEM images, b) orientational order parameter of CSA structures, scale bars represent 1  $\mu\text{m}$ , and c) radial distribution function, the distance,  $r$ , is scaled by the radius of 540 nm particles,  $r_{540}$ . All ratios are the volume ratio between 540 and 900 nm particles. .... 114

**Figure 4.3.** The calculated average pore size ( $a$ ) and pore size frequency distribution ( $P$ ) in 540/900 nm binary packed structures. .... 117

**Figure 4.4.** DSC curve for 540 nm monodisperse particle array, arrows indicate the direction of scans. .... 120

**Figure 4.5.** Pore volume distribution, average pore size ( $a(\text{DSC})$ ) and several descriptive statistics parameters: peak radius ( $R(\text{peak})$ ), standard

deviation ( $\sigma$ ), kurtosis (Kurt), and skewness (Skew) of the distribution corresponds to the logarithm of pore radius ( $\log R$ ) obtained from DSC for CSA structures. Data correspond to monodisperse structures are plotted in red. .... 124

**Figure 4.6.** a) Porosity ( $\epsilon$ ) from DSC (dots above) and Dodds' model (red line below), red circles represent the monodispersed structures, the blue dashed line is the porosity of fcc or hcp packing; b) accessible volume fraction ( $f$ ) from DSC (dots) and Dodds' model (lines), with different color for each DNA size. .... 127

**Figure 4.7.** a)  $\log \mu/\mu_0$  vs.  $N$ ; b) the left side of Equation 4.20 plotted over  $\psi$ . .... 132

**Figure 4.8.** a)  $\log D_E$  vs.  $a(\text{DM})$ , solid points represent binary packed structures, hollow points represent pure structures; b) the left side of Equation 4.29 plotted over  $\psi$ . .... 140

**Figure A.1.** Generation of obtuse angle pulsed electric field across the separation chamber. a) A schematic diagram of the circuit. b) Square wave signals applied to each buffer reservoirs in order to form electric fields in the directions of  $E_1$  and  $E_2$ . .... 160

**Figure A.2.** The diagrams of the circuit and the voltage applied for a) b) injection and c) d) separation modes in DNA capillary zone electrophoresis. .... 161

**Figure A.3.** The schematic illustration of the lab-built fluorescent

microscopy for imaging under a) epifluorescent and b) non-epifluorescent  
setups ..... 162

# Symbols and Abbreviations

---

## *Latin alphabet*

$a$	average pore size (nm)
$A$	surface area ( $\mu\text{m}^2$ )
$a(\text{DM})$	average pore size calculated from Dodds' model (nm)
$a(\text{DSC})$	average pore size measured by differential scanning calorimetry (nm)
$b$	Kuhn length (nm)
$c$	obstructed volume fraction
$C$	gel concentration
$D$	diffusion coefficient ( $\text{cm}^2/\text{s}$ )
$D_0$	free-solution dispersion coefficient ( $\text{cm}^2/\text{s}$ )
$d_c$	channel diameter (nm)
$D_E$	dispersion coefficient ( $\text{cm}^2/\text{s}$ )
$e$	elementary charge ( $4.355 \times 10^{-19}$ C)
$E$	electric field (V/cm)
$E_1, E_2$	applied electric field in pulsed field electrophoresis (V/cm)
$f$	frequency (Hz)
$f_A$	accessible volume fraction
$F_{el}$	electrostatic force on a charged particle (N)

$F_f$	frictional force on DNA in solvent (N)
$f_L$	appearance probabilities of large particles
$F_{ret}$	electrostatic force on the double layer (N)
$f_S$	appearance probabilities of small particles
$f^*$	scaled frequency
$g(r)$	radial distribution function
$\Delta H_{fus}$	enthalpy of fusion of water (kJ/g)
$I$	ionic strength (mol/L)
$K$	spring constant (N/m·mol)
$k_1, k_2, k_3, k_4$	fitting parameters
$k_B$	Boltzmann's constant ( $1.381 \times 10^{-23}$ J/K)
$K_r$	retardation factor
Kurt(logR)	excess kurtosis of the pore size distribution
$L$	molecular length (nm)
$L_c$	DNA contour length (nm)
$M$	Helmholtz free energy of DNA chains (J)
$N$	DNA molecule size (base pair)
$n$	number Kuhn segments
$N_A$	Avogadro's number ( $\text{mol}^{-1}$ )
$p$	persistent length of DNA (nm)
$P$	probability
$Pe$	Péclet number

$PD$	peak distance ( $\mu\text{m}$ )
$q$	effective charge of each Kuhn segment (C)
$Q$	heat (J)
$q_e$	effective charge of each base pair (C)
$Q_p$	particle charge (C)
$\mathbf{r}$	step vector
$R$	Pore diameter (nm)
$r_w$	radius of the confined lump of freezable water (nm)
$r_{540}$	SEM observed radius of 540 nm particles (pixel)
$R_A$	accessible radius (nm)
$R_g$	gyration radius of a polymer (nm)
$R_n$	end to end distance of an ideal polymer chain (nm)
$\mathbf{R}_n$	end-to-end vector
$r_p$	particle radius (nm)
$R_p$	pore radius (nm)
$Rs$	separation resolution
$Rs_{bed}$	separation resolution arising solely from the separation bed
$Rs^*$	scaled separation resolution
$R_t$	total pore radius (nm)
$r_w$	radius of the confined freezable water (nm)
$R(\text{peak})$	peak pore diameter (nm)
$S$	entropy of DNA chains (J/K)

Skew(logR)	skewness of the pore size distribution
$t$	retention time (s)
$T$	absolute temperature (K)
$t_{or}$	reorientation time of DNA (s)
$T_p$	melting temperature of confined liquid (°C)
$T_0$	normal melting point of the liquid (°C)
$\vec{t}(s)$	unit vector tangent to the chain at position $s$
$\Delta T$	difference between $T_p$ and $T_0$ (°C)
$U$	internal energy of chain conformation (J)
$v$	velocity (cm/s)
$V_A$	accessible pore volume ( $\mu\text{m}^3$ )
$V_p$	pore volume ( $\mu\text{m}^3$ )
$V_T$	total volume ( $\mu\text{m}^3$ )
$w$	DNA width (nm)
$Wb$	base line width ( $\mu\text{m}$ )
$z$	valence of ions

*Greek alphabet*

$\alpha$	constant derived from the Gibbs-Thomson equation (nm·K)
$\beta$	non-freezable water layer thickness (nm)
$\gamma$	scale of electrostatic interaction between analytes and matrix surface (nm)

$\gamma_{sl}$	surface energy of the solid-liquid interface (J/m <sup>2</sup> )
$\delta$	limiting ratio of free-solution to in-gel mobility
$\varepsilon$	porosity
$\varepsilon_f$	scaled electric force parameter
$\varepsilon_s$	dielectric constant (F/m)
$\varepsilon(\text{DM})$	porosity calculated from Dodds' model
$\varepsilon(\text{DSC})$	porosity measured by differential scanning calorimetry
$\zeta$	zeta potential (V)
$\eta$	solvent dynamic viscosity (N·s/m <sup>2</sup> )
$\theta$	deflection angle of DNA streams (°)
$\theta_{\text{max}}$	maximum angle (°)
$\iota$	contact angle (°)
$\kappa^{-1}$	Debye length (m)
$\lambda$	Odijk segment (nm)
$\mu$	electrophoretic mobility (cm <sup>2</sup> /V·s)
$\mu_{\text{EOF}}$	mobility of the electroosmotic flow (cm <sup>2</sup> /V·s)
$\mu_0$	free solution mobility (cm <sup>2</sup> /V·s)
$\mu_1, \mu_2$	DNA electrophoretic mobilities in the direction of $E_1$ and $E_2$ (cm <sup>2</sup> /V·s)
$\mu^*$	extrapolated field-free mobility (cm <sup>2</sup> /V·s)
$\nu$	exponential factor
$\zeta$	friction coefficient of each Kuhn segment (N·s/m)

$\zeta_e$	friction coefficient per base pair (N·s/m)
$\rho$	obstacle density
$\rho_s$	density of ice (g/cm <sup>3</sup> )
$\rho_{\text{SiO}_2}$	density of amorphous silica (g/cm <sup>3</sup> )
$\sigma^2$	variance of peaks in separation (cm <sup>2</sup> )
$\sigma^2_{\text{other}}$	variance of the fluorescence intensity profile associated with the separation bed (cm <sup>2</sup> )
$\sigma^2_{\text{inj}}$	variance of the fluorescence intensity profile associated with the injection channel (cm <sup>2</sup> )
$\sigma^2_{\text{total}}$	total variance of the fluorescence intensity profile at the separation chamber (cm <sup>2</sup> )
$\sigma^2(t)$	variance in time (s <sup>2</sup> )
$\sigma^2(x)$	variance in length (μm <sup>2</sup> )
$\sigma(\log R)$	standard deviation of pore size distribution
$\tau$	relaxation time (s)
$\tau_0$	Kuhn segment relaxation time (s)
$\phi$	angle between two pulsed fields (°)
$\varphi$	size ratio
$\chi_{700}$	volume fraction of 700 nm particles in a bidisperse suspension of 320 and 700 nm particles
$\chi_{900}$	volume fraction of 900 nm particles a bidisperse suspension

of 540 and 900 nm particles

$\psi$  orientational order parameter

$\omega$  angle between a line bonding nearest particles and an arbitrary reference axis ( $^{\circ}$ )

### *Abbreviations*

APFE asymmetric pulsed field electrophoresis

bp base pair

BRF biased reptation with fluctuation

BRM biased reptation model

CE capillary electrophoresis

CSA colloidal self-assembly

CZE capillary zone electrophoresis

DNA deoxyribonucleic acid

DSC differential scanning calorimetry

dsDNA double stranded DNA

EBL electron beam lithography

EOF electroosmotic flow

EVU ultraviolet light

fcc face-centered cubical

FIB focus ion beam

FJC freely jointed chain

GE	gel electrophoresis
hcp	hexagonal close packing
IL	interferometric lithography
NL	nanoimprint lithography
NMR	nuclear magnetic resonance
OMRC	Ogston-Morris-Rodbard-Chrambach
PAGE	polyacrylamide gel electrophoresis
PDMS	polydimethylsiloxane
PFE	pulsed field electrophoresis
PFGE	pulse field gel electrophoresis
PSD	pore size distribution
PVD	pore volume distribution
RBS	rouse bead-spring
ROP	rope-over-pulley
SEM	scanning electron microscopy
ssDNA	single stranded DNA
TBE	tris-borate-ethylenediaminetetraacetic acid
WLC	worm-like chain
$\mu$ TAS	micro total analysis systems

# Chapter 1

## Introduction

---

### 1.1 Background and Motivation

#### 1.1.1 Introduction

Size oriented separation of DNA is a major pillar of DNA analysis and various biotechnologies, such as the sequencing process employed by the Human Genome Project [1]. The continuous development of applications in researches since [2-6] demands improvement of DNA separation to higher speed, throughput, resolution, and lower cost [7-10]. In the past, slab gel electrophoresis dominated DNA separation; now capillary electrophoresis has become the dominant technique. Hybridization and mass spectrometry may replace electrophoresis in the future with the development of next-generation DNA sequencing [11-14]. but electrophoresis will probably remain as a major tool for sequencing. Electrophoresis relies on the size-dependent mobility of DNA in a sieving matrix, and the separation mechanism rises from the interaction of DNA molecules with the porous structure [15-18].

Electrophoresis in agarose or polyacrylamide gel, is the most widely

used technique, in either slab-gel or capillary configurations [19-21]. Despite its great success over decades, gel electrophoresis (GE) can only successfully resolve DNA up to 10 kbp [22, 23]. As a complement, the method known today as pulse field gel electrophoresis (PFGE), invented in 1984, conquered the size range up to 50 Mbp[24, 25]. The two techniques employ different underlying mechanisms: GE separation follows the sieving mechanism in which the size of DNA random coil is smaller than the pores size of the media; PFGE functions in the reptation regime where DNA molecules are more stretched and could not be separated by GE. The resolving power of PFGE comes from the reorientation of elongated DNA chains, following the shift of electric field directions [15]. Gel electrophoresis in either slab-gel or capillary configurations has several drawbacks. Slab-gel requires a large amount of sample, a new gel should be prepared for each run, and a low electric field is used to suppress Joule heating, resulting in relatively long separation times [26, 27]. Higher field can be applied in capillary electrophoresis since the heat generated is easily lost due to the 50~300  $\mu\text{m}$  scale of slender capillaries. However, the separation in a capillary can only be one-dimensional.

Micro total analysis systems ( $\mu\text{TAS}$ ), also known as “lab-on-a-chip” technology, has been developing rapidly since its introduction in the early 1990s [28]. Microfluidics, generally defined as the science and technology of manipulating small amounts of fluids ( $10^{-9}$  to  $10^{-15}$  L), has been a

keystone idea for the miniaturization of analytical devices and systems, and it offers opportunities to develop new separation methods and materials. With advances in micro and nanofabrication techniques during the last two decades, a variety of novel micro- and nano-fluidic devices have been applied in DNA electrophoresis. Miniaturized devices have several advantages over conventional normal scale techniques: such as less Joule heating [29-31], faster separation [32-34], smaller sample amount [35], high resolution and sensitivity in separation and detection [36], as well as being integratable and portable [37-39], although the fabrication process may be complicated and expensive.

Colloidal self-assembly (CSA), also known as self-organization, was employed in microfluidic devices as a sieving matrix for separation, because of its easier fabrication and lower cost compared with microfabricated procedures. Based on the pioneering work of Wirth's group which showed that self-assembling inorganic particles can serve as a replacement to gels in electrophoresis [40], a microfluidic device for DNA separation has been developed in our group. In this device, a self-assembled silica nanoparticle array serves as a separation matrix in capillary zone electrophoresis of DNA and surfactant denatured proteins [41]. Furthermore, a pulsed field DNA electrophoresis device has been designed [42], with inspiration from the "DNA prism" device fabricated by Austin et al. [43] This device showed good continuous two-dimensional angular

separations, dependent on the DNA size, field strength, and pulse frequency.

The promising preliminary results with CSA proved the feasibility of using nanoparticle arrays as a matrix for DNA separation, but a few unknowns remain in the separation mechanism of DNA in the devices. The full potential of the CSA approach for DNA separation still remains to be explored. The objective of this thesis is to investigate the role of separation media architecture on DNA separation performance, studying several matrix combinations in order to explore aspects of the separation mechanism. Our previous work employed highly hexagonal ordered nanoporous media, packed with single sized monodisperse particles. In this work, a step gradient of pore size was introduced by filling the device with a series of monodisperse packed zones of different particle sizes. The device design improved the effective range and peak capacity of our chips. Most separation matrices used for DNA separation to date are either highly disordered, such as gels, or highly ordered, such as microfabricated arrays. Using the self-assembly approach of binary mixtures, structures with systematically tuned order were fabricated. So, in addition to confinement size controlled by the pore size [44], the role of confinement geometry or architecture on separation performance is also investigated in both configurations of zone electrophoresis and pulsed field electrophoresis. Various different methods were developed to characterize the CSA

packing.

### **1.1.2 Scope of the Thesis**

The overall objectives of this study have been laid out above, and details of each chapter are given below. The latter part of this chapter is a general overview of DNA electrophoresis and separation media. A brief description of polymer physics in free solutions and nanoscale confinement, and the principles of electrophoretic methods are presented to facilitate our discussions in the following chapters. Different migration mechanisms of DNA in separation media under an electric field, as well as various types of separation techniques including gel, capillary and microfabricated devices are also discussed.

In Chapter 2, a pore size gradient is introduced into an asymmetric pulsed field electrophoresis device. The separation media is modified to a step gradient configuration by packing monodisperse zones of different sizes in sequence. DNA separation experiments show that DNA separation could be improved by a proper gradient. Better effective separation range and peak capacity is observed in gradient structures compared to a corresponding monodisperse CSA matrix.

In Chapter 3, we investigate the role of order in a separation matrix on pulsed field DNA electrophoresis performance. Monodisperse suspensions of nanoparticles yielded highly ordered structures. Binary

suspensions, on the other hand, provide disordered structures, where the degree of disorder can be systematically changed by varying the volume fractions of the two particles in suspension. Different analytical parameters were calculated to characterize each structure. A DNA separation experiment was conducted in each structure and the separation band distance, band width, and separation resolution were measured and calculated. The results show that DNA separation is significantly affected by the degree of disorder in the separation matrix. A non-monotonic dependence of DNA separation with the degree of order is observed.

In Chapter 4, the effect of the matrix order is tested in capillary zone DNA electrophoresis functioning in the Ogston sieving regime. Separation experiments are quantified by DNA electrophoretic mobility and dispersion coefficient. A theoretical model, thermoporosity method, and SEM images are used to characterize the separation media. The influence of the order is confirmed by statistical tests, and the results show that a higher degree of order yields faster migration and lower dispersion.

Finally, in Chapter 5, a summary of the key observations in this study is provided and some directions for future research in this field are suggested.

## **1.2 Polymer Physics**

### **1.2.1 DNA Conformation in Free Solutions**

DNA, short for deoxyribonucleic acid, either single or double stranded (ssDNA or dsDNA), is a semi flexible polymer composed of basic units called bases or base pairs (bp). The structural biology of DNA is remarkably complex and discussed in detail elsewhere [45, 46]. In what follows, we focus on the most common conformation—the B-form double helix, in which each base pair is about 0.34 nm long, and the molecule has a width of around 2 nm. The base residues, adenine, guanine, thymine, and cytosine, are connected by phosphodiester bonds and screened from the external environment by the phosphate backbone. The molecule are negatively charged in aqueous solution due to the dissociation of proton from the phosphate group, independent of sequence and evenly distributed along the chain.

Since DNA molecules are flexible linear chains, DNA of sufficient length is believed to be randomly coiled in free solution because of thermal drifting, with a radius called the gyration radius,  $R_g$ . (Figure 1.1a) [47]. The most straightforward model of flexible chains is the freely jointed chain (FJC) model [48], where a polymer is simplified as  $n$  rigid rods, or segments, of constant length  $b$  connected freely together, as shown in Figure 1.1b. The length of each segment is also called the Kuhn length. The stretched length of a polymer is known as the contour length,

$$L_c = nb \tag{1.1}$$

which is the actual size in case of very short molecules (e.g. 100 bp or shorter dsDNA) with a rigid rod conformation.

The end-to-end vector,  $\mathbf{R}_n$ , of the chain can be modeled as a sum of random walks of step vector  $\mathbf{r}$ . Thus the mean square end-to-end distance  $\langle R_n^2 \rangle$  is given by [49]:

$$\langle R_n^2 \rangle = \langle \mathbf{R}_n \cdot \mathbf{R}_n \rangle = \sum_{i=1}^n \sum_{j=1}^n \langle \mathbf{r}_i \cdot \mathbf{r}_j \rangle = nb^2 = bL_c \quad (1.2)$$

The probability distribution of the distance  $R_n$  is Gaussian for long chains:

$$p(R_n) = \left( \frac{3}{2\pi \langle R_n^2 \rangle} \right)^{3/2} \exp \left( -\frac{3R_n^2}{2 \langle R_n^2 \rangle} \right) \quad n \gg 1; R_n \ll nb \quad (1.3)$$

And the entropy of the chain,  $S$ , and Helmholtz free energy,  $M$ , can be derived as

$$S = k_B \ln(p(R_n)) = S(0) - \frac{3k_B R_n^2}{2nb^2} \quad (1.4)$$

$$M = U - TS = M(0) + \frac{3k_B T R_n^2}{2nb^2} = M(0) + \frac{1}{2} K R_n^2 \quad (1.5)$$

where  $S(0)$  and  $M(0)$  represent the entropy and Helmholtz free energy of the chain at equilibrium.  $U$  is the internal energy independent of chain conformation,  $T$  is the absolute temperature, and  $k_B$  is the Boltzmann's constant. This equation implies that in the absence of external forces, such as stretching, the equilibrium end-to-end length of the chain is zero. This

conclusion does not describe the real polymer conformation because the FJC model is developed from an ideal system which ignores the interactions between segments and between the chain and surrounding solvent, such as excluded volume, internal electrostatic repulsion and hydrodynamic interactions.

Polymer chains are often stiffer because of restrictions of chemical bonds and the electrostatic repulsion by the charges on the chain, exerting correlation between orientations of monomers. The worm-like chain (WLC) model is more suitable for the case where the chain flexibility is due to thermal agitation. The WLC model envisions an entropic rod that is continuously and smoothly curved (Figure 1.1c). For a polymer of contour length  $L_c$ , the end-to-end vector is given by

$$\mathbf{R}_n = \int_0^L \vec{t}(s) ds \quad (1.6)$$

where  $\vec{t}(s)$  is the unit vector tangent to the chain at position  $s$  along the chain. Orientation correlation exists for two adjacent points, but decays exponentially along the chain:

$$\langle \vec{t}(s) \cdot \vec{t}(0) \rangle = e^{-s/p} \quad (1.7)$$

where  $p$  is the characteristic persistent length capturing the stiffness of the chain. The persistent length is usually around 50 nm for dsDNA, and decreases when the solution has higher ionic strength, due to more

screening of the backbone charges [50]. The mean square end-to-end distance of the WLC is thus given by

$$\langle R_n^2 \rangle = \langle \mathbf{R}_n \cdot \mathbf{R}_n \rangle = \left\langle \int_0^L \vec{t}(s) ds \cdot \int_0^L \vec{t}(s') ds' \right\rangle \quad (1.8)$$

$$\langle R_n^2 \rangle = 2pL_c \left[ 1 - \frac{p}{L_c} \left( 1 - e^{-L_c/p} \right) \right] \quad (1.9)$$

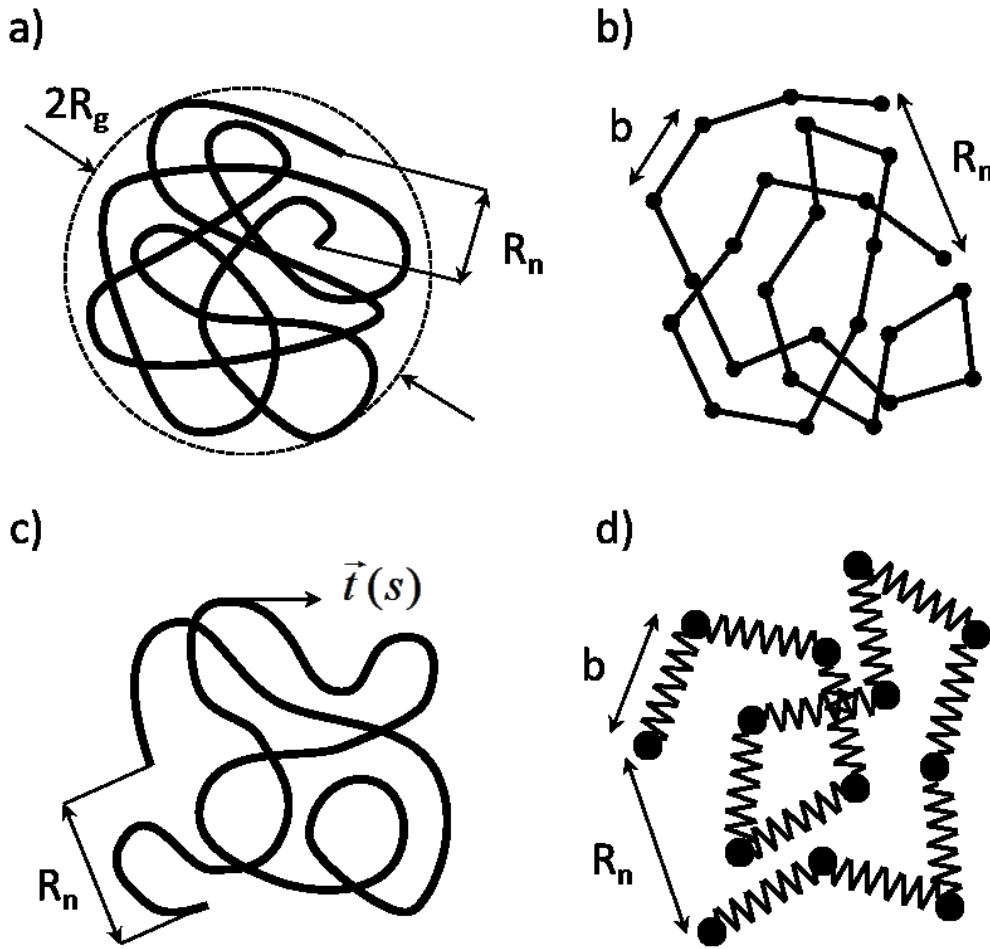


**Figure 1.1.** Schematic of models of polymer chain. a) DNA in a free solution as a coiled molecule. b) Freely-jointed-chain (FJC) model. c) Worm-like chain (WCM) model. d) Rouse bead-spring (RBS) model.

In the limit of long chain ( $L_c \gg p$ ),

$$\langle R_n^2 \rangle = 2pL_c \quad (1.10)$$

Compare Equation 1.10 with Equation 1.2, we see that the WLC can be expressed as a FJC composed of a number  $n$  of uncorrelated Kuhn segments,  $L_c = nb$ . Also, the Kuhn length is twice the persistent length in the WLC model,  $b = 2p$ .

The gyration radius,  $R_g$ , is given by[47]:

$$\langle R_g^2 \rangle = \frac{\langle R_n^2 \rangle}{6} = \frac{nb^2}{6} \quad (1.11)$$

Since  $n$  is proportional to the molecular size, Equation 1.11 indicates the size of the random coil is related to the DNA size  $N$  (in bp) by a power scaling law:

$$R_g \sim N^\nu \quad (1.12)$$

where  $\nu = 1/2$  for ideal chains. A correction to this dependence is proposed by Flory [51, 52], considering the self-excluded volume because two monomers cannot occupy the same position in space at the same time. This repulsion between monomers swells the gyration radius for chains with  $n \gg 1$ , and a larger exponent of  $\nu = 3/5$  accounts for the consequence of this self-avoiding effect.

Equation 1.5 can also be regarded as a harmonic spring with a spring constant  $K$ , which is called an “entropic spring”. Hence, a chain can also be

represented as composed of beads connected by segments of springs [53]. From this perspective, the Rouse bead-spring (RBS) model has been developed to describe polymer dynamics with friction from the solvent [54]. in contrast to static representations such as the FJC and WLC models. In the RBS model, a total number of  $n$  beads interact with each other through springs with average length  $b$ . (Figure 1.1d). The hydrodynamic interactions between segments are ignored, and solvent is able to penetrate through the coiled molecule and interact with each segment, which is called the “free-draining” phenomenon. The friction to each bead from the surrounding solvent and ions is characterized by a friction coefficient  $\xi$ . The total friction from the solution is:

$$F_f = n\xi \quad (1.13)$$

Using the Rouse friction assumption and Stokes-Einstein relation, the diffusion coefficient  $D$  and the relaxation time  $\tau$ , the time for a molecule to diffuse a distance on the order of its size, can be given by [47, 54, 55]:

$$D = \frac{k_B T}{n\xi} \quad (1.14)$$

$$\tau = \frac{\xi n^2 b^2}{3\pi^2 k_B T} \approx \frac{nb^2}{D} \approx \tau_0 n^2 \quad (1.15)$$

$\tau_0$  is the relaxation time of the Kuhn segment. As in the literature, the chain shows viscous elastic behavior on time scales shorter than  $\tau$ , while exhibiting simple diffusion on time scales larger than  $\tau$ . Thus, if DNA is

probed on time scales shorter than  $\tau_0$ , it does not move, but exhibits elastic response [47, 55].

As discussed, the RBS model still ignores the hydrodynamic interaction within the chain. By adding the hydrodynamic interactions between beads, the clump of fluid caged in the coil migrates together with the molecule instead of free-draining. Hence, the random coil is equivalent to a solid particle impermeable to solvents [56], and the Zimm's friction on the outer surface of the coil follows Stokes Equation, given the solvent viscosity,  $\eta$ , and velocity,  $v$ :

$$F_f = 6\pi\eta v R_g \quad (1.16)$$

modifying the model and defining the relaxation time as [57, 58]:

$$\tau \approx \tau_0 n^{3/2} \quad (1.17)$$

showing that hydrodynamic interactions decrease the relaxation time of the molecule.

## 1.2.2 DNA Conformation in Confinements

Polymer physics differs from the free solution case when a polymer is confined in channels or pores [59]. If one or more dimensions of channels or pores are smaller than the size of random coil, but still larger than the persistent length of the polymer, de Gennes [60, 61] demonstrated that the molecule is divided into blobs, distributing its length along the

channel, as shown in Figure 1.2a. The chain is flexible and coils randomly on the scale of one blob. The end-to-end distance was given by de Gennes as:

$$R_n \approx L_c \sqrt[3]{\frac{pw}{d_c^2}} \quad (1.18)$$

where  $w$  is the DNA width and  $d_c$  is the channel diameter. The relaxation time of the polymer in confinement predicted is:

$$\tau \approx \sqrt[3]{\frac{pw}{d_c^2} \frac{\eta b^2}{k_B T}} n^2 \quad (1.19)$$

When the channel size,  $d_c$ , is smaller than the persistence length,  $d_c < p$ , self-exclusion effects no longer govern the DNA conformation, giving way to intrinsic DNA elasticity, as well as interactions of DNA with the channel walls. This case of super-tight confinement ( $d_c < p$ ) is known as the Odijk regime, as investigated by Odijk [62, 63]. In this regime, DNA length stays in the narrow channel in deflections caused by polymer encounters with the channel walls, as shown in Figure 1.2b. The deflection,  $\lambda$ , is on the scale of the Odijk segment:

$$\lambda \approx \sqrt[3]{\frac{d_c^2}{p}} \quad (1.20)$$

Odijk predicts the end-to-end distance in the Odijk regime as [60, 64]:

$$R_n \approx L_c \left[ 1 - 0.361 \left( \frac{d_c}{p} \right)^{2/3} \right] \quad (1.21)$$

DNA friction comes from the hydrodynamic interaction of the Odijk segments with the channel wall [60]. The relaxation time of the molecule in this regime is calculated as:

$$\tau \approx \frac{d_c^\nu}{p \log \frac{d_c}{w}} \frac{\eta b^2}{k_B T} n^2 \quad (1.22)$$

There is a controversy over the exponent,  $\nu$ , of the channel size and how the

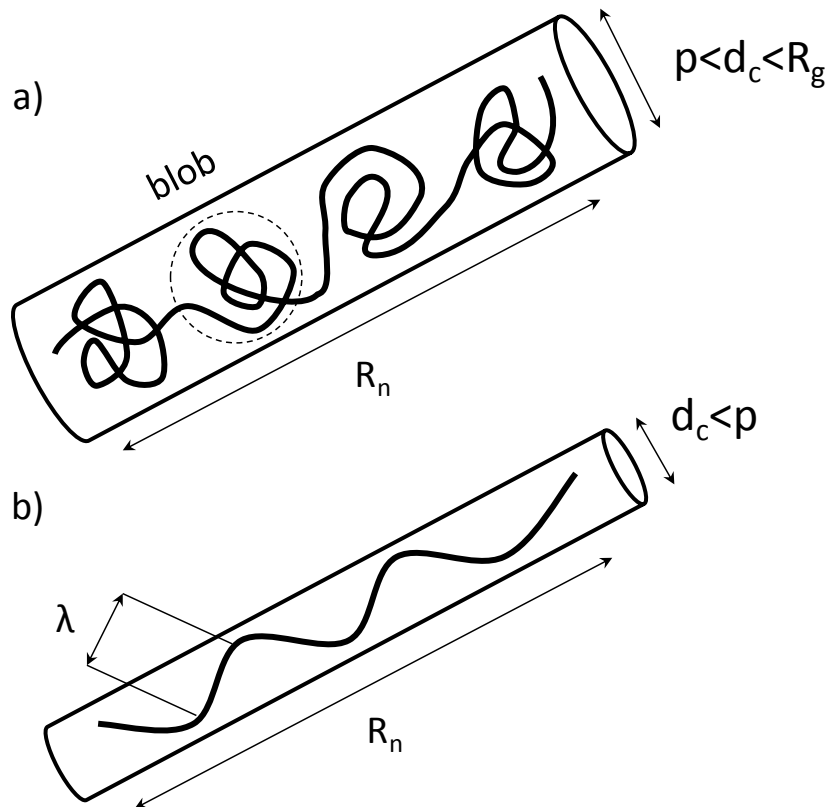


**Figure 1.2.** Conformation of a DNA in a) the de Gennes regime, and b) the Odijk regime.

relaxation time scales with the channel size. Values ranging from 1.6 to 2 are suggested for  $\nu$  in equation 1.22 [64-66].

## 1.3 Electrophoresis of DNA

### 1.3.1 Fundamentals of Electrophoresis

Electrophoresis is the motion of ions, molecules and other species with a certain surface charge in an electrolyte solution under an externally applied electric field [67]. The surface charge of an entity polarizes the ion distribution of the surrounding electrolyte solution, since the surface attracts ions with opposite charge while repulsing ions with the same sign. This electrostatic interaction results in an electric double layer (Figure 1.3a), with a thickness characterized by the Debye length,  $\kappa^{-1}$ , given by:

$$\kappa^{-1} = \sqrt{\frac{\epsilon_s k_B T}{2N_A e^2 I}} \quad (1.23)$$

where  $\epsilon_s$  is the dielectric constant of the solution,  $k_B$  is the Boltzmann's constant,  $T$  is the absolute temperature,  $e$  is the elementary charge,  $I$  is the ionic strength, and  $N_A$  is Avogadro's number.

The double layer has several sub-layers, as shown in Figure 1.3a: 1) the tightly absorbed Stern layer from the particle surface to the Stern plane; 2) the shear layer below the shear plane where ions and solvent molecules are still immobile; 3) the diffuse layer from the shear plane to the Gouy

plane in which the potential decays exponentially and extends gradually to the bulk solution. The electric potential at the shear plane is called the zeta potential,  $\zeta$ . The zeta potential is smaller than the surface potential, and is the potential that is measured by electrophoresis [67, 68].

Once an external electric field is applied, charged species start to migrate along the field due to an electrostatic force,  $F_{el}$ . In addition, the double-layer is also dragged by an electrostatic force,  $F_{ret}$ , in the direction opposite to the particle motion, and the bulk solvent exerts a frictional force,  $F_f$  (Figure 1.3b). The apparent velocity comes from the balance of the three forces. Electrophoretic mobility,  $\mu$  is the ratio of the velocity  $v$ ,

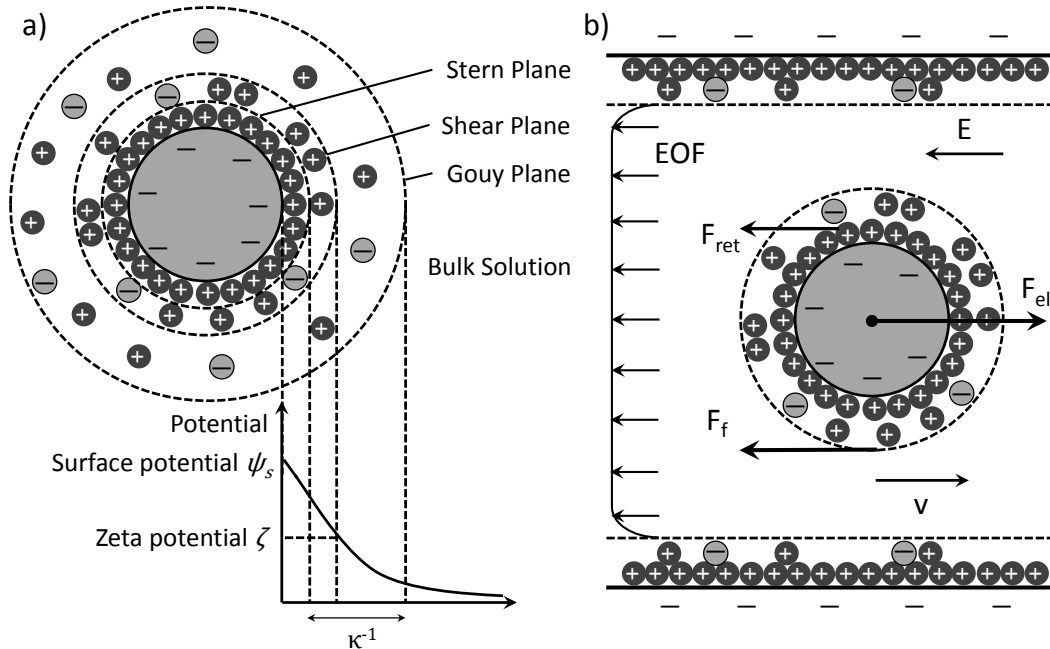


**Figure 1.3.** a) Schematic of an electric double layer around a negatively charged particle in an electrolyte solution. b) Electrophoresis of a negatively charged particle in an electrolyte solution with negatively charged substrate.

with respect to an applied electric field  $E$ ,  $\mu = v/E$ . The exact calculation of electrophoretic mobility is complicated, but for a spherical particle, analytical solutions can be found for two limiting cases classified by the particle radius,  $r_p$ .

For a thick double layer ( $\kappa^{-1} \gg r_p$ ), the Hückel solution indicates:

$$\mu = \frac{Q_p}{6\pi\eta r_p} \quad (1.24)$$

where  $Q_p$  is the particle charge, and  $\eta$  is the solution viscosity. In this case, charged species can be separated by electrophoretic mobility, dependent on their size and shAPFE.

For a thin double layer ( $\kappa^{-1} \ll r_p$ ), the Helmholtz-Smoluchowski solution shows:

$$\mu = \frac{\varepsilon_s \zeta}{\eta} \quad (1.25)$$

where  $\varepsilon_s$  is the solution's dielectric constant, and  $\zeta$  is the zeta potential. Mobility is independent of particle size and shAPFE in this extreme [67, 68].

In electrophoresis, surfaces of gels, other porous material, capillary tubes, and microchannels, are often charged as well as analytes. Electroosmotic flow (EOF) of the bulk solution will be induced under applied potential with a flat flow profile as shown in Figure 1.3b. The Helmholtz-Smoluchowski solution applies for EOF mobility,  $\mu_{EOF}$ , since

the double layer is much smaller than the characteristic length scale of the substrate:

$$\mu_{EOF} = \frac{\varepsilon_s \zeta_0}{\eta} \quad (1.26)$$

where  $\zeta_0$  is the zeta potential of the substrate surface. The apparent mobility of an analyte in electrophoresis is the net effect of its electrophoretic mobility and EOF.

Band broadening effect is important in electrophoresis, since it contributes to the separation resolution. As the major source of band broadening, dispersion can be practically calculated from the band broadening in the separation:

$$D_E = \frac{\sigma^2}{2t} \quad (1.27)$$

where  $\sigma^2$  is the variance of peaks in separation, and  $t$  is the migration time. Without an external field, dispersion is a pure thermal diffusion process driven by the concentration gradient, with diffusion coefficient origins from Fick's Laws. An enhancement to the diffusion has been observed under electric field [69], thus the term "dispersion" is used in order to differentiate from pure thermal diffusion in electrophoresis.

In physics, the Einstein–Smoluchowski relation indicates:

$$D = \mu k_B T \quad (1.28)$$

where  $D$  is the diffusion constant,  $\mu$  is the mobility, or the ratio of the

particle's velocity to an applied force,  $\mu = v/F$ ,  $k_B$  is Boltzmann's constant, and  $T$  is the absolute temperature. Thus, the enhancement to diffusion was described by the Nernst-Einstein relationship, linking the static diffusion coefficient,  $D$ , and the dispersion coefficient,  $D_E$ , by the ratio of the mobilities in the presence,  $\mu$ , and absence,  $\mu^*$ , of an electric field extrapolated from experimental data:

$$\frac{D_E}{D} = \frac{\mu}{\mu^*} \quad (1.29)$$

This expression follows the laws of thermodynamics and should be valid near equilibrium. However, this equation has been criticized by a number of researchers, pointing out it is problematic because electrophoresis is a highly non-equilibrium process [69-72]. Theory [15, 73] and experimental data [74, 75] both agree that the Equation 1.28 and 1.29 are generally not valid in DNA electrophoresis, except for very small molecules and very low field. The dispersion coefficient increases with the field intensity and is a weak function of the molecular size in practice.

## 1.3.2 DNA Migration Mechanisms

### 1.3.2.1 Free solution

In typical buffer conditions of DNA electrophoresis, the Debye length is 1~5 nm. This is much smaller than the intrinsic persistence length of DNA, placing it in the Helmholtz-Smoluchowski regime. The

electrostatic interaction leading to the mobility and the hydrodynamic interactions between segments are screened by the double layer, localized within the Debye length around the backbone. Therefore, solvent is able to penetrate through the coiled molecule, and DNA electrophoresis in free solution is free-draining, as confirmed by experiments [70, 72]. The equilibrium free solution mobility is obtained when the electrostatic force balances the drag force:

$$\mu_0 = \frac{v}{E} = \frac{nqE}{n\xi E} = \frac{q}{\xi} \quad (1.30)$$

Here  $E$  is the applied electric field.  $q$  and  $\xi$  are the effective charge and friction coefficient of one segment. Since the electrostatic driving force and the Rouse frictional drag force scale with molecular size, the electrophoretic mobility in free solution,  $\mu_0$ , is independent of size for DNA and other homogeneously charged polymers. The only exception is molecules shorter than the Kuhn length,  $\sim 200$  bp for dsDNA. In this case,  $\mu_0$  increases with DNA size as the chain is not long enough to form a coil [76, 77].

Paradoxically, DNA does not appear to be free-draining for the dispersion in the present of an electric field [70]. Diffusion controls the dispersion even with external field, and the Zimm's friction (Equation 1.16) should be used instead. According to the Stokes-Einstein equation, the free-solution dispersion coefficient,  $D_0$ :

$$D_0 = \frac{k_B T}{6\pi\eta R_g} \quad (1.31)$$

negatively depends on the gyration radius, and as a result, DNA size.

The Nernst-Einstein equation for dispersion coefficient accounting for the Rouse friction is:

$$D_0 = \frac{k_B T}{n\xi} = \frac{\mu_0 k_B T}{Nq_e} \quad (1.32)$$

where  $q_e$  is the effective charge of one base pair. In free-solution, however, molecular dispersion arises from hydrodynamic interactions with the solvent, while the electrophoretic mobility comes from electrostatic interactions with the electric field. Hence, equation 1.32 is not valid in free-flow electrophoresis except for molecules smaller than the persistent length,  $\sim 100$  bp for dsDNA [78], and in low field.

Equation 1.30 shows a well-known fact that electrophoresis cannot separate DNA in free solutions. Therefore, separation has to rely on new mechanisms introduced by porous media such as gels and micro-fabricated structures. The migration mechanism is strongly affected by the dimensions of the molecules, obstacles, and pores. According to the literature [79-81], three different regimes have been proposed for DNA electrophoresis, as shown in Figure 1.4, each of which will be discussed in the following sections.

### 1.3.2.2 The Ogston sieving regime

The Ogston regime applies when the size of the coil,  $R_g$ , is smaller than the pore size of the separation matrix,  $a$ , and the field is relatively low. (Figure 1.4a) In this case, macromolecules act as compact globular particles, with no conformation change during electromigration through the pores. The separation in this case can be treated as a filtration process driven by an electric field [15]. In this regime, a free-volume model called

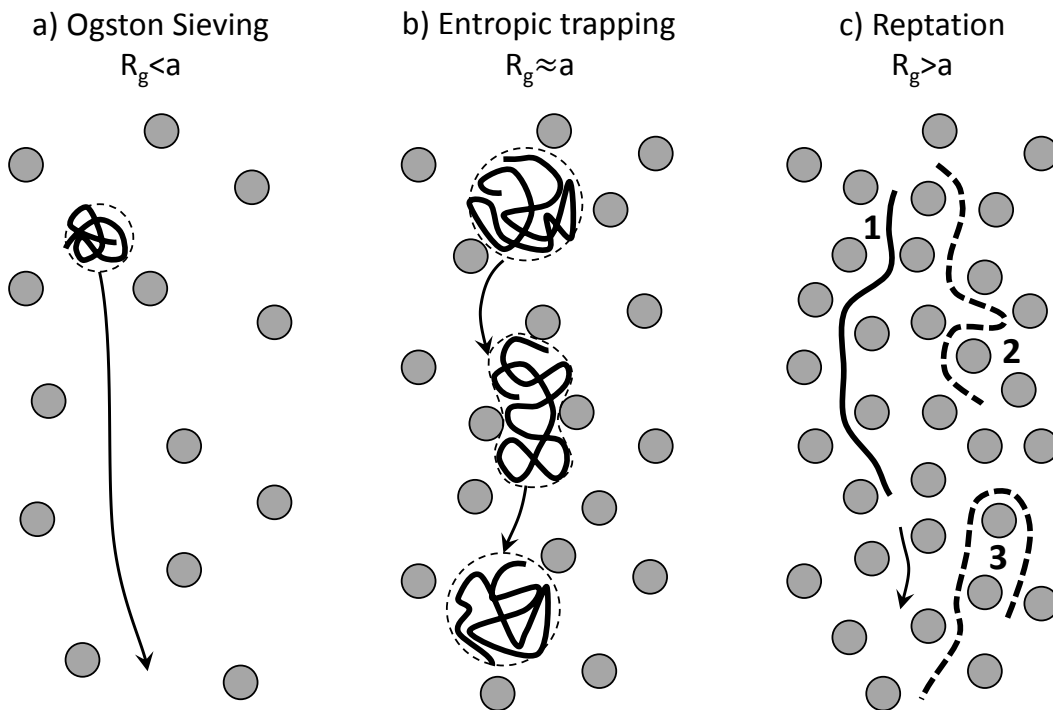


**Figure 1.4.** Three regimes of DNA electrophoresis. a) Ogston sieving, where the pore size in the separation media is larger than the DNA coil size. b) Entropic trapping, where the size of pores in the separation media is around the DNA coil size. c) Reptation regime, where the pore size is much smaller than the DNA coil size. Molecule 1 illustrates reptation with orientation. Hernia and hooking are shown by molecules 2 and 3 respectively.

the Ogston-Morris-Rodbard-Chrambach (OMRC) model [49, 82-84] proposed for media with sparse obstacles and porosity much smaller than the percolation threshold applies. The model states that the scaled mobility, i.e., the ratio between the mobility,  $\mu$ , in the separation media and the free-solution mobility,  $\mu_0$ , is equal to the fraction of accessible gel volume fraction,  $f(C,N)$ , where  $C$  is the gel concentration and  $N$  is the molecular size. For random media, the prediction is:

$$\frac{\mu}{\mu_0} = f(C, N) = \exp(-K_r C) = \exp\left(-\frac{\pi R_g^2}{4a^2}\right) \quad (1.33)$$

where  $K_r \sim R_g^2$  is a retardation factor and the average pore size,  $a$ , is related to the gel concentration  $C$  by  $a \sim C^{-1/2}$ . Equation 1.33 can be developed to the form of a Ferguson plot ( $\log \mu$  vs.  $C$ ):

$$\log \mu = \log \mu_0 - K_r C \quad (1.34)$$

which provides a standard method to determine molecular weight in gel electrophoresis of small analytes such as DNA. Equation 1.33 can also be rewritten as:

$$\log \mu = \log \mu_0 - kN \quad (1.35)$$

indicating a linear dependence to the molecular size [81]. Therefore, DNA with different sizes can be separated under a direct current field in the Ogston regime.

As to the dispersion in the Ogston regime, when the size of analytes

is much smaller than the pore size (called the Zimm-Ogston regime), the hydrodynamic interaction dominates, but the media confines the larger molecules more than the smaller ones due to an increased probability of collisions [85]. Thus Zimm's friction is valid, and dispersion scales with electrophoretic mobility as:

$$\frac{D_E}{D_0} = \frac{\mu}{\mu_0} = f(C, N) \quad (1.36)$$

When the size of the molecule becomes comparable to the pore size (called the Rouse-Ogston regime), the molecule feels significant excluded volume interactions and the hydrodynamic interactions are shielded by the obstacles [86]. The Zimm's model is replaced here by the Rouse friction, which neglects hydrodynamic interaction to predict dispersion:

$$D_E = \frac{k_B T}{n\xi} = \frac{\mu k_B T}{nq} = \frac{\mu_0 k_B T}{Nq_e} f(C, N) \quad (1.37)$$

Now the Nernst-Einstein equation becomes valid. However, the presence of two subregimes in the Ogston regime is often overlooked and the Rouse-Ogston subregime is hard to observe in practice. It is often interpreted as the transition between the Ogston and reptation regimes [85].

### 1.3.2.3 The entropic trapping regime

When the average pore size of the medium is commensurate with the dimension of the coil conformation, competition arises between the chain

staying randomly coiled in larger pores or deforming and migrating through the smaller domains. Migration has to overcome an entropic barrier due to the conformation change when molecules pass through a smaller pore. (Figure 1.4b)

This regime was originally predicted by simulations of polymer diffusion in a random matrix [87, 88], and verified experimentally later as an intermediate between the Ogston sieving and reptation regimes [89]. The mobility shows a strong dependence on DNA size  $N$  according to Slater et al. [90]

$$\mu \sim \frac{1}{N^{1+\nu}} \quad (1.38)$$

where the exponent  $\nu > 0$  represents the “strength” of the entropic effects.  $\nu$  decreases as the electric field increases, and approaches zero as DNA reaches the reptation regime.

Entropic trapping has been less recognized compared with the other two regimes, due to the accompanying of other mechanisms and the stringent conditions required for it to dominate. For example, the field strength should not be too small to provide sufficient enthalpy to overcome the entropic penalty in a realistic amount of time, and not be too large to make the trapping negligible. Also, the pore geometry and variation need to be well-defined, making observation of the effect in random porous gels unlikely. Nanofabricated structures offer precisely controlled architectures

and have been developed to investigate the effects of entropic trapping, which will be reviewed in Section 1.4.3.

#### **1.3.2.4 The reptation regime**

When the pore size of the media is smaller than the DNA gyration radius, DNA moves like a worm by a process called “reptation”. This concept was first introduced by de Gennes to describe the diffusion of a polymer chain in tight confinement. The confinement force the polymer to deform significantly from its random coil conformation [91-93]. Reptation can be described as a curvilinear one-dimensional motion along the chain axis, because the lateral movement of the chain is impeded by the surrounding obstacles. The external electric field makes the reptation motion biased towards the direction of the field gradient, usually with one head leading the sliding chain to thread its way through the porous network. This motion was called the biased reptation model (BRM), developed by Slater et al. [17, 94, 95] and Zimm et al. [96] The BRM model was later amended to biased reptation with fluctuation (BRF) by Viovy et al. [97] to take DNA length fluctuations into account during migration. Alternatives to the biased reptation is the formation of loops or hernias in the middle of a chain when a pore is crossed by the chain twice instead of once [93], or hooking when two ends migrate towards the field direction simultaneously (Figure 1.4c).

According to the biased reptation model, the formation of hernias would be improbable as long as external forces applied on the DNA chain are smaller than thermal forces [98, 99], Viovy et al. [15] introduced a scaled electric force parameter  $\varepsilon_f$ , which is the ratio of the electrostatic force to the thermal force applied on a DNA chain:

$$\varepsilon_f = \frac{\eta a^2 \mu_0 E}{k_B T} \quad (1.39)$$

where  $\eta$  is the buffer viscosity,  $\mu_0$  is DNA mobility in free solution,  $k_B$  is the Boltzmann's constant,  $a$  is the pore size, and  $T$  is the absolute temperature. Hernia and hooking formation is at its minimum when  $\varepsilon_f \ll 1$ .

The BRF model provides the best prediction of the experimental behavior of DNA gel electrophoresis among theoretical treatments developed. Real-time videomicroscopy of long DNA molecules migrating in gel has also validated the BRF model [80, 81]. The mobility in the BRF model is given by [15]:

$$\frac{\mu}{\mu_0} \approx \sqrt{\frac{1}{9N^2} + \left(\frac{2\varepsilon_f}{5 + 2\delta\varepsilon_f}\right)^2} \quad (1.40)$$

where  $\delta$  is the limiting ratio of free mobility to in-gel mobility of large DNA under strong fields, and  $\varepsilon_f$  is the scaled field defined in Equation 1.39. This equation provides satisfactory predictions of separation behavior in the reptation regime. For weak electric fields or shorter DNA molecules, DNA

chains are less oriented and stretched, thus possess more random conformations. This leads to a mobility strongly dependent on size but independent of field strength ( $\mu \sim \varepsilon_f^0 N^1$ ). As a result, separation can be achieved using DC electrophoresis. In contrast, the extent of biased orientation and stretching increases with molecular size and field strength, yielding a field-dependent mobility ( $\mu \sim \varepsilon_f N^0$ ) for very long DNA molecules or high electric fields. In this regime called reptation with orientation, different sizes of DNA molecule move with the same velocity under DC electrophoresis, so no separation can be achieved [80, 81].

As to dispersion, the BRF model predictions are also experimentally confirmed [70, 100], with three distinct subregimes: reptation-equilibrium ( $D_E \sim \varepsilon_f^0 N^2$ ,  $N \ll \varepsilon_f^{-2/3}$ ), accelerated reptation ( $D_E \sim \varepsilon_f N^{1/2}$ ,  $\varepsilon_f^{-2/3} < N < \varepsilon_f^{-1}$ ), and plateau ( $D_E \sim \varepsilon_f^{3/2} N^0$ ,  $N \gg \varepsilon_f^{-1}$ ). The first two cases are often more important because they lead to significant band broadening when the size dependent mobility should still allow separation [15].

### 1.3.2.5 Mechanism of pulsed field electrophoresis

The pulsed field electrophoresis (PFE) technique was developed to overcome the limitations of DC field separations and to increase the effective molecular size range of electrophoretic separations [24, 101]. In this method the direction of the electric field is periodically changed, and can be classified into three groups based on the field sequence. 1)

Intermittent-field electrophoresis, in which the DC field is switched off periodically. 2) Field-inversion electrophoresis, in which the field is altered between the two opposite directions, with different amplitudes or durations to give net motion. 3) Cross-field electrophoresis, in which two electric fields typically of the same magnitudes are applied alternately in two directions with a certain angle.

The separation mechanism of the pulsed methods is based on the biased reptation model and the size-dependent reorientation time of DNA molecules [102-104]. DNA molecules reptate through the porous matrix in the direction of the external field. Once a new field is applied, the new reptation has to be built up progressively from the previous state, so a chain starts to migrate from its initial state at a size-dependent velocity before it reaches the new steady state with size-independent mobility. Shorter molecules will respond more rapidly and spend a larger fraction of time migrating rather than reorienting through the pores [105]. This induces a net migration rate along the average field direction that is faster for shorter molecules in most circumstances. However, band inversions are observed, especially in field inversion electrophoresis, which has been successfully explained based by the BRF model. A brief summary of this aspect of the reptation model can be found in a comprehensive review contributed by Viovy [15].

Recent advances in experimental methods for tracking single DNA

molecules facilitate the understanding of the mechanism of the DNA movements under a pulsed electric field [29]. In the cross-field configuration, the zigzag type motion when the angle between two symmetric pulsed field  $\phi \leq 90^\circ$  (Figure 1.5a) results in poor or no separation. Experiments suggested the highest separation resolution can be achieved with an obtuse angle between the symmetric fields,  $\phi > 90^\circ$ . Angles of  $120^\circ$  or  $135^\circ$  are used in most experimental applications [25]. The observed reorientation presents head and tail switching. The end of the

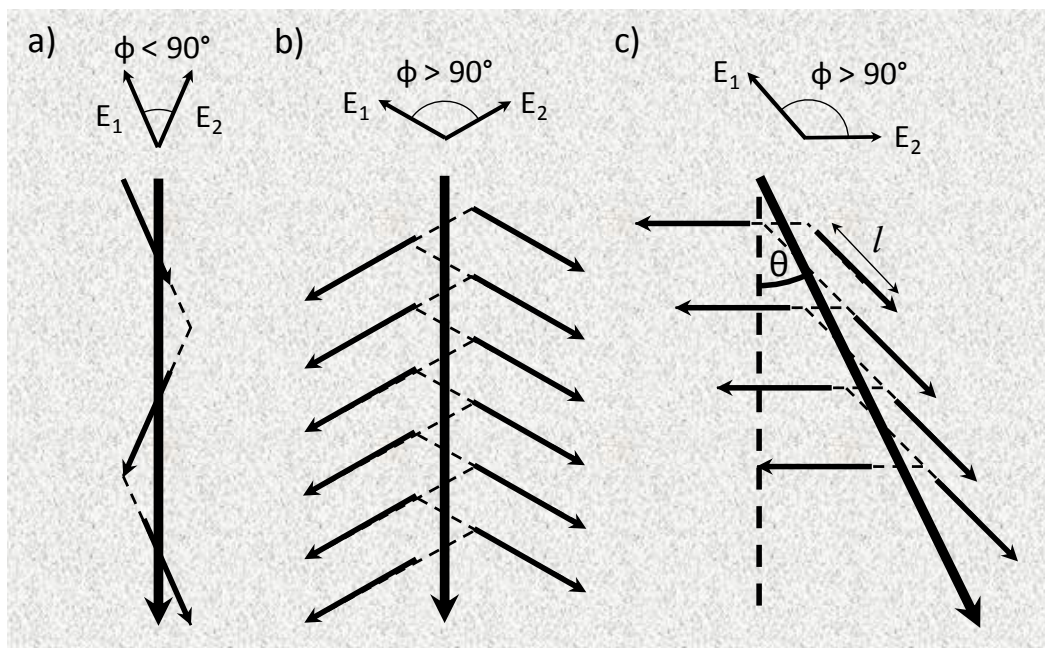


**Figure 1.5.** Schematic of migration mechanism of DNA in a porous media. Gray arrows indicate directions of net motion. a) The zigzag type motion with one leading head under symmetric pulsed electric fields with an acute angle. b) The chevron type motion with periodically changing head and tail under symmetric pulsed electric fields with an obtuse angle. c) The ratchet type backtracking motion under asymmetric electric fields.

molecule that was leading the chain along the previous direction becomes the tail after the electric field switches its direction. Thus the molecule backtracks in a chevron motion as shown in Figure 1.5b [105, 106].

Asymmetric pulsed field electrophoresis (APFE) (Figure 1.5c), although the fields have different magnitudes, shares a similar mechanism with the symmetric cross field electrophoresis. That is, the DNA reptates and backtracks along the directions of the fields as a flexible rod with a certain length [25, 106]. However, APFE creates an angular separation in which molecules with different sizes move along different directions characterized by the deflection angle  $\theta$ . It was observed that  $\theta$  was highly dependent on the frequency, electric field strength, and DNA size [42, 44].

For a relatively small frequency, short molecule and strong field, the molecule has enough time to reorient itself to the new direction, and to travel distances larger than its own length. A simple geometric model [42] was developed to describe this situation, based on the what was introduced by Austin et al. [29] to quantify the pulsed field electrophoresis of DNA within their microfabricated array. The model relates the net angular displacement,  $\theta$ , in each forward-backtrack cycle to the molecular length,  $l$ , electric fields,  $E_1$ ,  $E_2$ , and frequency,  $f$ :

$$\tan \theta = \tan \phi - \frac{\frac{\mu_2 E_2}{2f} - l}{\frac{\mu_1 E_1}{2f} - l} \sec \phi \quad (1.41)$$

where  $\mu_1$  and  $\mu_2$  are DNA mobilities along  $E_1$  and  $E_2$ , respectively. The term  $l/(\mu_2 E_2)$  is the time scale of the reorientation, i.e., the time for a molecule to travel its own length under  $E_2$ . By taking the ratio between the pulse duration and the reorientation time, a dimensionless scaled frequency,  $f^*$ , is defined as[44]:

$$f^* = \frac{2fl}{\mu_2 E_2} \quad (1.42)$$

and Equation 1.41 becomes:

$$\tan \theta = \tan \phi - \frac{1 - f^*}{\frac{\mu_1 E_1}{\mu_2 E_2} - f^*} \sec \phi \quad (1.43)$$

These equations predict a rising curve with increasing frequency for the deflection angle. The meditation is consistent with experiments showing that a maximum angle  $\theta_{\max}$  occurs when the frequency increases up to a value of  $f = (\mu_2 E_2)/(2l)$  ( $f^*=1$ ). However, the measured  $\theta_{\max}$  strongly depends on DNA size, contrary to the predicted size independent value of  $\phi=90^\circ$ . This discrepancy can be solved by taking the molecule relaxation and size fluctuation into consideration. Also, molecular dynamics of DNA electrophoresis such size fluctuation and hernia formation significantly affect the deflection behavior at higher frequencies, stronger fields and larger pore sizes. The deflection angle is observed as a plateau around  $\theta_{\max}$ , and decreases afterwards as the frequency increases and the molecule does

not have enough time to reorient completely. Under large frequencies,  $f > (10\mu_2 E_2)/(2l) (f^* > 10)$ , DNA molecules will sense the field as an average DC field, and  $\theta$  remains  $\sim 0^\circ$ , i.e., relatively constant for all sizes. In all regimes, the comparison of pulse time with reorientation time as well as relaxation time of molecules determines the separation behavior of pulsed field electrophoresis of DNA.

### 1.3.2.6 Effects of strong field

In the Ogston sieving mechanism, it is presumed that the polymer coils are rigid particles, and the matrix affects the molecule transfer by providing steric obstacles. When the electrophoretic convection dominates the transport instead of diffusion (e.g. strong electric field, long DNA molecules, and very small obstacles), the polymer undergoes a completely different process. The Péclet number [107] is used to quantify the strength of the field:

$$Pe = \frac{\mu_0 E p}{D_E} = \frac{\mu_0 E \xi L_c}{2k_B T} \quad (1.44)$$

If  $Pe > 1$ , once colliding with an obstacle, the post penetrates the coil more rapidly than thermal fluctuations that randomize the coil conformation [108]. so that the molecule uncoils, extends, and hooks around the obstacle. The next moment, the electric force drives the unhooking process, in which the stretched molecule hairpin slides around

and finally leaves the obstacle.

Models have been developed to describe this behavior. As the simplest version, the rope-over-pulley (ROP) model assumes the two ends of the chain are strongly stretched at either side. Collisions with nearly symmetric extended arms are referred to as U collision and those with asymmetric extended arms are J collisions as shown in Figure 1.6a[109]. More complex cases were also considered such as W collisions, where both ends migrate at one side with a loop at the other side, and X collisions, in which the short arm begins unhooking before the long arm completely uncoils [109].

DNA migration behavior upon collision is determined by the collision time, sum of the uncoiling time and unhooking time. In dilute arrays, the molecule has sufficient time to relax to random coil before encountering the next obstacle. Patel and Shaqfeh calculated the mobility and dispersion by two-dimensional Brownian dynamics simulations [110]:

$$\frac{\mu}{\mu_0} = \frac{1}{1 + 0.33\rho b^2 n^{3/2}} \quad (1.45)$$

$$\frac{D_E}{\mu_0 E a} = 0.06\rho b^2 n^{5/2} \quad (1.46)$$

where  $a$  is the gap size between the obstacles, and  $\rho$  is the obstacle density. The experimental separations are even faster and with higher resolution than the model prediction [111].

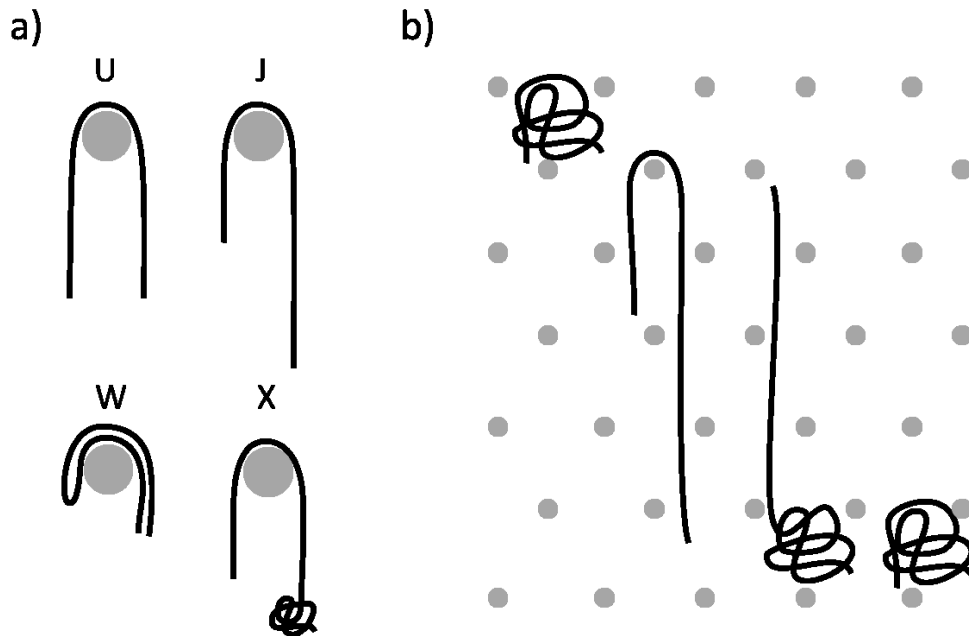


**Figure 1.6.** a) Schematic of several typical collisions of DNA with a single post. b) The geometration of long DNA in obstacle array with small gaps.

When the gap between obstacles is small, DNA interacts with the next post immediately downfield from its leading end. This interaction is a reasonable description of large DNA in an agarose gel. For this tight array regime, the term geometration was introduced by Deutsch [112, 113], regarding the dynamics as a repetitive cycle of collision, unhooking, and relaxation (Figure 1.6b). Simulations indicate that the mobility and dispersion in the geometration regime are independent of the molecular size, consistent with what people observe in gel electrophoresis under similar conditions [114].

In the reptation mechanism, hooking and hernias becomes significant when the scaled field  $\varepsilon_f \sim 1$  [15]. The probability of hernia

formation in larger pores or stronger field is not negligible. Thus, the key assumption of stretched DNA with negligible size fluctuation, used in developing the geometric model in the previous, section is challenged. The separation efficiency decreases, since the migration mechanism is more complicated. Moreover, the frequency of trapping also increases with field strength and DNA size. The trapping of large DNA, especially of Mbp size, even in relatively low field is a major challenge in both gel and microfluidic electrophoresis.

## **1.4 Separation Techniques**

### **1.4.1 Gel Electrophoresis**

Using a slab gel of agarose or polyacrylamide is the most conventional configuration of electrophoresis. Agarose gels are physically entangled polymer chains with monomeric units of agarobiose, a disaccharide made up of D-galactose and 3,6-anhydro-L-galactopyranose isolated from seaweed. Polyacrylamide or poly(2-propenamide) gel is formed from acrylamide linear polymer cross-linked by certain reagents, typically N,N'-methylenebisacrylamide.

Several interesting trials have been made recently to prepare a more ordered system of regular pores by patterning voids in a hydrogel [115, 116] or making an inverse opal from a colloidal crystal [117]. However, the

main stream slab gels are still highly hydrophilic porous network with disordered architecture and a random distribution of pore size. The concentration of agarose, or polyacrylamide and bis-acrylamide used in creating a gel determines the average pore size, thus the resolution, and the effective separation size range. The smaller the analytes, the smaller the pore size and the higher the gel concentration that should be used. Most electrophoresis in gels occurs under the Ogston sieving mechanism, while pulsed field gel electrophoresis (PFGE) is based on reptation. Entropic trapping also occurs because of the random distribution of pores, with some pores being large enough to be conformational entropic barriers. Agents such as sodium hydroxide or formamide are used to disrupt the hydrogen bonds and adsorption of DNA onto gel fibers. Affinity electrophoresis may be performed as well through ligand interaction of nucleic acids or fragments.

Generally, agarose gel has a larger pore size (0.1~1  $\mu\text{m}$ ) and can be used for the electrophoresis of DNA fragments ranging from 50 bp to several Mbp, using specialized apparatus. Most agarose gels are made with between 0.7% (for large 5–10 kbp fragments) and 2% (for small 0.2–1 kbp fragments) agarose dissolved in electrophoresis buffer. Up to 3% can be used for separating very tiny fragments but a disadvantage of high concentrations is the long running time (sometimes in days) [118]. Pulsed field gel electrophoresis (PFGE) often requires high percentage agarose

gels.

Polyacrylamide gel electrophoresis (PAGE) is used for separating particularly small DNA fragments. Traditional DNA sequencing techniques, such as Maxam-Gilbert or Sanger method, are used to separate DNA fragments with only a single base-pair difference in length, thanks to the uniform pore size and high resolution provided by polyacrylamide gel. PAGE is also capable of separating proteins ranging from 5 to 2,000 kDa. Typically, resolving gels are made in 6~15% concentration, with a 5% stacking gel poured on top and a gel comb inserted to form the wells and defines the lanes.

### **1.4.2 Capillary Electrophoresis**

Introduced in the 1960s, capillary electrophoresis (CE), also known as capillary zone electrophoresis (CZE), was first designed to separate ionic species based on their size to charge ratio in a thin capillary (typical inner diameter 20~100  $\mu\text{m}$ ) filled with an electrolyte solution under an electric field. In CE of DNA, however, the capillary should be filled with a sieving media, since DNA mobility is constant in free solution. This was done first by gelation inside the capillary in the late 1980s' to early 1990s' [119, 120]. then later moved to capillaries filled with replaceable polymer solutions [121]. The early history of DNA sequencing has been reviewed nicely by Dovichi [122].

Capillary DNA electrophoresis shares a similar sieving mechanism with gel electrophoresis, but with lower sample amount, higher resolution, sensitivity and speed. The efficiency of capillary electrophoresis benefits from the absence of mass transfer between phases and the flat flow profile of EOF. The use of arrays with typically about 100 capillaries instead of single capillaries allows capillary DNA sequencing instrumentation to function as a high-throughput system. Dovichi has developed instrumentation using 576 capillaries [122]. Substantial effort has also been directed toward miniaturizing DNA capillary electrophoresis into microfluidic chips. Mathies group did extensive work to miniaturize DNA sequencing into microfluidic chips with capillary or capillary arrays [38, 123-126].

There has been increasing research into other principles for sequencing, and efforts to replace the sieving matrix with other porous media. DNA sequencing by capillary electrophoresis in free electrolyte solutions has been conducted by labeling DNA with a protein or another monodisperse chemical to generate additional friction, as proposed by Mayer et al. [127], or utilizing sub-micron capillaries where the inner radius is smaller than the size of the electric double layer.[128] Contrary to the polymer media with natural random architecture in typical GE and CE, a promising new concept of microfabricated arrays has been tested and will be discussed in detail in the following section.

### **1.4.3 Micro-fluidic Devices**

As fabrication techniques have advanced [129], an increasing variety of micro- or nano-fluidic devices have been designed for DNA separation. With a combination of physics, engineering, and analytical chemistry, DNA electrophoresis in micro-fabricated devices is an intrinsically interdisciplinary topic. It is necessary to discuss critical features of those devices first in brief.

#### **1.4.3.1 Devices fabricated from top-down**

The most common substrates for micro-fabrication are silicon, glass, and plastic materials, including PDMS (polydimethylsiloxane). The typical procedure to fabricate silicon and glass devices, conventional lithography, is outlined in Figure 1.7a. First, a two-dimensional pattern of the channel structures is transferred onto a resist. Optical lithography is commonly used when the features required are no less than 1  $\mu\text{m}$ , since the resolution using ultraviolet light and photomask is limited by diffraction [130]. Extreme ultraviolet light (EUV) or X-rays can give higher resolution [131], but unfortunately impose difficulties including mask damage from the high beam energy, and the incompatibility with conventional optics. Instead, methods based on focused beams such as electron beam lithography (EBL) [132, 133] and focus ion beam (FIB) lithography [134] are more widely used. They are able to work on the scale of nanometers, commensurate with

the persistent length of dsDNA. Instead of masking procedures, these techniques are operated in the scanning mode by direct writing, which is extremely slow, and expensive for patterning large areas with features [135]. Using the interference of two or more coherent beams, interferometric lithography (IL) provides a means of fabricating wafer-scale uniform nanoscale features like lines and pillars. Nanoimprint lithography (NL) is also a route around the limitation of focused beam, by making a negative mode of the pattern by EBL [136, 137]. The mode is reusable to stamp the design onto the resist, and imprint the pattern on wafers many times.

Regardless of the approach used to pattern the wafer, after the developing stage that removes the exposed positive resist or the unexposed negative resist, the next step is to transfer the pattern on the resist to the substrate by etching, which controls the depth and landform of the channel. The region beneath the remaining resist pattern is protected from being corroded during etching. As a result, the bare region is etched into wells or channels. A dry etching approach such as reactive ion etching and deep trench etching is often used for tiny features. Wet etching, by dipping the substrate in an etchant solution or by electrochemical corrosion, is much simpler. Multilevel patterning and etching steps have been achieved to fabricate complex structures [138]. The etched substrate is then washed and bonded with a second flat substrate on top to create the final device (Figure

1.7a), possibly with prior surface modification steps such as thermal oxidation to convert surface Si to SiO<sub>2</sub>, or functionalization reactions.

Another major series of devices, PDMS substrate based chips were pioneered by the Whitesides group and have been used most widely [139]. As shown in Figure 1.7b, the first step is to make a mold that is a negative image of the structure. This is commonly done by optical lithography. The viscous PDMS mixed with cross-linker is poured over the mold, cured under heating, and then peeled off. The patterned PDMS is then sealed to a glass substrate. As the PDMS is shAPFEd by the resist left on the mold, the depth and features of channels are determined by the thickness and pattern

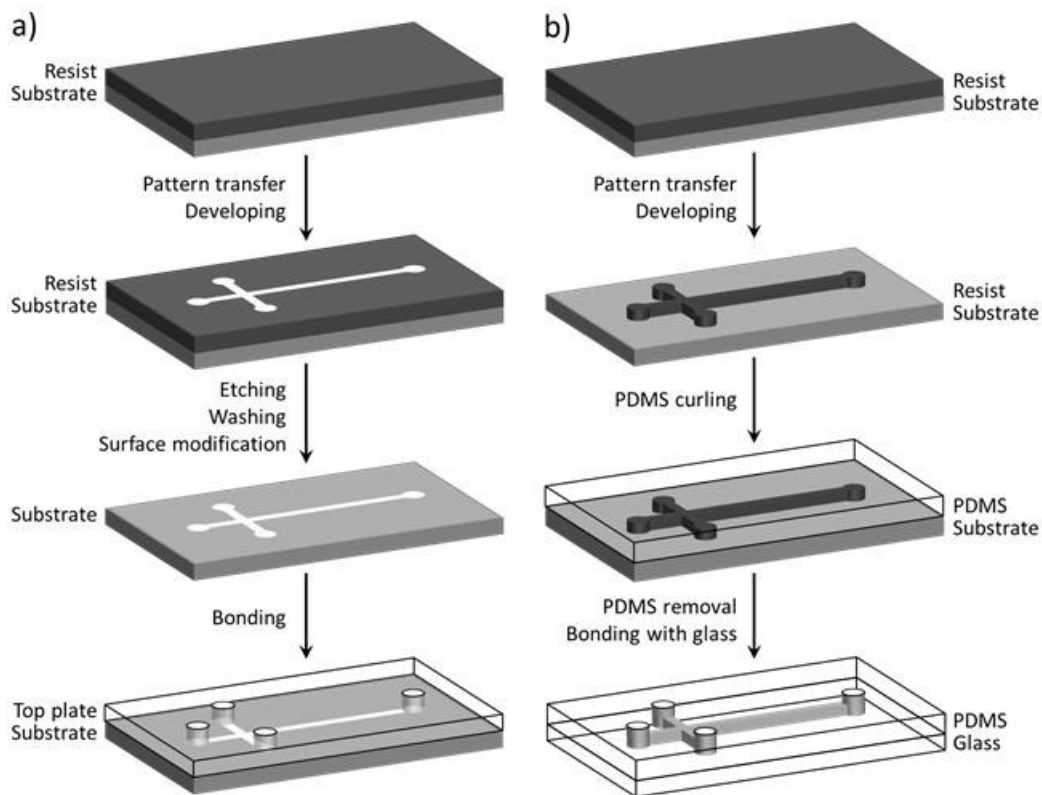


**Figure 1.7.** Schematic illustration of the general fabrication procedure of a) Si/glass chips, and b) PDMS chips.

of photoresist. The mold surface is coated with silane before used to assist the PDMS removal, and can be reused to create numbers of devices. Compared with conventional lithography, PDMS fabrication is an easy and inexpensive option for producing identical devices from one mold, although it is somehow troublesome since PDMS is porous and hydrophobic.

Top-down fabrication is the best choice to create a separation device with flexibly and precisely defined geometries. A huge category of microfluidic devices for DNA separation is the post array. Baba et.al fabricated a series of chips with nanopillars or nanowall arrays on quartz or silicon for conventional DNA electrophoresis and dynamics study [133, 140, 141]. An asymmetric post array developed in Han's group is capable of continuous DNA separation under an electric field [142]. The mechanism rises from the different rates and frequencies of the occasional jumps of coiled DNA between wide longitudinal channels through narrow transverse channels, which are governed by the entropic trapping mechanism (Figure 1.8b). Another interesting design is the entropic recoil device analogous to the trapping of very large DNA at the entrance to the gel in gel electrophoresis [132]. Austin and coworkers investigated a Brownian ratchet based separation of DNA using an asymmetric post array [143-145]. The structure rectifies the lateral Brownian motion of DNA molecules moving in the vertical direction under an electric field, and thereby deflects them based on their side-dependent diffusion. The same

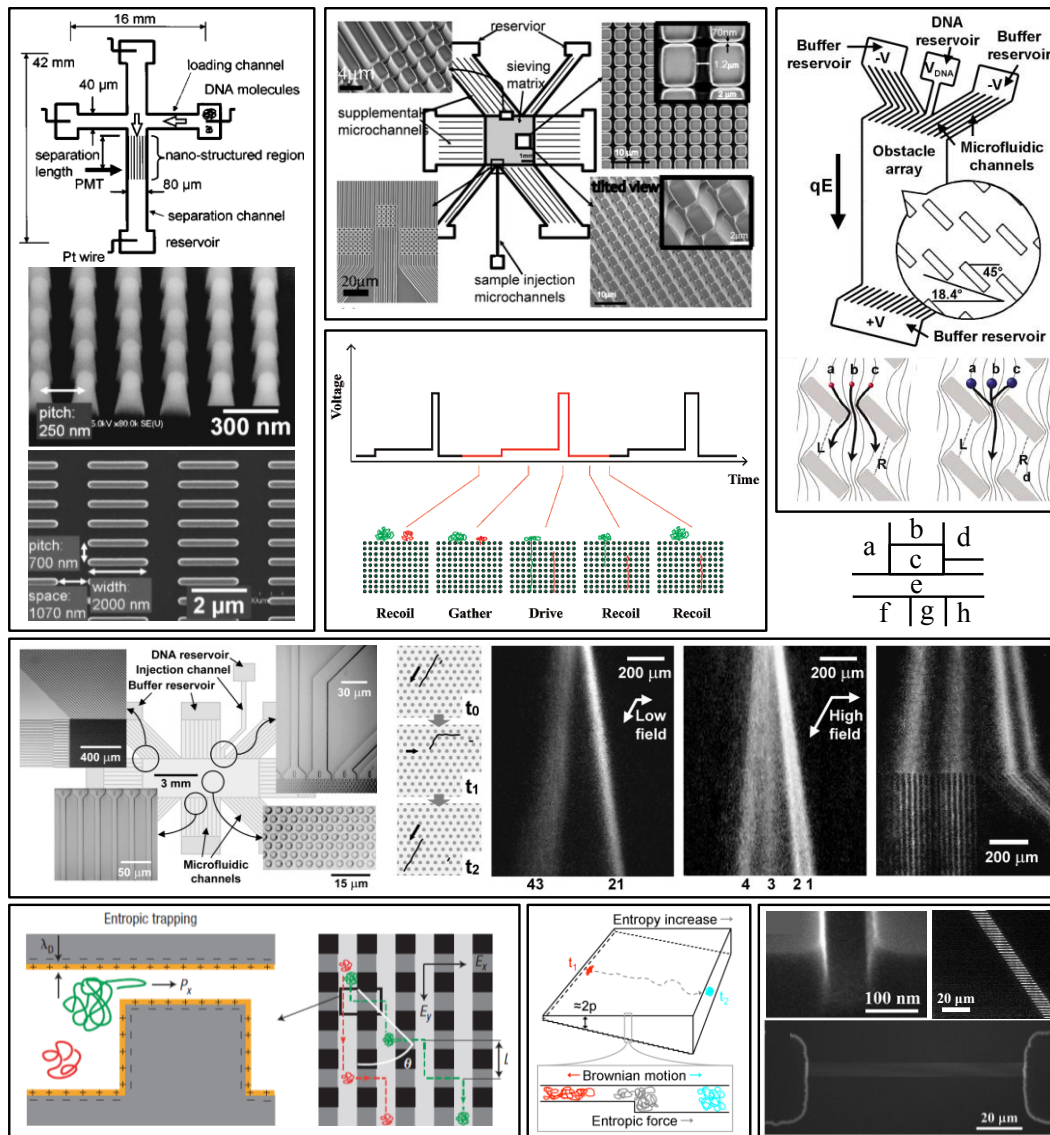


**Figure 1.8.** Microfabricated devices for DNA separation. a) Devices with nanopost or nanowall array [140]; b) Anisotropic array for continuous separation by entropic trapping [142]; c) An entropic recoil separation in a dense post array under pulsed field [132]; d) A Brownian ratchet device for continuous separation based on diffusivities [144]; e) A “DNA prism” device using asymmetric pulsed field to sort DNA into streams of different angles [43]; f) A nanofilter device for separating DNA and protein based on entropic trapping and sieving mechanisms [146]; g) A staircase slit device offering a powerful tool to study entropic effects [147]; h) The transport of  $\lambda$ -phage DNA in channels with 50 nm’s width [148].

group demonstrated a new approach called a “DNA prism”, using pillar arrays fabricated on silicon chips (Figure 1.8e) [43]. Asymmetric pulsed electric fields are applied to stretch long DNA coils around the pillars and sort them into flow streams of different angles [133]. From a fundamental perspective, microfabricated devices with periodic post arrays offer the key to test numbers of models idealizing gels as periodic lattices of obstacles.

Another category of devices with micro-slits have been attracting more and more attention. The key feature of slit configuration is the confinement in the slit is only in one or two dimensions. The slit-well motif, consisting of a staggered arrangement of deep well and shallow slit regions, is an ideal geometry for entropic trapping. The well region is usually at least as large as the size of DNA coil, so that molecules can relax therein. The slit depth is typically comparable with the Kuhn length of the DNA, requiring significant conformation change for DNA to migrate through when electric field is applied. In the entropic trapping separation by Han et al. [149, 150], the most impressive aspect of their device is the electrophoretic mobility counterintuitively increases with molecular weight. They further developed a novel slit sieving structure recently to separate DNA and proteins under pulsed field continuously by sieving and entropic trapping [146]. Strychalski et al. [147] designed a slit device with a staircase depth profile, and conducted an interesting observation on single DNA conformation change. A sub-nanometer channel was fabricated

through FIB milling and used to learn about single DNA molecule transport in tight constrains by Ramsey and Menard [148].

Despite progress, devices prepared by micro-fabrication share some common disadvantages. These include requiring sophisticated facilities, a clean-room for instance, time- and money-consuming procedures, and generally producing 2D architectures. Those issues impede the application to micro- or nanofluidic system on a routine basis. So far, most microfabricated structures were designed for large DNA molecules, due in part to technical challenges in lithographically accessing structures on the dimensions of smaller species such as proteins and some viruses.

#### **1.4.3.2 Devices fabricated from bottom-up**

The bottom-up fabrication method has been developed to avoid the time and cost required in microfabrication. The simplest approach is to imbed gel or monolithic porous matrix inside microchannels by gelation or polymerization on chip. However, self-assembly or self-organization has become a competitive alternative to the lithographic techniques. Starting from nanoscale building blocks, e.g. atoms, macromolecules, or colloid particles, self-assembly enables spontaneous formation of complex, three-dimensional ensembles with nanoscale features that are beyond the resolution and ability of current lithography techniques.

Colloidal self-assembly (CSA), the spontaneous organization of

particles, has been intensively used in various areas, such as the design of nanomaterials [73-76], photonics [77-80], colloidal lithography [81], and chemical and biological sensors [82,83]. It has attracted increasing attention in separation science because of their low cost of fabrication and unique, three-dimensional, well ordered nanostructures. A loosely packed crystalline lattice assembled by repulsive electrostatic interactions has been used as a template to fabricate an array of voids in a hydrogel [84]. The regularity of such void arrays made it possible to experimentally verify the entropic trapping effect, which is an important molecular migration mechanism that had lacked comprehensive study due to the random character of gels.

A well-developed CSA method is the micropost array assembled from magnetic beads studied by Viovy et.al. [31, 111] In the absence of a magnetic field, the paramagnetic beads have no magnetic moment and form

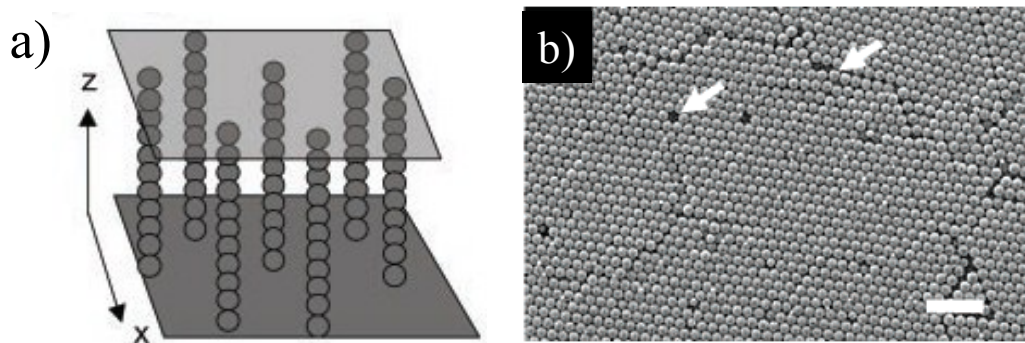


**Figure 1.9.** a) Schematic of the self-assembled posts of paramagnetic beads aligning with magnetic field [31]. b) SEM image of a hexagonally closed packed 2  $\mu\text{m}$  polystyrene colloidal array fabricated within a microchannel. The arrows indicate lattice defects. The scale bar is 10  $\mu\text{m}$  [41].

a homogeneous suspension, easily injected into microchannels. When an external uniform magnetic field is applied, the beads stack into columns orienting along the field lines, producing a quasi-hexagonal array in the channel. After electrophoresis, the magnetic field is turned off and the beads become suspension again which can be easily flushed away.

As the focus of this thesis, monodispersed colloids can be organized into close-packed crystalline arrays driven by the capillary force between the particles during solvent evaporation [151]. Such a structure features much higher mechanical strength compared to the non-close-packed systems mentioned above. Wirth [40] and Tinland [152] have used self-assembled silica crystalline arrays to study DNA electrophoretic behavior. Although it is hard to create defect-free crystalline structure over large areas, the matrix formed by this colloid self-assembly is sufficiently hexagonal ordered, and has succeeded in our group to separate DNA and proteins by CZE or APFE [41, 42, 44].

## 1.5 References

1. Hawkins, T.L., et al., *DNA sequencing - A magnetic attraction to high-throughput genomics*. Science, 1997. **276**(5320): p. 1887-1889.
2. Sharon, D., R. Chen, and M. Snyder, *Systems biology approaches to disease marker discovery*. Disease Markers, 2010. **28**(4): p. 209-224.
3. Moreno, C., et al., *Comparative Genomics for Detecting Human Disease Genes*. Genetic Dissection of Complex Traits, 2nd Edition, 2008. **60**: p. 655-697.
4. Michlmayr, A. and R. Oehler, *'OMICS': state of the art in vitro techniques employed in surgical research*. European Surgery-Acta

- Chirurgica Austriaca, 2010. **42**(3): p. 127-133.
5. van't Veer, L.J., et al., *Gene expression profiling predicts clinical outcome of breast cancer*. Nature, 2002. **415**(6871): p. 530-536.
  6. Hedenfalk, I., et al., *Gene-expression profiles in hereditary breast cancer*. New England Journal of Medicine, 2001. **344**(8): p. 539-548.
  7. Wang, D.J. and S. Bodovitz, *Single cell analysis: the new frontier in 'omics'*. Trends in Biotechnology, 2010. **28**(6): p. 281-290.
  8. van den Berg, A., H.G. Craighead, and P.D. Yang, *From microfluidic applications to nanofluidic phenomena*. Chemical Society Reviews, 2010. **39**(3): p. 899-900.
  9. Lee, C.C., T.M. Snyder, and S.R. Quake, *A microfluidic oligonucleotide synthesizer*. Nucleic Acids Research, 2010. **38**(8): p. 2514-2521.
  10. Wan, F., J. Zhang, and B. Chu, *Advances in electrophoretic techniques for DNA sequencing and oligonucleotide analysis*. Advances in Chromatography, Vol 47, 2009. **47**: p. 59-125.
  11. Cantor, C.R., et al., *DNA sequencing after the Human Genome Project*. Nucleosides & Nucleotides, 1997. **16**(5-6): p. 591-598.
  12. Shendure, J., *Next-generation human genetics*. Genome Biology, 2011. **12**(9).
  13. Shendure, J. and H.L. Ji, *Next-generation DNA sequencing*. Nature Biotechnology, 2008. **26**(10): p. 1135-1145.
  14. Ansorge, W.J., *Next-generation DNA sequencing techniques*. New Biotechnology, 2009. **25**(4): p. 195-203.
  15. Viovy, J.L., *Electrophoresis of DNA and other polyelectrolytes: Physical mechanisms*. Reviews of Modern Physics, 2000. **72**(3): p. 813-872.
  16. Noolandi, J., et al., *Self-trapping and anomalous dispersion of DNA in electrophoresis*. Physical Review Letters, 1987. **58**(23): p. 2428-2431.
  17. Slater, G.W. and J. Noolandi, *The biased reptation model of DNA gel-electrophoresis - Mobility vs molecular-size and gel concentration*. Biopolymers, 1989. **28**(10): p. 1781-1791.
  18. Zimm, B.H., *Lakes-straits model of field-inversion gel-electrophoresis of DNA*. Journal of Chemical Physics, 1991. **94**(3): p. 2187-2206.
  19. Southern, E.M., *Detection of specific sequences among DNA fragments separated by gel-electrophoresis*. Journal of Molecular Biology, 1975. **98**(3): p. 503-517.
  20. Panyim, S. and R. Chalkley, *High resolution acrylamide gel electrophoresis of histones*. Archives of Biochemistry and Biophysics, 1969. **130**(1-2): p. 337-346.

21. Loening, U.E., *Fractionation of high-molecular-weight ribonucleic acid by polyacrylamide-gel electrophoresis*. *Biochemical Journal*, 1967. **102**(1): p. 251-257.
22. Laurell, C.B., *Quantitative estimation of proteins by electrophoresis in agarose gel containing antibodies*. *Analytical Biochemistry*, 1966. **15**(1): p. 45-52.
23. Peacock, A.C. and C.W. Dingman, *Resolution of multiple ribonucleic acid species by polyacrylamide gel electrophoresis*. *Biochemistry*, 1967. **6**(6): p. 1818-1827.
24. Schwartz, D.C. and C.R. Cantor, *Separation of yeast chromosome-sized DNAs by pulsed field gradient gel-electrophoresis*. *Cell*, 1984. **37**(1): p. 67-75.
25. Bustamante, C., S. Gurrieri, and S.B. Smith, *Towards a molecular description of pulsed-field gel-electrophoresis*. *Trends in Biotechnology*, 1993. **11**(1): p. 23-30.
26. Verpoorte, E., *Microfluidic chips for clinical and forensic analysis*. *Electrophoresis*, 2002. **23**(5): p. 677-712.
27. Burns, M.A., et al., *An integrated nanoliter DNA analysis device*. *Science*, 1998. **282**(5388): p. 484-487.
28. Manz, A., N. Graber, and H.M. Widmer, *Miniaturized total chemical-analysis systems - a novel concept for chemical sensing*. *Sensors and Actuators B-Chemical*, 1990. **1**(1-6): p. 244-248.
29. Duke, T.A.J., et al., *Pulsed-field electrophoresis in microlithographic arrays*. *Electrophoresis*, 1996. **17**(6): p. 1075-1079.
30. Chou, H.P., et al., *A microfabricated device for sizing and sorting DNA molecules*. *Proceedings of the National Academy of Sciences of the United States of America*, 1999. **96**(1): p. 11-13.
31. Doyle, P.S., et al., *Self-assembled magnetic matrices for DNA separation chips*. *Science*, 2002. **295**(5563): p. 2237-2237.
32. Obreja, P., et al., *Polymer-based chips for surface plasmon resonance sensors*. *Journal of Optics a-Pure and Applied Optics*, 2008. **10**(6).
33. Liu, Y.X., N.C. Cady, and C.A. Batt, *A plastic microchip for nucleic acid purification*. *Biomedical Microdevices*, 2007. **9**(5): p. 769-776.
34. Fogarty, B.A., et al., *Rapid fabrication of poly(dimethylsiloxane)-based microchip capillary electrophoresis devices using CO<sub>2</sub> laser ablation*. *Analyst*, 2005. **130**(6): p. 924-930.
35. Margulies, M., et al., *Genome sequencing in microfabricated high-density picolitre reactors*. *Nature*, 2005. **437**(7057): p. 376-380.
36. Jung, B., R. Bharadwaj, and J.G. Santiago, *Thousandfold signal increase using field-amplified sample stacking for on-chip electrophoresis*. *Electrophoresis*, 2003. **24**(1920): p. 3476-3483.

37. Hopwood, A.J., et al., *Integrated microfluidic system for rapid forensic DNA analysis: Sample collection to DNA profile*. Analytical Chemistry, 2010. **82**(16): p. 6991-6999.
38. Liu, P. and R.A. Mathies, *Integrated microfluidic systems for high-performance genetic analysis*. Trends in Biotechnology, 2009. **27**(10): p. 572-581.
39. Zeng, Y., et al., *High-performance single cell genetic analysis using microfluidic emulsion generator arrays*. Analytical Chemistry, 2010. **82**(8): p. 3183-3190.
40. Zhang, H. and M.J. Wirth, *Electromigration of single molecules of DNA in a crystalline array of 300-nm silica colloids*. Analytical Chemistry, 2005. **77**(5): p. 1237-1242.
41. Zeng, Y. and D.J. Harrison, *Self-assembled colloidal arrays as three-dimensional nanofluidic sieves for separation of biomolecules on microchips*. Analytical Chemistry, 2007. **79**(6): p. 2289-2295.
42. Zeng, Y., M. He, and D.J. Harrison, *Microfluidic self-patterning of large-scale crystalline nanoarrays for high-throughput continuous DNA fractionation*. Angewandte Chemie-International Edition, 2008. **47**(34): p. 6388-6391.
43. Huang, L.R., et al., *A DNA prism for high-speed continuous fractionation of large DNA molecules*. Nature Biotechnology, 2002. **20**(10): p. 1048-1051.
44. Nazemifard, N., et al., *DNA dynamics in nanoscale confinement under asymmetric pulsed field electrophoresis*. Angewandte Chemie-International Edition, 2010. **49**(19): p. 3326-3329.
45. Calladine, C.R. and H.R. Drew, *Understanding DNA*. 1997, San Diego: Academic.
46. Bloomfield, V.A., D.M. Crothers, and I.J. Tinoco, *Nucleic acids: Structures, properties and functions*. 2000, Sausalito: University Science Books.
47. Doi, M., Edwards, S.F., *The theory of polymer dynamics*. 1986, New York: Oxford University.
48. Fixman, M. and J. Kovac, *Dynamics of stiff chains .2. Freely jointed chain*. Journal of Chemical Physics, 1974. **61**(12): p. 4950-4954.
49. Rodbard, D. and Chrambac. A, *Unified theory for gel electrophoresis and gel filtration*. Proceedings of the National Academy of Sciences of the United States of America, 1970. **65**(4): p. 970-977.
50. Baumann, C.G., et al., *Ionic effects on the elasticity of single DNA molecules*. Proceedings of the National Academy of Sciences of the United States of America, 1997. **94**(12): p. 6185-6190.
51. Flory, P.I., *Thermodynamics of high polymer solutions*. Journal of Chemical Physics, 1942. **10**(1): p. 51-61.

52. Flory, P.J. and S. Fisk, *Effect of volume exclusion on dimensions of polymer chains*. Journal of Chemical Physics, 1966. **44**(6): p. 2243-2248.
53. Slater, G.W., et al., *Deformation, stretching, and relaxation of single-polymer chains: Fundamentals and example*. Soft Materials, 2004. **2**(2-3): p. 155-182.
54. Rouse, P.E., *A theory of the linear viscoelastic properties of dilute solutions of coiling polymers*. Journal of Chemical Physics, 1953. **21**(7): p. 1272-1280.
55. Rubinstein, M. and R.H. Colby, *Polymer Physics*. 2003, New York: Oxford University Press.
56. Kenward, M. and G.W. Slater, *Molecular-dynamics simulations with explicit hydrodynamics - I: On the friction coefficients of deformed polymers*. European Physical Journal E, 2004. **14**(1): p. 55-65.
57. Zimm, B.H., *Dynamics of polymer molecules in dilute solution - Viscoelasticity, flow birefringence and dielectric loss*. Journal of Chemical Physics, 1956. **24**(2): p. 269-278.
58. Zimm, B.H., W.H. Stockmayer, and M. Fixman, *Excluded volume in polymer chains*. Journal of Chemical Physics, 1953. **21**(10): p. 1716-1723.
59. Reisner, W., et al., *Statics and dynamics of single DNA molecules confined in nanochannels*. Physical Review Letters, 2005. **94**(19).
60. Tegenfeldt, J.O., et al., *The dynamics of genomic-length DNA molecules in 100-nm channels*. Proceedings of the National Academy of Sciences of the United States of America, 2004. **101**(30): p. 10979-10983.
61. Brochard, F. and P.G. de Gennes, *Conformation of molten polymers inside small pores*. Journal De Physique Lettres, 1979. **40**(16): p. L399-L401.
62. Odijk, T., *On the statistics and dynamics of confined or entangled stiff polymers*. Macromolecules, 1983. **16**(8): p. 1340-1344.
63. Odijk, T., *Scaling theory of DNA confined in nanochannels and nanoslits*. Physical Review E, 2008. **77**(6).
64. Tegenfeldt, J.O., et al., *Stretching DNA in nanochannels*. Biophysical Journal, 2004. **86**(1): p. 596a-596a.
65. Maggs, A.C., *Two plateau moduli for actin gels*. Physical Review E, 1997. **55**(6): p. 7396-7400.
66. Morse, D.C., *Viscoelasticity of concentrated isotropic solutions of semiflexible polymers. 2. Linear response*. Macromolecules, 1998. **31**(20): p. 7044-7067.
67. Russel, W.B., D.A. Saville, and W.K. Schowalter, *Colloidal Dispersions*. 1989, Cambridge, UK: Cambridge University Press.
68. Masliyah, J.H. and S. Bhattacharjee, *Electrokinetic and colloid*

- transport phenomena*. 2005, Hoboken, New Jersey: Wiley Interscience.
69. Gibson, T.J. and M.J. Sepaniak, *Examination of band dispersion during size-selective capillary electrophoresis separations of DNA fragments*. *Journal of Chromatography B*, 1997. **695**(1): p. 103-111.
  70. Nkodo, A.E., et al., *Diffusion coefficient of DNA molecules during free solution electrophoresis*. *Electrophoresis*, 2001. **22**(12): p. 2424-2432.
  71. Slater, G.W., P. Mayer, and G. Drouin, *Migration of DNA through gels*. *High Resolution Separation and Analysis of Biological Macromolecules, Pt A*, 1996. **270**: p. 272-295.
  72. Stellwagen, E., Y.J. Lu, and N.C. Stellwagen, *Unified description of electrophoresis and diffusion for DNA and other polyions*. *Biochemistry*, 2003. **42**(40): p. 11745-11750.
  73. Slater, G.W., P. Mayer, and P.D. Grossman, *Diffusion, joule heating, and band broadening in capillary gel-electrophoresis of DNA*. *Electrophoresis*, 1995. **16**(1): p. 75-83.
  74. Tinland, B., *Dispersion coefficients of lambda DNA in agarose gels during electrophoresis by fringe recovery after photobleaching*. *Electrophoresis*, 1996. **17**(10): p. 1519-1523.
  75. Tinland, B., L. Meistermann, and G. Weill, *Simultaneous measurements of mobility, dispersion, and orientation of DNA during steady-field gel electrophoresis coupling a fluorescence recovery after photobleaching apparatus with a fluorescence detected linear dichroism setup*. *Physical Review E*, 2000. **61**(6): p. 6993-6998.
  76. Mohanty, U. and N.C. Stellwagen, *Free solution mobility of oligomeric DNA*. *Biopolymers*, 1999. **49**(3): p. 209-214.
  77. Hoagland, D.A., E. Arvanitidou, and C. Welch, *Capillary electrophoresis measurements of the free solution mobility for several model polyelectrolyte systems*. *Macromolecules*, 1999. **32**(19): p. 6180-6190.
  78. Bednar, J., et al., *Determination of DNA persistence length by cryoelectron microscopy - Separation of the static and dynamic contributions to the apparent persistence length of DNA*. *Journal of Molecular Biology*, 1995. **254**(4): p. 579-591.
  79. Slater, G.W. and S.Y. Wu, *Reptation, entropic trapping, percolation, and Rouse dynamics of polymers in random-environments*. *Physical Review Letters*, 1995. **75**(1): p. 164-167.
  80. Slater, G.W., et al., *Theory of DNA electrophoresis (similar to 1999-2002(1)/(2))*. *Electrophoresis*, 2002. **23**(22-23): p. 3791-3816.
  81. Slater, G.W., et al., *The theory of DNA separation by capillary electrophoresis*. *Current Opinion in Biotechnology*, 2003. **14**(1): p.

- 58-64.
82. Ogston, A.G., *The spaces in a uniform random suspension of fibres*. Transactions of the Faraday Society, 1958. **54**(11): p. 1754-1757.
  83. Morris, C.J., ed. *Protides of the Biological Fluids*, ed. H. Peeters. Vol. 14t. 1967, Elsevier: New York. 543-551.
  84. Chrambach, A., *The practice of quantitative gel electrophoresis*. 1985, Weinheim: VCH Verlagsgesellschaft.
  85. Mercier, J.F. and G.W. Slater, *Universal interpolating function for the dispersion coefficient of DNA fragments in sieving matrices*. Electrophoresis, 2006. **27**(8): p. 1453-1461.
  86. Long, D. and A. Ajdari, *A note on the screening of hydrodynamic interactions, in electrophoresis, and in porous media*. European Physical Journal E, 2001. **4**(1): p. 29-32.
  87. Baumgartner, A. and M. Muthukumar, *A trapped polymer-chain in random porous-media*. Journal of Chemical Physics, 1987. **87**(5): p. 3082-3088.
  88. Muthukumar, M. and A. Baumgartner, *Effects of entropic barriers on polymer dynamics*. Macromolecules, 1989. **22**(4): p. 1937-1941.
  89. Smisek, D.L. and D.A. Hoagland, *Electrophoresis of flexible macromolecules - Evidence for a new mode of transport in gels*. Science, 1990. **248**(4960): p. 1221-1223.
  90. Rousseau, J., G. Drouin, and G.W. Slater, *Entropic trapping of DNA during gel electrophoresis: Effect of field intensity and gel concentration*. Physical Review Letters, 1997. **79**(10): p. 1945-1948.
  91. Lerman, L.S. and H.L. Frisch, *Why does the electrophoretic mobility of DNA in gels vary with the length of the molecule*. Biopolymers, 1982. **21**(5): p. 995-997.
  92. Lumpkin, O.J. and B.H. Zimm, *Mobility of DNA in gel-electrophoresis*. Biopolymers, 1982. **21**(11): p. 2315-2316.
  93. de Gennes, P.G., *Reptation of a polymer chain in presence of fixed obstacles*. Journal of Chemical Physics, 1971. **55**(2): p. 572-579.
  94. Slater, G.W. and J. Noolandi, *On the reptation theory of gel-electrophoresis*. Biopolymers, 1986. **25**(3): p. 431-454.
  95. Slater, G.W. and J. Noolandi, *New biased-reptation model for charged polymers*. Physical Review Letters, 1985. **55**(15): p. 1579-1582.
  96. Lumpkin, O.J., P. Dejardin, and B.H. Zimm, *Theory of gel-electrophoresis of DNA*. Biopolymers, 1985. **24**(8): p. 1573-1593.
  97. Semenov, A.N., T.A.J. Duke, and J.L. Viovy, *Gel-electrophoresis of DNA in moderate fields - the effect of fluctuations*. Physical Review E, 1995. **51**(2): p. 1520-1537.
  98. Akerman, B., *Barriers to DNA loop formation in a porous matrix*. Progress in Biophysics & Molecular Biology, 1996. **65**: p. Pb144-

Pb144.

99. Akerman, B., *Tube leakage during electrophoresis retards reptating DNA in unmodified and hydroxyethylated agarose gels*. Physical Review E, 1996. **54**(6): p. 6697-6707.
100. Brahmasandra, S.N., et al., *Mobility, diffusion and dispersion of single-stranded DNA in sequencing gels*. Electrophoresis, 2001. **22**(6): p. 1046-1062.
101. Carle, G.F. and M.V. Olson, *Separation of chromosomal DNA-molecules from yeast by orthogonal-field-alternation gel-electrophoresis*. Nucleic Acids Research, 1984. **12**(14): p. 5647-5664.
102. Viovy, J.L., *Reptation-breathing theory of pulsed electrophoresis - dynamic regimes, antiresonance and symmetry breakdown effects*. Electrophoresis, 1989. **10**(5-6): p. 429-441.
103. Noolandi, J., et al., *Generalized tube model of biased reptation for gel-electrophoresis of DNA*. Science, 1989. **243**(4897): p. 1456-1458.
104. Slater, G.W. and J. Noolandi, *Effect of nonparallel alternating-fields on the mobility of DNA in the biased reptation model of gel-electrophoresis*. Electrophoresis, 1989. **10**(5-6): p. 413-428.
105. Akerman, B. and M. Jonsson, *Reorientational dynamics and mobility of DNA during pulsed-field agarose-gel electrophoresis*. Journal of Physical Chemistry, 1990. **94**(9): p. 3828-3838.
106. Gurrieri, S., et al., *Real-time imaging of the reorientation mechanisms of YOYO-labelled DNA molecules during 90 degrees and 120 degrees pulsed field gel electrophoresis*. Nucleic Acids Research, 1996. **24**(23): p. 4759-4767.
107. Randall, G.C. and P.S. Doyle, *Electrophoretic collision of a DNA molecule with an insulating post*. Physical Review Letters, 2004. **93**(5).
108. Andre, P., D. Long, and A. Ajdari, *Polyelectrolyte/post collisions during electrophoresis: Influence of hydrodynamic interactions*. European Physical Journal B, 1998. **4**(3): p. 307-312.
109. Randall, G.C. and P.S. Doyle, *Collision of a DNA polymer with a small obstacle*. Macromolecules, 2006. **39**(22): p. 7734-7745.
110. Patel, P.D. and E.S.G. Shaqfeh, *A computational study of DNA separations in sparse disordered and periodic arrays of posts*. Journal of Chemical Physics, 2003. **118**(6): p. 2941-2951.
111. Minc, N., et al., *Quantitative microfluidic separation of DNA in self-assembled magnetic matrixes*. Analytical Chemistry, 2004. **76**(13): p. 3770-3776.
112. Deutsch, J.M., *Theoretical-studies of DNA during gel-electrophoresis*. Science, 1988. **240**(4854): p. 922-924.

113. Deutsch, J.M. and T.L. Madden, *Theoretical-studies of DNA during gel-electrophoresis*. Journal of Chemical Physics, 1989. **90**(4): p. 2476-2485.
114. Popelka, S., et al., *Peak dispersion due to geometration motion in gel electrophoresis of macromolecules*. Journal of Chromatography A, 1999. **838**(1-2): p. 45-53.
115. Khetan, S. and J.A. Burdick, *Patterning network structure to spatially control cellular remodeling and stem cell fate within 3-dimensional hydrogels*. Biomaterials, 2010. **31**(32): p. 8228-8234.
116. Wosnick, J.H. and M.S. Shoichet, *Three-dimensional chemical Patterning of transparent hydrogels*. Chemistry of Materials, 2008. **20**(1): p. 55-60.
117. Colvin, V.L., *From opals to optics: Colloidal photonic crystals*. MRS Bulletin, 2001. **26**(8): p. 637-641.
118. Lewis, M. *Agarose gel electrophoresis (basic method)*. Biological Protocols [Web Page] 2011 [cited 2012 Aug. 15]; Available from: <http://www.methodbook.net/dna/agarogel.html>.
119. Cohen, A.S., et al., *Rapid separation of DNA restriction fragments using capillary electrophoresis*. Journal of Chromatography, 1988. **458**: p. 323-333.
120. Drossman, H., et al., *High-speed separations of DNA sequencing reactions by capillary electrophoresis*. Analytical Chemistry, 1990. **62**(9): p. 900-903.
121. Ruizmartinez, M.C., et al., *DNA-sequencing by capillary electrophoresis with replaceable linear polyacrylamide and laser-induced fluorescence detection*. Analytical Chemistry, 1993. **65**(20): p. 2851-2858.
122. Dovichi, N.J., *DNA sequencing by capillary electrophoresis*. Electrophoresis, 1997. **18**(12-13): p. 2393-2399.
123. Woolley, A.T. and R.A. Mathies, *Ultra-high-speed DNA-sequencing using capillary electrophoresis chips*. Analytical Chemistry, 1995. **67**(20): p. 3676-3680.
124. Liu, S.R., et al., *Optimization of high-speed DNA sequencing on microfabricated capillary electrophoresis channels*. Analytical Chemistry, 1999. **71**(3): p. 566-573.
125. Mathies, R.A. and X.C. Huang, *Capillary array electrophoresis - an approach to high-speed, high-throughput DNA sequencing*. Nature, 1992. **359**(6391): p. 167-169.
126. Huang, X.C., M.A. Quesada, and R.A. Mathies, *Capillary array electrophoresis - an approach to high-speed, high-throughput DNA-sequencing*. Proceedings of Advances in DNA Sequencing Technology, 1993. **1891**: p. 12-20.
127. Mayer, P., G.W. Slater, and G. Drouin, *Theory of DNA-sequencing*

- using free-solution electrophoresis of protein-DNA complexes.* Analytical Chemistry, 1994. **66**(10): p. 1777-1780.
128. Napoli, M., J.C.T. Eijkel, and S. Pennathur, *Nanofluidic technology for biomolecule applications: a critical review.* Lab on a Chip, 2010. **10**(8): p. 957-985.
  129. Mijatovic, D., J.C.T. Eijkel, and A. van den Berg, *Technologies for nanofluidic systems: top-down vs. bottom-up - a review.* Lab on a Chip, 2005. **5**(5): p. 492-500.
  130. Chan, Y.C., et al., *Design and fabrication of an integrated microsystem for microcapillary electrophoresis.* Journal of Micromechanics and Microengineering, 2003. **13**(6): p. 914-921.
  131. Naulleau, P., et al., *Sub-70 nm extreme ultraviolet lithography at the Advanced Light Source static microfield exposure station using the engineering test stand set-2 optic.* Journal of Vacuum Science & Technology B, 2002. **20**(6): p. 2829-2833.
  132. Cabodi, M., S.W.P. Turner, and H.G. Craighead, *Entropic recoil separation of long DNA molecules.* Analytical Chemistry, 2002. **74**(20): p. 5169-5174.
  133. Kaji, N., et al., *Separation of long DNA molecules by quartz nanopillar chips under a direct current electric field.* Analytical Chemistry, 2004. **76**(1): p. 15-22.
  134. Campbell, L.C., et al., *Electrophoretic manipulation of single DNA molecules in nanofabricated capillaries.* Lab on a Chip, 2004. **4**(3): p. 225-229.
  135. Shi, J., et al., *Highly parallel mix-and-match fabrication of nanopillar arrays integrated in microfluidic channels for long DNA molecule separation.* Applied Physics Letters, 2007. **91**(15).
  136. Chou, S.Y., P.R. Krauss, and P.J. Renstrom, *Nanoimprint lithography.* Journal of Vacuum Science & Technology B, 1996. **14**(6): p. 4129-4133.
  137. Chou, S.Y., P.R. Krauss, and P.J. Renstrom, *Imprint lithography with 25-nanometer resolution.* Science, 1996. **272**(5258): p. 85-87.
  138. Han, J. and H.G. Craighead, *Entropic trapping and sieving of long DNA molecules in a nanofluidic channel.* Journal of Vacuum Science & Technology a-Vacuum Surfaces and Films, 1999. **17**(4): p. 2142-2147.
  139. Duffy, D.C., et al., *Rapid prototyping of microfluidic systems in poly(dimethylsiloxane).* Analytical Chemistry, 1998. **70**(23): p. 4974-4984.
  140. Baba, M., et al., *DNA size separation using artificially nanostructured matrix.* Applied Physics Letters, 2003. **83**(7): p. 1468-1470.
  141. Yasui, T., et al., *DNA separation in nanowall array chips.* Analytical

- Chemistry, 2011. **83**(17): p. 6635-6640.
142. Mao, P. and J. Han, *Massively-parallel ultra-high-aspect-ratio nanochannels as mesoporous membranes*. Lab on a Chip, 2009. **9**(4): p. 586-591.
  143. Duke, T.A.J. and R.H. Austin, *Microfabricated sieve for the continuous sorting of macromolecules*. Physical Review Letters, 1998. **80**(7): p. 1552-1555.
  144. Huang, L.R., et al., *Tilted Brownian ratchet for DNA analysis*. Analytical Chemistry, 2003. **75**(24): p. 6963-6967.
  145. Huang, L.R., et al., *Role of molecular size in ratchet fractionation*. Physical Review Letters, 2002. **89**(17).
  146. Fu, J.P., et al., *A patterned anisotropic nanofluidic sieving structure for continuous-flow separation of DNA and proteins*. Nature Nanotechnology, 2007. **2**(2): p. 121-128.
  147. Stavis, S.M., et al., *DNA molecules descending a nanofluidic staircase by entropophoresis*. Lab on a Chip, 2012. **12**(6): p. 1174-1182.
  148. Menard, L.D. and J.M. Ramsey, *Fabrication of sub-5 nm nanochannels in insulating substrates using focused ion beam milling*. Nano Letters, 2011. **11**(2): p. 512-517.
  149. Han, J., S.W. Turner, and H.G. Craighead, *Entropic trapping and escAPFE of long DNA molecules at submicron size constriction*. Physical Review Letters, 1999. **83**(8): p. 1688-1691.
  150. Han, J. and H.G. Craighead, *Separation of long DNA molecules in a microfabricated entropic trap array*. Science, 2000. **288**(5468): p. 1026-1029.
  151. Denkov, N.D., et al., *2-Dimensional Crystallization*. Nature, 1993. **361**(6407): p. 26-26.
  152. Meistermann, L. and B. Tinland, *DNA electrophoresis in a monodisperse porous medium*. Physical Review E, 2000. **62**(3): p. 4014-4017.

# Chapter 2

## DNA Electrophoresis in Nanoparticle Arrays with Pore Size Gradient\*

---

### 2.1 Introduction

Pulsed field electrophoresis (PFE) has been established as the standard method to separate large DNA molecules [1-3]. As large molecules exhibit biased reptation behavior during electrophoresis, they cannot be separated in a continuous field as that mode requires the Ogston sieving mechanism be operational [3]. Different separation media for PFE have been investigated. Austin and co-workers developed a structure they called a DNA prism to separate DNA via a mechanism in which the DNA chain reorients itself according to the pulsing field and undergoes head to tail switching [4]. They also accomplished separation using a ratchet fractionation of DNA molecules in microfluidic devices within an obstacle array [5]. Both of the DNA separation mechanisms involve physical rather than chemical interactions with the separation media.

---

\* A version of this chapter has been published as an extended abstract in MicroTAS 2010, Groningen, the Netherlands. The work was done in collaboration with co-authors, Neda Nazemifard and Ledi Wang. A version of the submitted manuscript appears in their thesis as well. My role includes device fabrication, electrophoresis experiments and data analysis. A version of the submitted manuscript appears in their thesis as well.

Spontaneous organization of nanoparticles, referred to as colloidal self-assembly (CSA), is simple and cost-effective for creating three-dimensional nanostructures. Using the CSA approach with silica particles, a microfluidic device has been developed in our group for continuous two-dimensional separation of DNA under pulsed electric fields[6]. Our further studies concluded that the separation mechanism relies on the comparison of the pulse period to reorientation time of DNA molecules with different sizes, longer for larger molecules relative to smaller ones [7], consistent with the original work of Austin's group [4, 5].

Within porous sieving media, it is recognized that a single pore size can only be optimized for a certain range of molecular size, with low resolution for samples outside that range [3]. In other words, the peak capacity is limited by the efficient range of a given pore size, as well as bandwidths of the peaks within this range, making the separation of DNA mixtures containing both large and small molecules challenging. Structures with ordered pore gradients have already been used in chromatography and packed bed filtration to enhance peak capacity [8]. As to the ratchet mechanism developed by Austin and co-workers, a microarray structure with array gradients was proved to be capable of separating a range of particle sizes [9]. The study described in this chapter employs a gradient of ordered porous CSA matrices, making it able to expand the efficient separation range of DNA size while preserving the advantage of having a

high degree of order in the structure [10].

## **2.2 Experimental**

### **2.2.1 DNA separation microchip**

DNA separation was conducted using a microfluidic chip filled with an array of nanoparticles as the sieving matrix. PDMS microchips were fabricated using a standard soft lithography technique as described in Section 1.4.3 [6], using a positive photoresist master (AZ-4620, Clariant Corp. Charlotte, NC, USA) UV patterned on a 4-inch silicon wafer. The mold was silanized to facilitate PDMS removal. Negative PDMS replicas were made by pouring a 10:1 (m:m) mixture of PDMS base (Sylgard 184, Dow Corning, Midland, MI, USA), with the curing agent over the mold, followed by incubation at 60 °C overnight. PDMS replicas were removed from the master, reservoirs were punched to access channels and the device was then sealed to clean glass slides prior to packing. The chip design is schematically shown in Figure 2.1a. The separation chamber is 4 × 4 mm. Channels are ~100 μm wide, ~20 μm deep and ~4 mm long.

Aqueous suspensions of monodisperse silica colloids (Bangs Laboratories, Fishers, IN, USA) of nominally 100 nm, 330 nm, and 700 nm diameter were used to form the self-assembled nanoparticle array inside the microchips. Particle suspensions were ultrasonicated for 10~15 min prior to

use, with the concentration (5~20% w/v) optimized for each particle size. Figure 2.1b schematically outlines the steps taken to fabricate the self-assembled structures. From 10~15  $\mu\text{L}$  of a colloidal suspension was injected, filling the channels spontaneously, forming a liquid meniscus at the outlet of the channel in open reservoirs. Once all channels were filled, all the reservoirs except one were sealed with a PDMS cover to prevent solvent evaporation. Solvent evaporation at the open reservoir induced colloidal self-assembled packing within the channels, with a supply of particle suspension from the closed reservoirs.

The growth of the array can be terminated by replacing the suspension in the reservoir with water. In our previous work with monodisperse CSA arrays without a gradient, the packing was stopped only after the whole microchip was filled by the array, as illustrated by the column on the left in Figure 2.1b. A stepwise packing scheme was used for gradient separation chips: the separation chamber was partially packed with one size of particles, and once the packed zone filled a half region of the whole chamber, the suspension in the surrounding reservoirs was switched to the second particle size suspension, in order to pack the remainder of the chamber. (The right column in Figure 2.1b) The liquid in the reservoirs was substituted with the running buffer and left to equilibrate for at least half an hour before separation. The yield of chip for successful usage is 70~80%. For SEM observation, packed chips were dried completely and the PDMS

pieces were removed before sputtering with a Au metal layer.

## 2.2.2 Asymmetric pulsed field electrophoresis

DNA samples, NoLimits™ DNA fragments (6, 10, 20 kbp, Fermentas Life Sciences, Thermo Fisher Scientific, Waltham, MA, USA),  $\lambda$ -DNA (48 kbp, New England Biolabs Ipswich, MA, USA), and T4

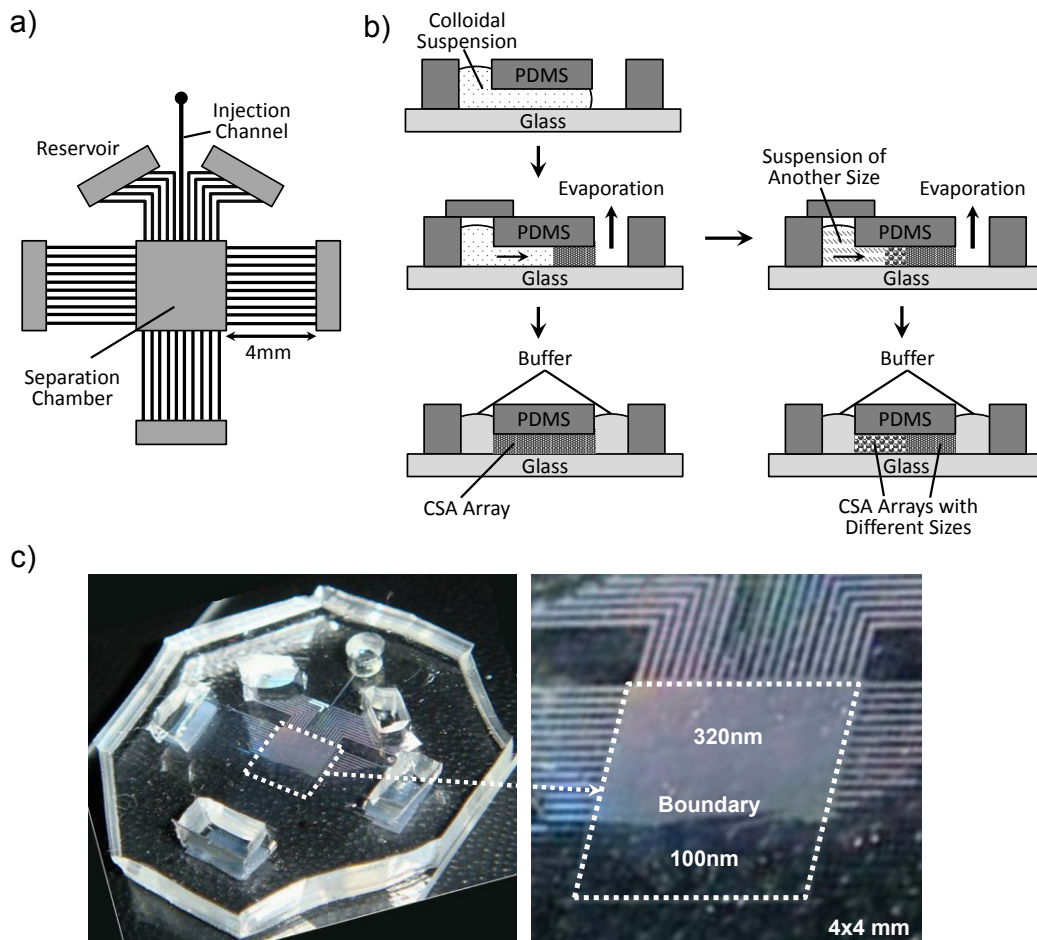


**Figure 2.1.** a) Schematic of the chip design for continuous angular separation by asymmetric pulsed field electrophoresis. b) The packing process of CSA arrays without (left column) and with pore size gradient (right column). c) A photo of a chip packed with silica particle array of 320-100 nm gradient.

DNA (166 kbp, Nippon Gene, Tokyo, Japan) were stained by YOYO-1 (Molecular Probes, Life Technologies, Grand Island, NY, USA) with dye-to-base ratio of 1:10. Pulsed field electrophoresis was performed in 4× TBE buffer to suppress electroosmotic flow with 4% v/v 2-mercaptoethanol added to reduce photobleaching.

Pulsed electric fields were generated by homebuilt high-voltage amplifiers triggered by square wave signals from a synthesized function generator (Wavetek, San Diego, CA). The separation chamber was connected to reservoirs where pulsed electric potentials were applied using platinum electrodes. The applied pulsed electric potentials generated asymmetric obtuse-angle pulsed fields,  $E_1$  and  $E_2$ , across the separation chamber, where the angle between the pulsed fields is  $135^\circ$  and  $E_1 = \sqrt{2}E_2$  in all our experiments. (Figure 2.2a) Typical electric fields used in these experiments are around 80~280 V/cm and the frequencies are between 0.1 to 100 Hz.

Angular separation of DNA molecules was conducted by continuously injecting DNA samples into the separation chamber by applying a DC electric field in the DNA sample reservoir. Once reaching the separation chamber, the DNA molecules under pulsed electric field split into streams along different angles according to their sizes, following the mechanism described in Section 1.3.2.

DNA samples were excited by a 488 nm argon ion laser beam, and

the fluorescent emission was collected with a homemade microscope using a 4× objective (0.1 N.A., Olympus, Tokyo, Japan) for separation and visualized by a CCD camera (StellaCam 2, Astrovid, Glens Falls, NY, USA) controlled by VisualDub installed in a PC. The separation angle  $\theta$  (the angle of the DNA flow relative to the vertical line) and bandwidth were measured from fluorescent images captured by ImageJ (NIH, <http://rsb.info.nih.gov/ij/>).

## **2.3 Results and discussion**

### **2.3.1 Angular separation in monodisperse CSA**

Previous results, reconfirmed by several studies with freshly prepared devices showed that, for larger DNA molecules, better separation was achieved at lower frequencies and in structures with larger pore sizes. For smaller DNA molecules, better separation was achieved at higher frequencies and in smaller pore sizes[6, 7]. For a mixture of four sizes of double stranded DNA (2, 6, 10, 20 kbp), the packed structure of 100 nm particles (Figure 2.2b) provided a better separation for the two smaller DNA molecules, failing to resolve the two larger sizes even at its optimum condition  $E = 160$  V/cm,  $f = 5$  Hz. The packed structure of 320 nm particles (Figure 2.2c) provides separation for the two larger DNA fragments, failing to resolve the two smaller sizes at optimum field  $E = 160$  V/cm,  $f = 20$  Hz.

As a result, each combination of pore size and frequency provides separation of a certain range of DNA sizes.

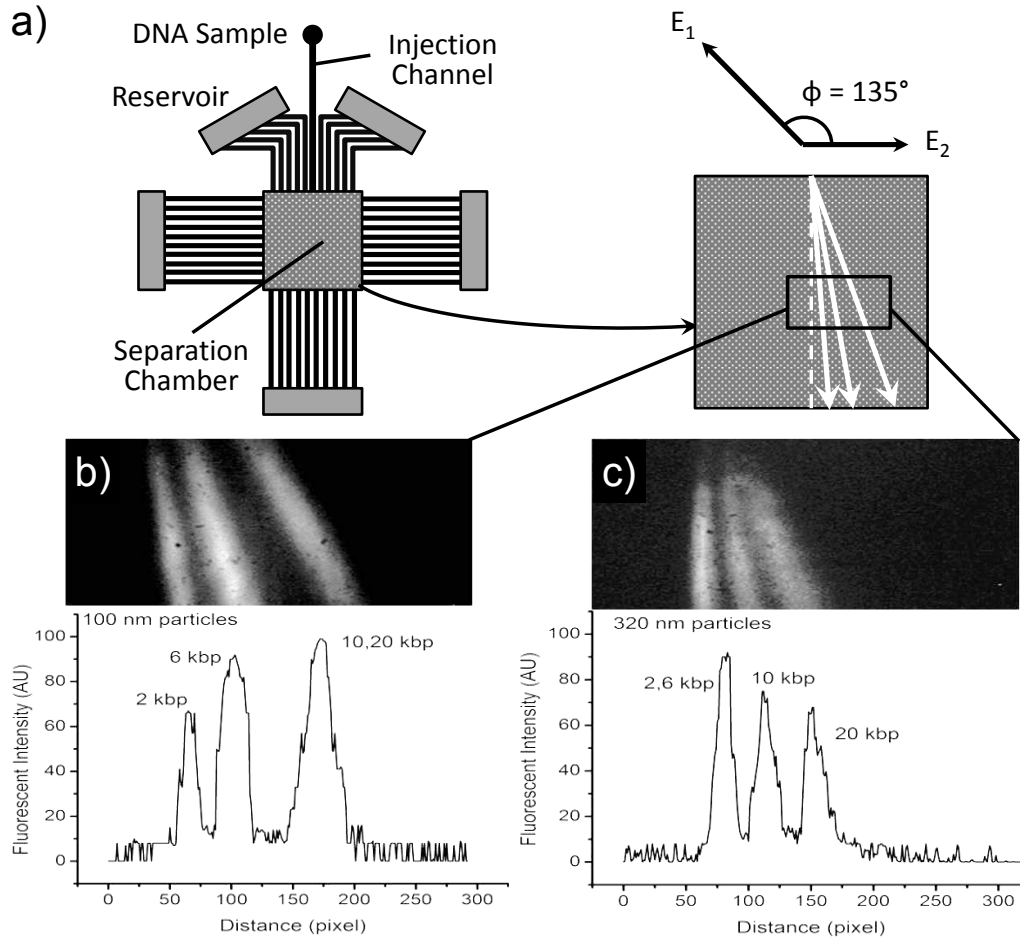


**Figure 2.2.** a) Schematic of the angular separation. DNA samples are continuously injected into the separation chamber filled with silica CSA arrays. Pulsed electric fields  $E_1, E_2$  shown on the right are applied across the chamber. Larger DNA have larger deflection angle ( $\theta$ ) relative to the vertical line. Fluorescent images and intensity profiles of optimized separations of 4 DNA mixture (2, 6, 10, 20 kbp) in arrays of b) 100 nm particles at  $E_1 = 160$  V/cm,  $f = 5$  Hz and c) 320 nm at  $E_1 = 160$  V/cm,  $f = 20$  Hz are shown.

### 2.3.2 Characterization of particle arrays

Using the stepwise packing scheme described in Section 2.2.1, different combinations of particle sizes, i.e., 700 vs. 320 nm, 320 vs. 100 nm, or 900 vs. 540 nm were used to create layers of different, ordered pore sizes inside the separation chamber. SEM images were captured within the

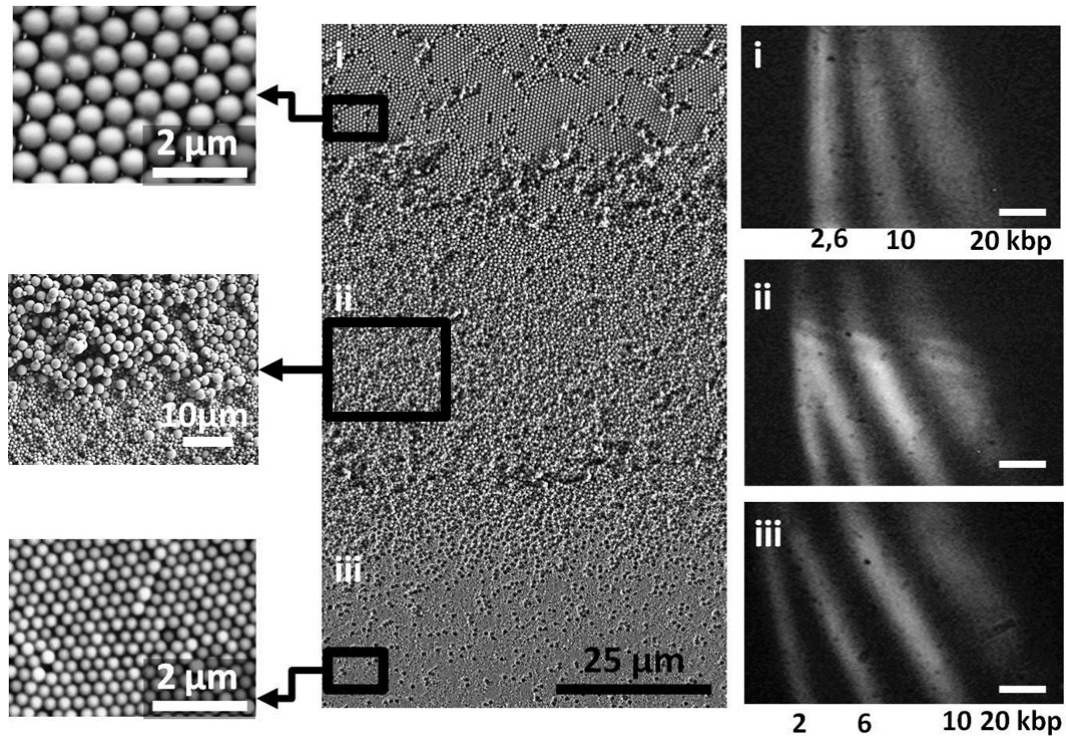


**Figure 2.3.** Centre column: SEM image of the separation chamber. Numbering scheme (i. ii. iii) refer to the larger, boundary and smaller particle packed regions. The top part of the separation chamber is packed with 700 nm particles (i), the middle part is the interface (ii), the bottom part of the separation chamber is packed with 320 nm particles. (iii). Left column: zoomed-in SEM images of the three regions. Right column: fluorescence images of the separation of four sizes of DNA (2, 6, 10, and 20 kbp) injected into the chamber in regions (i) 320 nm particle, (ii) the interface, (iii) 100 nm particle. Scale bar is 50  $\mu\text{m}$ .  $E_l = 160 \text{ V/cm}$ ,  $f = 15 \text{ Hz}$ .

regions of the two sizes, as well as at the boundary between the two zones.

The left column in Figure 2.3 shows an SEM image of a separation chamber packed by 700 and 320 nm particles using the stepwise packing scheme. The top part of this image (i) is packed with 700 nm particles, the middle part (ii) is the interface, and the bottom part (iii) is packed with 320 nm particles. It can be seen from the two enlarged SEM images that both top and bottom zones have an ordered structure and fairly well defined pore sizes. SEM images of the monodisperse region of the CSA structures revealed a closely packed hexagonal array of nanoparticles, where the size of the pores ( $d_p$ ) were around 15% of the particle size i.e.,  $d_p \approx 15$  nm, 50 nm, and 105 nm for 100 nm, 330 nm, and 700 nm particles, respectively[11]. The boundary is sharp to the naked eye, but under SEM magnification, the structure switches from pure large particle to pure small particle occurs across tens of microns at the interface.

### **2.3.3 Angular separation within pore size gradient**

The right column in Figure 2.3 shows an example of DNA separation in a gradient structure of two particles. The separation chamber for this experiment was packed with 320 and 100 nm particles. It can be seen from the top image that while 10 and 20 kbp DNA molecules were separated, 2 and 6 kbp DNA appear as one stream in the 320 nm array. Once entering the array of 100 nm particles, streams of the two smaller

DNA split, while the separation of the two larger streams is retained, even though the bands change their orientation angle and become slightly broader. Some band broadening is observed at the interface, but the separation, achieved in the upstream region of 10 and 20 kbp DNA remains parallel downstream of the interface, since the horizontal displacement of the streams is retained, even though no further improvement will occur. Overall, the results show that the four different sizes of DNA, which could not be completely separated in the two respective constant pore structures (Figure 2.2), can be resolved by creating a pore size step change or gradient in our separation device. It should be noted that the SEM images of Figure 2.3 are taken in a 700/320 nm silica CSA structure, since the instrument we used cannot resolve particles as small as 100 nm. However, the configuration of 320/100 nm gradient packing is a reasonable analogy to 700/320 nm array because of similar size ratio.

The maximum sample diversity was four, with a minimum size increment of 4 kbp in all of our previous experiments in all devices of this type. To further promote the separation performance of this new gradient design, six different DNA sizes (2, 4, 6, 10, 15 and 20 kbp) were prepared, and injected in beds of 320/100 nm particles. As control experiments, the separation in 320 and 100 nm constant structures is shown in the left column of Figure 2.4. For the mixture of six sizes, the packed structures of 100 nm particles (Figure 2.4b) provided a better separation for the smaller

DNA molecules, especially for size 2 and 4 kbp, while the packed structure of 320 nm particles (Figure 2.4a) provided a better separation for the larger DNA pieces of 6, 10, 15 and 20 kbp. As a result, each combination of pore size provided separation of a certain range of DNA sizes, and neither structure resolved all components. The right column of Figure 2.4 is the separation in a 320/100 nm gradient bed. With 320/100 nm bed, the separation of DNA sizes varying from 2 to 20 kbp, with a minimum

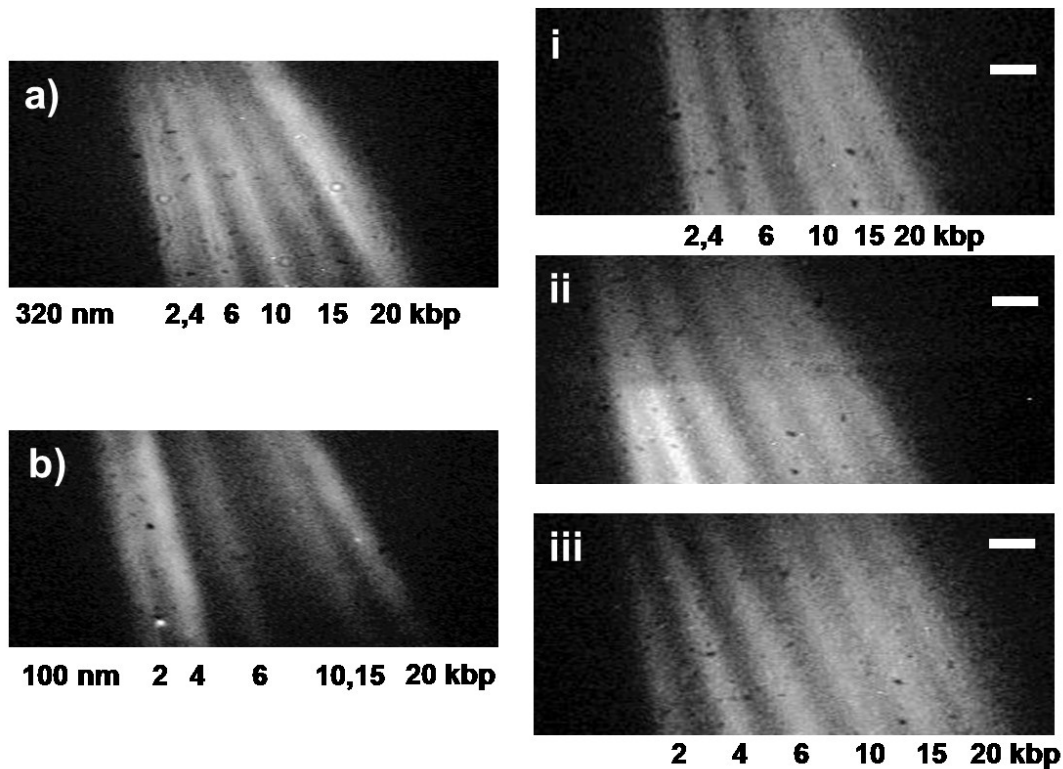


**Figure 2.4.** Two-dimensional separation of six different sizes of DNA (2, 4, 6, 10, 15, 20 kbp) in a) 320nm, b) 100 nm structures, and with 320/100 nm size gradient at  $E_l = 280$  V/cm,  $f = 15$  Hz. i: the separation at the top of separation chamber packed with 320 nm particles. ii: the separation at the interface. iii: the separation at the bottom of the separation chamber packed with 100 nm particles.

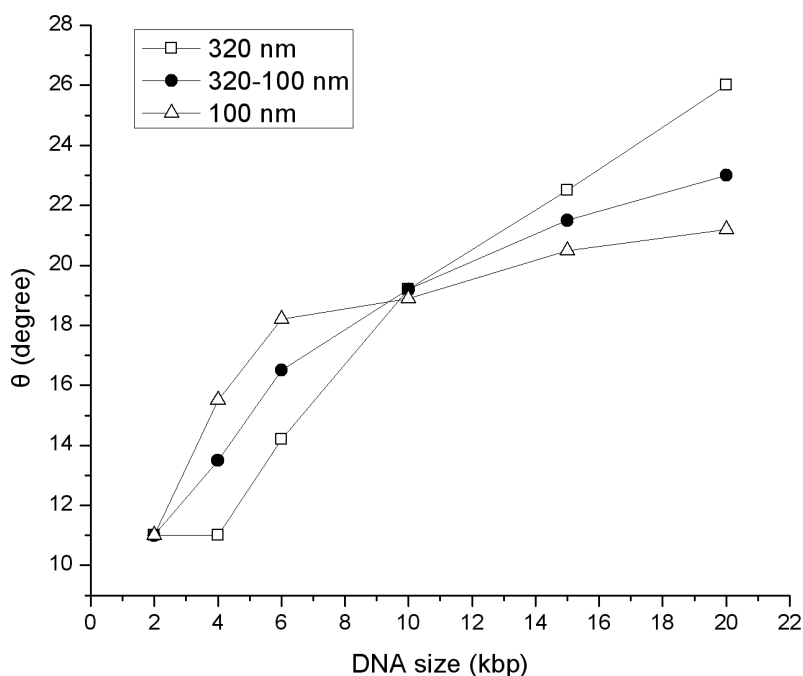


**Figure 2.5.** Analysis of the deflection angle  $\theta$  in 320 nm (hollow square), 100 nm (hollow triangle) and 320/100 nm gradient (solid circle) arrays at  $E_1 = 280\text{V/cm}$ ,  $f = 15\text{Hz}$ .

increment of 2 kbp, was achieved.

The deflection angle  $\theta$  defines the continuous separation shown in Figure 2.4, and was analyzed by the software ImageJ as shown in Figure

2.5, to provide detail about the separations. The angle was measured in the middle of the separation chamber ( $\sim 2$  mm from the injection entrance) where the electric field is more uniform. For the 100 nm array, the change of deflection angle for DNA larger than 6 kbp is relatively small, with only about 3 degree increase from 6 kbp to 20 kbp, while the smaller sized DNA (2, 4, 6 kbp) is well separated. However, with the 320 nm particles, DNA molecules of 2 and 4 kbp are not resolved, while the

larger ones have different deflection angles. In the pore size combination of 320 and 100 nm particles, changes in the angle  $\theta$  (measured as the net deflection effect of the whole separation chamber) were evenly distributed, and better overall separation was attained.

To widen the size range of separation tested, 48 kbp DNA was added, and experiments were performed in beds of 700/320 nm particles because larger pores are better for larger size DNA molecules. According to Figure 2.6, 6 and 10 kbp DNA can be separated in a combination of pore sizes and the resolution is better. The 20 and 48 kbp DNA fragments can be

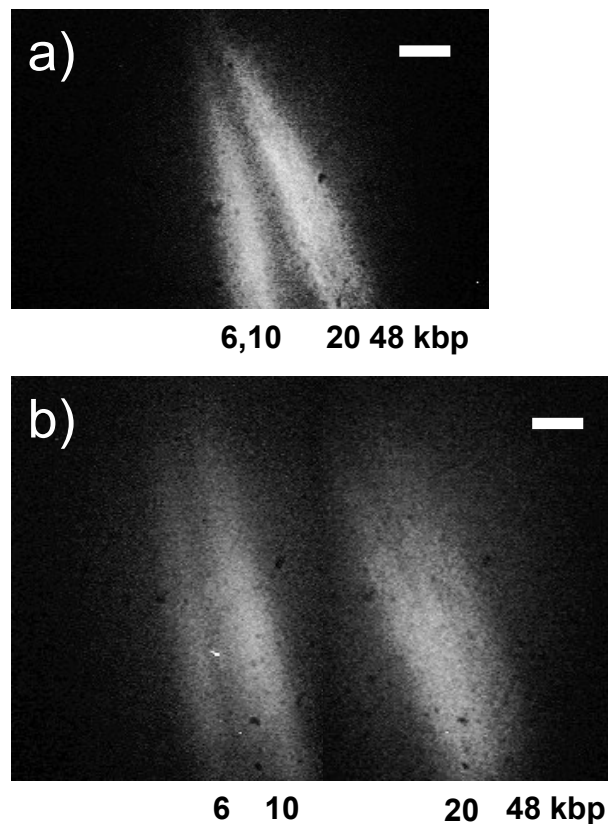


**Figure 2.6.** DNA separation inside 700/320 nm particles at  $E_1 = 280\text{V/cm}$ ,  $f = 15\text{Hz}$ . a) in the 700 nm region before the boundary, b) in the 320 nm region after the boundary.

resolved from the other sizes but the resolution is not very good. This may be due to the formation of hooking and of hernias inside the separation matrix, since the DNA is relatively large and the field is strong.

## 2.4 Conclusions

Gradients in pore size can be created in a size regime as small as 15 to 105 nm pores, much smaller than could be readily accomplished using nanolithography of pillars and posts. By packing separation zones with differing pore sizes, optimal separation could be achieved for each DNA size range by taking advantages from both larger and smaller pore sizes within one device, and the separation accomplished by upstream region can then be retained, as DNA moves across the zone boundary even when they have the same deflection angle in the downstream region. The peak capacity hence can be improved due to the employment of pore gradient. Thus, in addition to electric field, frequency and pore size, gradients or steps can be tuned to increase the peak capacity in the separation of DNA mixtures with a wide size distribution, avoiding the band broadening of a random pore size array.

## 2.5 References

1. Schwartz, D.C. and C.R. Cantor, *Separation of yeast chromosome-sized DNAs by pulsed field gradient gel-electrophoresis*. Cell, 1984. **37**(1): p. 67-75.
2. Carle, G.F. and M.V. Olson, *Separation of chromosomal DNA-*

- molecules from yeast by orthogonal-field-alternation gel-electrophoresis*. Nucleic Acids Research, 1984. **12**(14): p. 5647-5664.
3. Viovy, J.L., *Electrophoresis of DNA and other polyelectrolytes: Physical mechanisms*. Reviews of Modern Physics, 2000. **72**(3): p. 813-872.
  4. Huang, L.R., et al., *A DNA prism for high-speed continuous fractionation of large DNA molecules*. Nature Biotechnology, 2002. **20**(10): p. 1048-1051.
  5. Huang, L.R., et al., *Role of molecular size in ratchet fractionation*. Physical Review Letters, 2002. **89**(17).
  6. Zeng, Y., M. He, and D.J. Harrison, *Microfluidic self-patterning of large-scale crystalline nanoarrays for high-throughput continuous DNA fractionation*. Angewandte Chemie-International Edition, 2008. **47**(34): p. 6388-6391.
  7. Nazemifard, N., et al., *DNA dynamics in nanoscale confinement under asymmetric pulsed field electrophoresis*. Angewandte Chemie-International Edition, 2010. **49**(19): p. 3326-3329.
  8. Neiman, B., et al., *Organically modified silica sol-mediated capillary electrophoresis*. Analytical Chemistry, 2002. **74**(14): p. 3484-3491.
  9. Huang, L.R., et al., *Continuous particle separation through deterministic lateral displacement*. Science, 2004. **304**(5673): p. 987-990.
  10. Nazemifard, N., et al., *A systematic evaluation of the role of crystalline order in nanoporous materials on DNA separation*. Lab on a Chip, 2012. **12**(1): p. 146-152.
  11. Dufresne, E.R., et al., *Flow and fracture in drying nanoparticle suspensions*. Physical Review Letters, 2003. **91**(22).

# Chapter 3

## The Effect of Disorder on DNA Pulsed Field Electrophoresis<sup>\*</sup>

---

### 3.1 Introduction

The separation of DNA molecules by size is essential in molecular biology. Pulsed field gel electrophoresis (PFGE) has been the conventional method of separating long DNA molecules ( $\geq 10$  kbp) [1-3], in which electric field is switched between two directions with an obtuse angle. Negatively charged DNA molecules would move along the direction of the electric field, once the directions of the field change, the molecules reorient themselves to the new direction. The separation mechanism in PFGE is based on the head/tail switching (reorientation) of DNA molecules [4, 5]. Larger molecules have longer reorientation time compared to the smaller molecules [6]. PFGE is performed in a gel usually made of Agarose or polyacrylamide, usually highly random architectures with a wide distribution of pore sizes [7, 8].

---

<sup>\*</sup> A version of this chapter has been published: Nazemifard N. et al., 2012. Lab on a Chip, 12: 146-152. The work was done in collaboration with co-authors, Neda Nazemifard and Ledi Wang. My role includes device fabrication, electrophoresis experiments, and data analysis. A version of the submitted manuscript appears in their thesis as well.

With recent advances in microfluidic devices, there has been considerable interest in performing pulsed field electrophoresis in microchips that can be integrated in lab-on-a-chip devices. In most of these microfluidic separation devices, the random geometry of the gel has been replaced by a highly ordered microarray of pillars, with well controlled pore sizes. The microfabricated array structure for DNA separation was pioneered by Austin [9] who employed soft lithography technique to fabricate microarrays in silicon. Subsequently, Viovy [10] developed microarrays comprising self-assembled columns of magnetic beads formed upon imposition of magnetic field. These microfabricated array structures are highly ordered and the distance between the posts can be tuned for separating different sizes of DNA molecules.

To improve the separation resolution of DNA molecules in either conventional (gel-based) or microfluidic (microarray) devices, the experimental parameters should be optimized to provide the maximum peak-distance and minimum band-broadening between individual DNA bands. Although, there have been several studies on the effects of experimental parameters such as pulse frequency [11, 12], electric field strength [13], and buffer properties (such as pH, concentration, etc.) [14, 15] on DNA separation resolution, the effect of disorder of the separation matrix is somewhat less understood. This can be attributed to the practical difficulty of fabricating separation matrices with different degrees of

disorder. Several researchers developed numerical simulations to study the effects of disorder on DNA electrophoresis [16, 17]. However, their computational studies were focused on one-dimensional steady-state DNA electrophoresis in sparse arrays of obstacles where the spacing between the obstacles ( $\sim 1-4 \mu\text{m}$ ) was orders of magnitude larger than the persistence length of DNA ( $\sim 50 \text{ nm}$ ). The separation of DNA in a sparse post array is based on the collision frequency of the DNA molecules with the obstacles [18, 19]. The higher collision frequency results in higher separation resolution, so that the separation mechanism is different from the head and tail switching, or ratchet mechanism in pulsed field electrophoresis. This indicates that the effect of disorder on DNA pulsed electrophoresis might be different from DNA electrophoresis in a sparse array.

In the microchip designed and developed in our group for DNA separation, self-assembled nanoparticle arrays were used as the sieving matrices under pulsed field electrophoresis.(Figure 3.1a)[20, 21] An evaporation induced self-assembly technique was employed to form hexagonal close packed nanoparticles as shown in Figure 3.1b and c. Asymmetric pulsed electric fields were applied to achieve 2D separation of DNA molecules (Figure 3.2a-c). One of the advantages of using the self-assembly approach is that it provides an opportunity to systematically study the effect of disorder on DNA separation resolution and band broadening. Using the self-assembly approach and monodisperse particle suspensions,

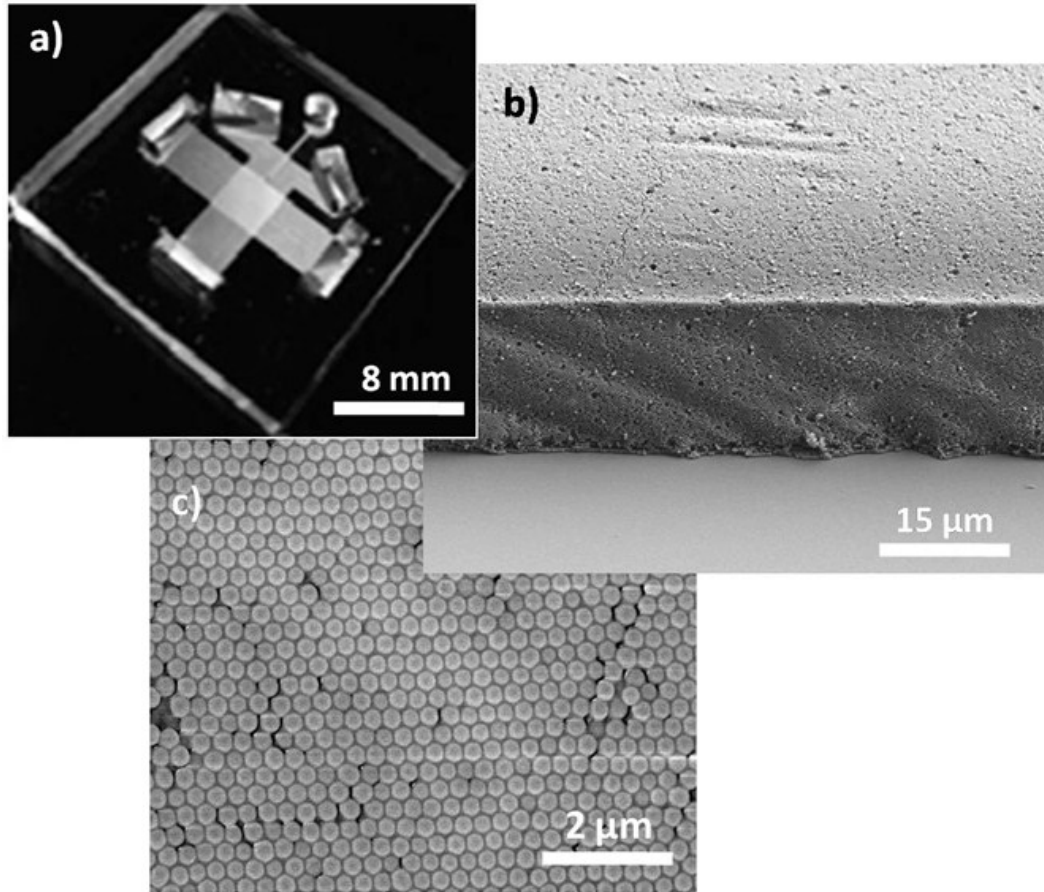


**Figure 3.1.** (a) PDMS microchip for DNA separation. The microchip contains an injection channel which is connected to the separation chamber (the square part in the middle of the microchip) where the separation of DNA molecules occurs. The chamber is connected to different buffer reservoirs in order to apply the electric field (b) SEM image of self-assembled 320 nm silica particles inside the separation chamber. (c) SEM image of the top surface of (b) which shows a uniform hexagonal packed structure.

uniform, ordered structures are fabricated (the structure shown in Figure 3.1c for instance), which resemble the ordered extreme of microfabricated arrays. Bidisperse particle suspensions, on the other hand, are used to fabricate random structures which resemble the disordered structure of gels.

By changing the ratio of the particle concentrations in a bidispersed solution, structures with different degrees of disorder can be fabricated. Using this scheme, in addition to highly ordered, defect-free structures, random structures are formed where defects would be intentionally introduced to the separation matrix by adding the second particle to the suspension and the degree of disorder can be systematically increased by increasing the concentration of the second particle. In the following sections, a brief description of the experimental set up and the self-assembly technique is first presented. Next, different parameters used to characterize the degree of disorder in the packed nanoparticle structures are described. Finally, the results of DNA separations conducted in structures with different degrees of disorder are presented and discussed.

## **3.2 Experimental Section**

### **3.2.1 DNA Separation**

DNA separations were conducted using a microfluidic chip filled with an array of nanoparticles as a sieving matrix. A schematic of the PDMS microchip is shown in Figure 3.2a. PDMS microchips were fabricated using a standard soft lithography technique, then sealed onto clean glass slides prior to packing, as described in detail elsewhere [21]. Aqueous suspensions of silica colloids (Bangs Laboratories, Fishers, IN) of

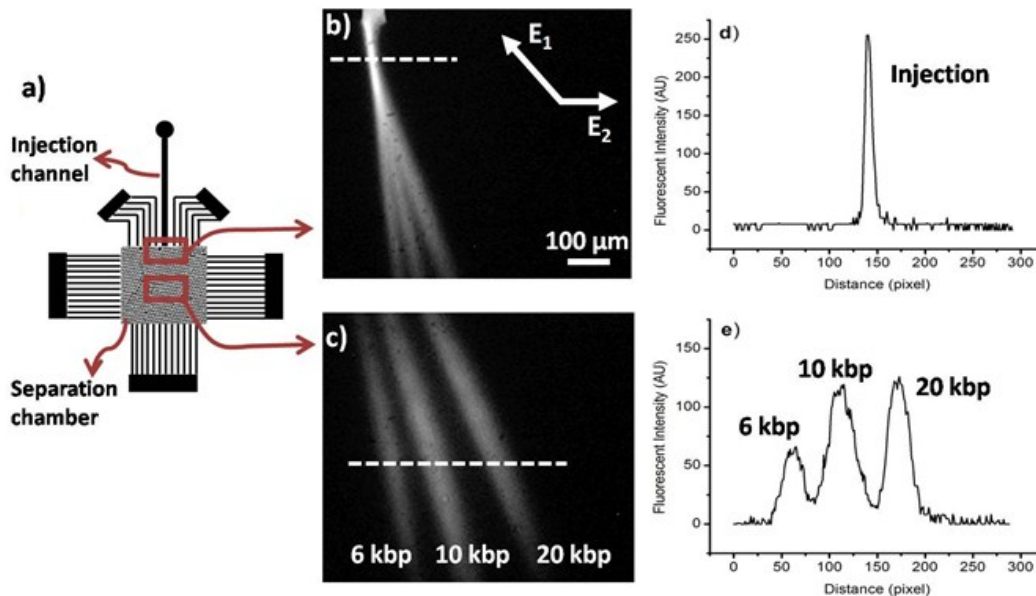


**Figure 3.2.** a) Schematic of the DNA separation microchip. b) Fluorescent image of the junction of the separation chamber and injection channel. A mixture of three different sizes of DNA: 6, 10, and 20 kbp is injected into the separation chamber. c) Fluorescent image of the separated DNA molecules in the middle of the separation chamber. d) and e) fluorescent intensity profiles at the injection and the middle of the separation chamber along the dashed lines in b) and c), respectively.

330 nm, and 700 nm diameter were used to form the self-assembled nanoparticle array inside the microchips using the procedure discussed in Section 2.2.1. DNA fragments (6, 10, 20 kbp, Fermentas Life Sciences) were stained by YOYO-1 (Molecular Probes) with a dye-to-base ratio of 1:10. Pulsed field electrophoresis was performed in 4× TBE buffer to suppress the electroosmotic flow with 4% v/v 2-mercaptoethanol added to reduce photobleaching. Pulsed electric fields were generated using homebuilt high-voltage amplifiers triggered by square wave signals from a

synthesized function generator. DNA samples were excited by a 488-nm argon ion laser beam, and the fluorescent emission was collected by a homemade microscope using a 4× objective (0.1 N.A., Olympus). Digitized images were analyzed using ImageJ (NIH, <http://rsb.info.nih.gov/ij/>).

Separation of DNA molecules was conducted by injecting DNA samples into the separation chamber inside the microchip. The fluorescence image shown in Figure 3.2b represents the junction of the injection channel and separation chamber. The separation chamber was connected to reservoirs where pulsed electric potentials were applied using platinum electrodes. The applied pulsed electric potentials generate asymmetric obtuse-angle pulsed fields,  $E_1$  and  $E_2$  across the separation chamber, where the angle between the pulsed fields is  $\sim 135^\circ$  and  $E_1 = 1.4E_2$  (as shown in Figure 3.2b) in all our experiments. Once a DNA sample reaches the separation chamber, different sizes of DNA molecules separate from each other and form individual streams, as shown in Figure 2c. The separation mechanism of DNA molecules under obtuse-angle pulsed fields is as follows: pulsed electric field causes DNA molecules to stretch and reorient periodically, with their head/tail repeatedly switched. Due to this periodic head/tail switching of the molecule, the net migration of DNA molecules is biased in different directions by the asymmetric fields; larger molecules are deflected farther from the injection angle more compared to smaller ones.

### 3.2.2 Self-assembled Nanoparticle Array Structures

Monodispersed suspensions of silica particles of 320 nm and 700 nm were used to fabricate ordered packed structures inside the separation chamber in the microfluidic device. SEM images of these structures revealed homogenous, ordered packed structures where the pore size is around 15% of the particle size, which is the radius of narrowest tunnel surrounded by three adjacent spherical particles.

### 3.3 Results and Discussion

In order to introduce defects and disrupt the regular crystalline geometry of these homogenous packed structures, bidispersed suspensions of 320 nm and 700 nm silica beads with different volume fractions of 700 nm particles ( $\chi_{700}$ ) were used to fabricate the packed structures with different degrees of defects. This means that  $\chi_{700} = 0$  and  $\chi_{700} = 1$  represent the ordered structures whereas  $0 < \chi_{700} < 1$  represent the disordered structures. It is worth mentioning here that these two particle sizes were used in our experiment based on the insignificant difference between the porosity of the monodispersed and bidispersed structures of these two particles. According to several studies in literature [22-24], the porosity of the binary packed structures of two particles with size ratio around 0.45 ( $320/700 = 0.45$ ) has a maximum 10% difference compared to the porosity

of the monodispersed packed structures of either particles. This implies that the addition of the second particle to the packed structure of the primary particle would just increase the degree of disorder without changing the porosity significantly.

### **3.3.1 Characterization of the Packed Structures.**

To characterize the different colloidal structures with different  $\chi_{700}$ , SEM images of these structures were obtained. Figure 3.3a, panels II to V, show SEM images of colloidal crystal structures with different  $\chi_{700}$  ranging from 0 (ordered structure of 320 nm particles) to 0.5 (320 nm and 700 nm particles were mixed with the same volume ratio). The image in Panel I is a computationally generated image of an ideal hexagonal packed spheres. This image was used as a reference with the highest degree of order. Using image analysis techniques, the center of the particles were located.

Several approaches were taken to quantitatively analyze the degree of order from particle center coordinates. Traditionally, colloidal order in two-dimensional images can be evaluated by the radial distribution function,  $g(r)$ , where the number and magnitude of the peaks in the plot of  $g(r)$  with respect to scaled distance represent the degree of order in the structures [25-27]. Figure 3.3b shows plots of  $g(r)$  calculated for each corresponding SEM image. A comparison between these images shows that the experimentally created packed structure of 320 nm particles (Panel II) is

very similar to the ideal hexagonal packed structure. We also note that by increasing  $\chi_{700}$  (Panels III to V) the degree of disorder in the structures would increase.

Another single parameter useful for characterizing two-dimensional

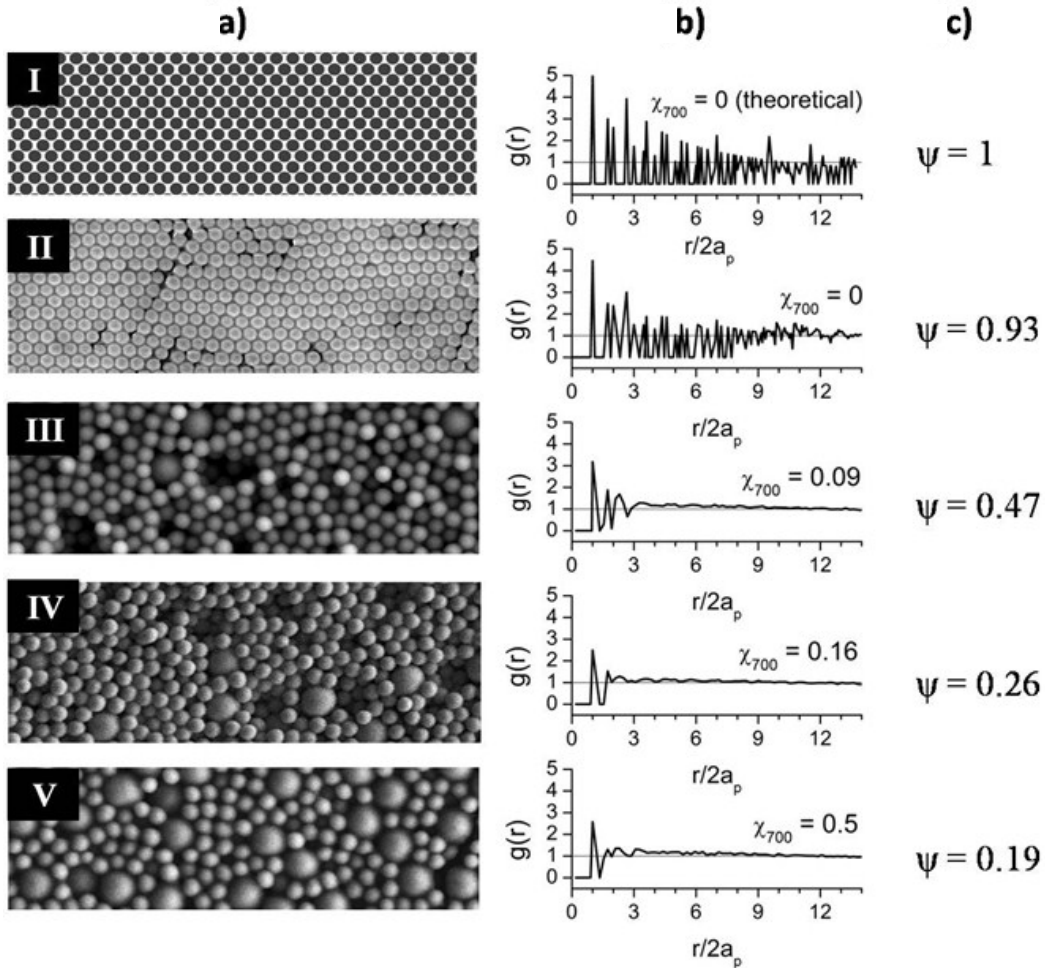


**Figure 3.3.** a) SEM images of the self-assembled packed structures of 320 and 700 nm silica particles with different  $\chi_{700}$  from the top:  $\chi_{700} = 0, 0.09, 0.16,$  and  $0.5$ . The first top image is the ideal hexagonal lattice of spheres generated by the image analysis software. b) Radial distribution function calculated for each structure shown in a).  $a_p$  is the particle radius. c) Global orientational order parameter calculated for each structure shown in a).

order is a global bond orientational order parameter given as

$$\psi = \frac{1}{N_p} \left| \sum (\cos 6\omega + i \sin 6\omega) \right| \quad (3.1)$$

where  $i$  is the imaginary unit,  $\omega$  is the angle between a line joining nearest neighbors and an arbitrary reference axis, and  $N_p$  is the total number of particles.  $\psi$  approaches unity for perfect hexagonal order and approaches zero for random configurations[26, 28]. Using SEM images taken at 5~10 different locations of each CSA packing, the global  $\psi$  was an average of at least 30 center particles for each structure. As shown in Figure 3c, it can be seen from this figure that by increasing the concentration of the 700 nm particles, the hexagonal order in the packed structure of 320 nm is

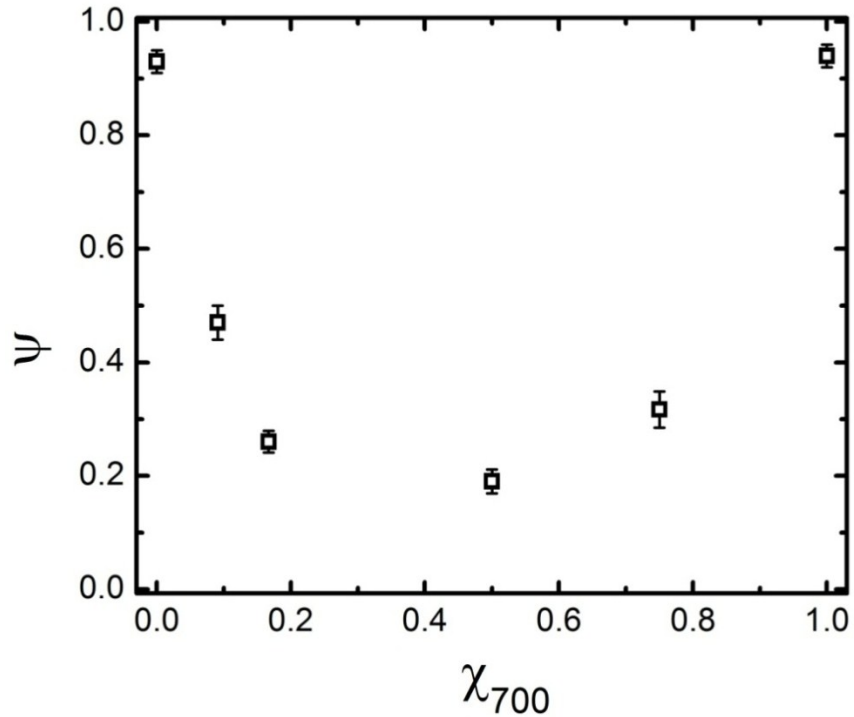


**Figure 3.4.** Variation of global orientational order parameter,  $\psi$ , with respect to  $\chi_{700}$ .

increasingly distorted. The similar values of  $\psi$  for the images in Panel I and II show that the self-assembled array of 320 nm particles is very similar to the perfect hexagonal packed structure. Figure 3.4 shows the variation of  $\psi$  with respect to  $\chi_{700}$ . As expected,  $\chi_{700} = 0$  and  $\chi_{700} = 1$  have the highest degree of order. The addition of the second particle to the packed structure of the primary particle would distort the hexagonal order, where  $\chi_{700} = 0.5$  represents the packed structure with the highest degree of disorder.

An important difference between mono and binary packed structures is their pore size distribution. In mono packed structures, the pore size distribution is very sharp while in binary packed structures, there is a broad

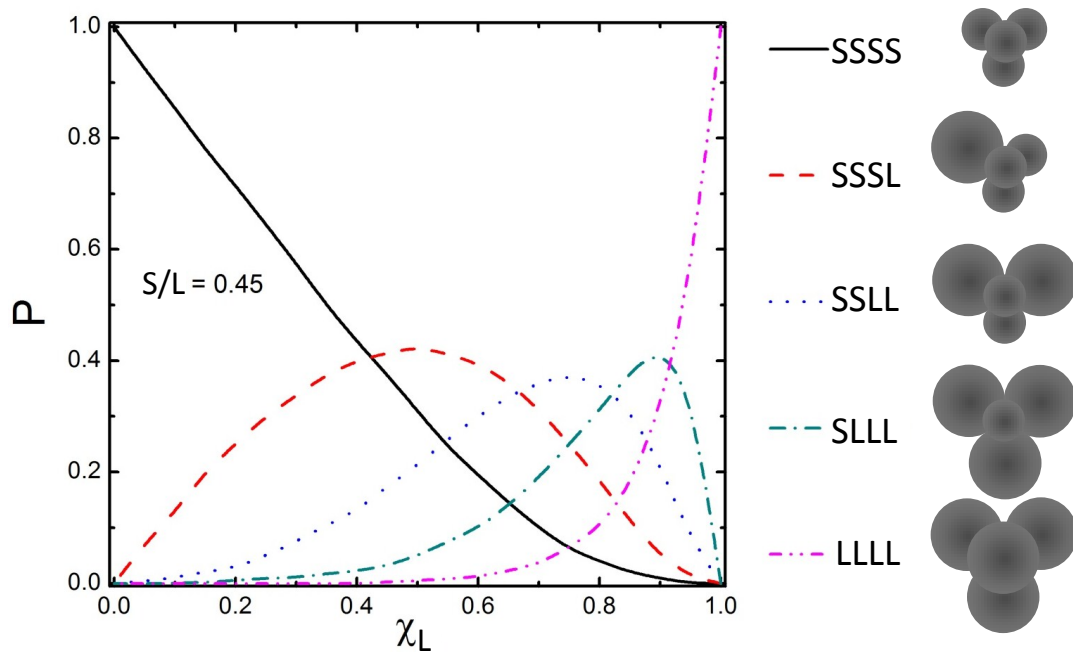


**Figure 3.5.** Probability of the presence of five different pore sizes as a function of the volume fraction of the larger particle,  $\chi_L$ , in the binary packing of spheres with size ratio of 0.45.

broad pore size distribution, which is strongly dependent on the size ratio of the two particles. Assuming that each pore is formed by four adjacent particles, there are five different possibilities for pore formation in a binary packed structure of small (s) and large (L) particles: SSSS, SSSL, SLLS, SLLL, and LLLL. Figure 3.5 taken from Andrade [29] shows the pore size frequency distribution,  $P$ , as a function of volume fraction of larger particle ( $\chi_L$ ) for the particle size ratio around 0.45. It can be seen from Figure 3.5 that while for mono packed structures, there is only one pore size present, in binary packed structures, at certain volume fractions ( $\chi_L = 0.75$ ), there can be up to five different pore sizes present in the structure.

### 3.3.2 DNA Separation

In order to study the effect of disorder on DNA separation resolution, DNA separations were conducted in self-assembled packed structures with  $\chi_{700}$  varying from zero to unity. For each experiment, fluorescence intensity profiles were acquired both at the injection point, as well as, at a certain distance from the injection channel as shown in Figure 3.2d and e. Using the fluorescence intensity profiles, the peak positions and peak variances were calculated. Peak distance between two consecutive DNA streams was calculated by subtracting their corresponding peak positions. Figure 3.6 shows the variation of the peak distance with respect

to  $\chi_{700}$  between DNA sizes: 6-10 kbp and 10-20 kbp at a)  $E_1 = 160$  V/cm,  $f = 15$  Hz and b)  $E_1 = 280$  V/cm,  $f = 20$  Hz. The frequencies for each electric field were adjusted to maximize the separation. For each data point in this figure, three microchips were fabricated and packed with particle suspensions with the same  $\chi_{700}$ . DNA separations were conducted in these microchips and peak distances were calculated as described earlier. Using these results, the average and error bars of one standard deviation were calculated for each  $\chi_{700}$  as shown in Figure 3.6. The two sides in this figure correspond to ordered structures ( $\chi_{700} = 0$  and  $\chi_{700} = 1$ ) whereas the inner parts represent structures with different degrees of disorder.

According to Figure 3.6, by increasing the degree of disorder, the peak distances between the three DNA sizes decrease (except a small increase at  $\chi_{700} = 0.09$  compared to  $\chi_{700} = 0$ ). This effect is more pronounced at higher electric field between all three DNA sizes. The minimum peak distance was measured at  $\chi_{700} = 0.75$  for both cases. According to Figure 3.5, in a binary packed structure of 320 nm and 700 nm particles,  $\chi_{700} = 0.75$  has the most variety of pore size, meaning all five different pore sizes are present at this structure [29].

The decline of peak distance in disordered structures can be explained based on the separation mechanism of long DNA molecules

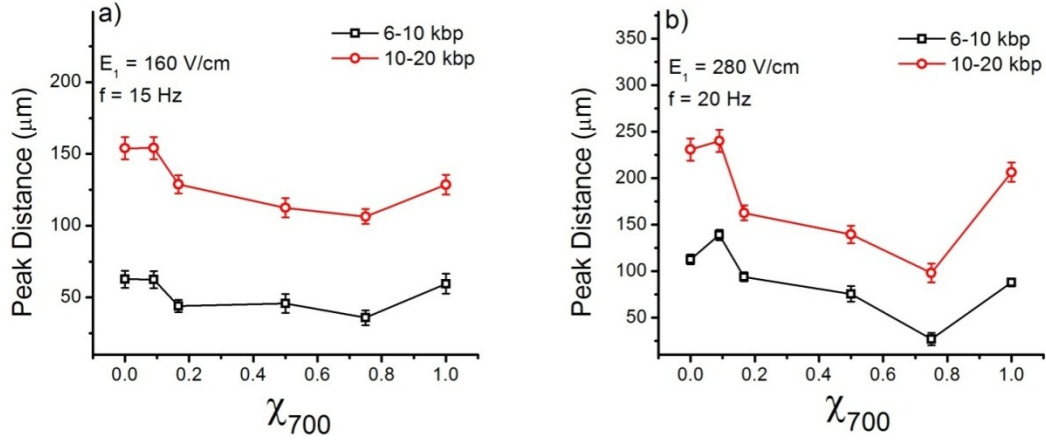


**Figure 3.6.** Variation of peak distance between 6-10 kbp and 10-20 kbp DNA molecules with respect to  $\chi_{700}$  for (a)  $E_1 = 160 \text{ V/cm}$ ,  $f = 15 \text{ Hz}$  and (b)  $E_1 = 280 \text{ V/cm}$ ,  $f = 20 \text{ Hz}$ .

under pulsed field electrophoresis (Section 1.3.2.5). As described earlier, the separation of different molecules is caused by the backtracking motion of the molecules under the pulsed electric field. When DNA molecules are subjected to an electric field, they stretch and move in the direction of the applied electric field. When the direction of the electric field changes with an obtuse angle, the molecules backtrack to the new direction of the electric field, with the head that used to be the tail in the previous half cycle. Due to this backtracking motion, the overall distance that the molecule migrates in each cycle becomes strongly dependent on the DNA size ( $N$ ). This distance varies linearly with DNA size ( $\sim N$ ) in ordered structures such as microfabricated arrays [6, 30]. In disordered structures such as gels, the DNA dynamics is more complicated. The higher collision frequency of DNA molecules with the structure in disordered matrices results in

complicated conformations of DNA, so that the distance traveled by the molecules will no longer be a linear function of DNA size [6].

Although the separation resolution is directly proportional to the peak distance between DNA bands, another major contributor to separation resolution is band broadening. Here, band width is defined as  $Wb = 4\sigma$ , where  $\sigma$  is the peak standard deviation of the fluorescence intensity profile. The peak variance for each DNA stream was calculated at a certain distance from the injection channel where the field is considered uniform. The total (observed) variance is the summation of the variances introduced by different independent factors [31]. The variance due to injection ( $\sigma_{inj}$ ) can be calculated using the fluorescence intensity profiles at the injection channel (Figure 3.2d), allowing estimation of the variance due to other contributions ( $\sigma_{other}$ ):

$$\sigma_{total}^2 = \sigma_{inj}^2 + \sigma_{other}^2 \quad (3.2)$$

$$\sigma_{other} = \sqrt{\sigma_{total}^2 - \sigma_{inj}^2} \quad (3.3)$$

$\sigma_{other}$  is the band broadening due to DNA size fluctuations, Brownian diffusion, electric field gradients, and other components.

To study the effect of disorder on band broadening,  $\sigma_{other}$  was calculated for each stream of DNA in structures with  $\chi_{700}$  varying from zero to unity. The results are shown in Figure 3.7. This figure shows the

variation of  $\sigma_{\text{other}}$  with respect to  $\chi_{700}$  for three different DNA sizes: 6, 10, and 20 kbp at a)  $E_l = 160$  V/cm,  $f = 15$  Hz and b)  $E_l = 280$  V/cm,  $f = 20$  Hz. According to Figure 3.7, the band broadening is highest for  $\chi_{700} = 0.5$ , which represents a structure with the maximum degree of disorder according to Figure 3.4. Local minima, with similar values of band broadening are seen for  $\chi_{700} = 0.25$  and  $\chi_{700} = 0.75$  (which have different pore size distributions). Surprisingly, band broadening increases again for maximum ordered states,  $\chi_{700} = 0$  and 1. The results show that band broadening is affected to a greater extent by the distortion in hexagonal structure rather than the presence of different pore sizes in binary packed structures.

The non-monotonic behavior of band broadening we observe with respect to degree of disorder in the matrix is not totally understood. It was

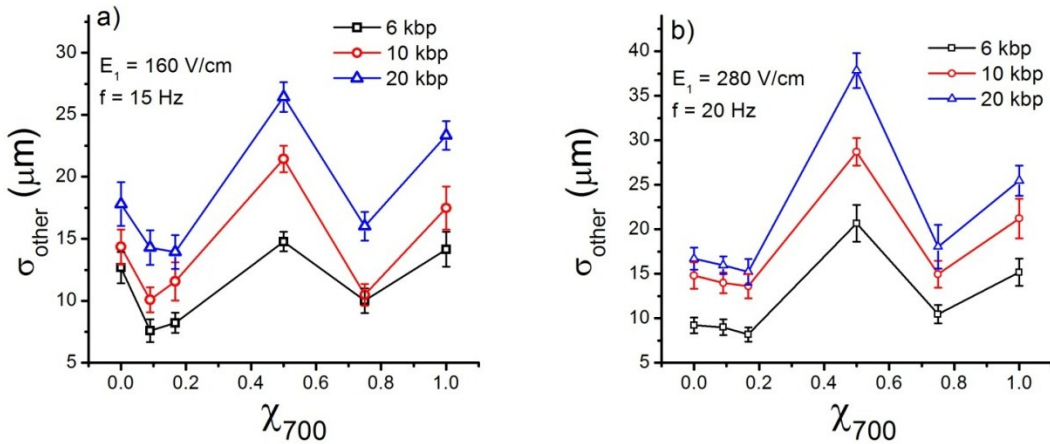


**Figure 3.7.** Variation of band broadening,  $\sigma_{\text{other}}$  calculated using Eq. 1b, for 6, 10, and 20 kbp DNA molecules with respect to  $\chi_{700}$  for (a)  $E_l = 160$  V/cm,  $f = 15$  Hz and (b)  $E_l = 280$  V/cm,  $f = 20$  Hz.

predicted by Monte Carlo simulation [32] that DNA diffusion coefficients in an array of obstacles show non-monotonic behavior. Slater et al. [32] suggested that increasing order favored reptation, while decreasing order favored entropic trapping, and that these two models of molecular behavior exhibited diffusion coefficients with opposite dependence on order. In electromigration of DNA, diffusion is a minor contributor to band broadening, whereas other molecular dynamics play a larger role [33-36]. By analogy, increasing order will increase reptation like motion and decrease hooking, entanglement, hernia formation, and entropic trapping while decreasing order will increase the latter effects. The net effect will create a competition between band broadening that could also lead to non-monotonic behavior.

Once the peak distance and band broadening are measured, the

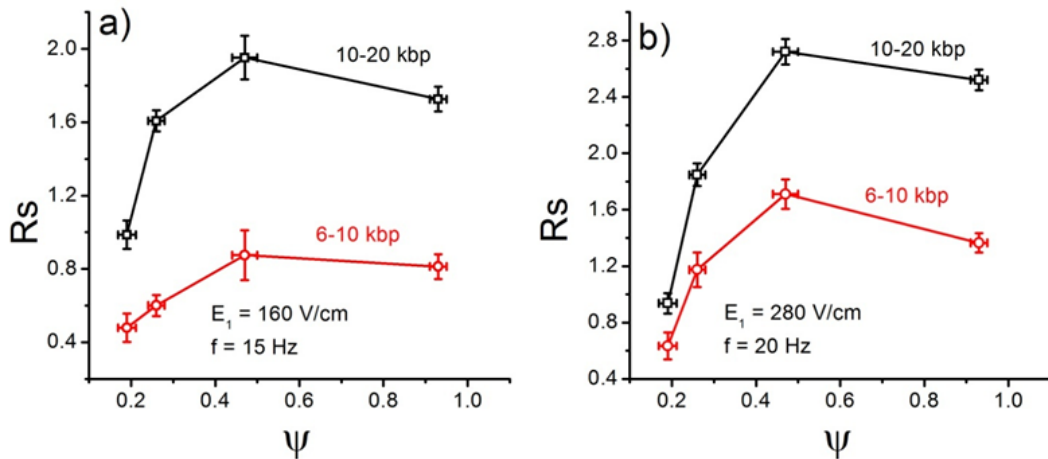


**Figure 3.8.** Variation of separation resolution,  $R_s$ , calculated using Equation 3.2, between 6-10 kbp and 10-20 kbp DNA molecules with respect to  $\psi$  for (a)  $E_1 = 160$  V/cm,  $f = 15$  Hz and (b)  $E_1 = 280$  V/cm,  $f = 20$  Hz.

separation resolution between different sizes of DNA molecules can be calculated. Resolution is employed to evaluate the separation performance, and is defined as the quotient of the peak distance over the average band broadening for two consecutive DNA bands:

$$Rs_{6-10} = \frac{PD_{6-10}}{\frac{1}{2}(Wb_6 + Wb_{10})} = \frac{PD_{6-10}}{2(\sigma_6 + \sigma_{10})} \quad (3.4)$$

where  $Rs_{6-10}$  is the separation resolution between 6 and 10 kbp DNA,  $PD_{6-10}$  is the peak distance between the two DNA sizes,  $Wb_6$ ,  $Wb_{10}$  and  $\sigma_6$ ,  $\sigma_{10}$  are baseline bandwidths and standard deviations for 6 and 10 kbp DNA, respectively. Two peaks with resolution larger than 1.5 is considered as baseline resolved. Using this equation, the separation resolution was calculated between three DNA sizes in structures with  $\chi_{700}$  varying between zero to unity. The resolution,  $Rs$ , is shown in Figure 3.8 as a function of the degree of order,  $\psi$ , for  $\chi_{700} = 0$  to 0.5. Figure 3.8 shows the separation resolution increases significantly as the order increases. On the other hand, comparing  $\psi = 0.47$  and  $\psi = 0.93$  shows that small scale, scattered defects or disorder have either no significantly negative or sometimes even positive effects on separation resolution, as long as the local order in the structure is preserved. Once the degree of disorder is increased such that the local order of the structure is affected, the separation resolution decreases significantly.

The injection band broadening width contributes significantly to the

observed resolution in Figure 3.8. Using Equation 3.3 to isolate  $\sigma_{\text{bed}}^2$ , then substituting these corrected values into Equation 3.4 allows evaluation of the resolution arising solely from the separation bed. Figure 3.9 shows the variation of the scaled “bed resolution”,  $Rs_{\text{bed}}^* = Rs_{\text{bed}}/Rs_{\text{bed}, \chi_{700}=0}$ , with respect to  $\chi_{700}$ , illustrating the variation of separation resolution with the degree of disorder is more pronounced for larger electric fields and longer DNA molecules. For a field of 280 V/cm, the separation resolution between 10 and 20 kbp DNA molecules in a structure with  $\chi_{700} = 0.5$  drops to around one third of the resolution in ordered structures with  $\chi_{700} = 0$ . This is particularly important, since most of the new DNA separation devices perform in strong electric fields to accelerate the separation process.

It can be seen from Figure 3.9 that except for a small initial increase, overall, by increasing the degree of disorder in the structure, the separation resolution decreases between all three different DNA sizes. A comparison between the resolution for ordered ( $\chi_{700} = 0$  and 1) and highly disordered ( $\chi_{700} = 0.5$ ) arrays shows that regardless of the pore size ( $\sim 50$  nm for  $\chi_{700} = 0$  and 105 nm for  $\chi_{700} = 1$ ), the resolution in ordered structures is higher compared to disordered structures. The change in resolution is not symmetric around  $\chi_{700} = 0.5$ . This may be caused by the asymmetric pore size distribution around  $\chi_{700} = 0.5$ . Between  $\chi_{700} = 0$  to 0.5, pore sizes introduced to the structure are all larger than the initial pore size (SSSS  $\sim 50$  nm). Between  $\chi_{700} = 1$  to 0.5, the pore sizes introduced to the structure

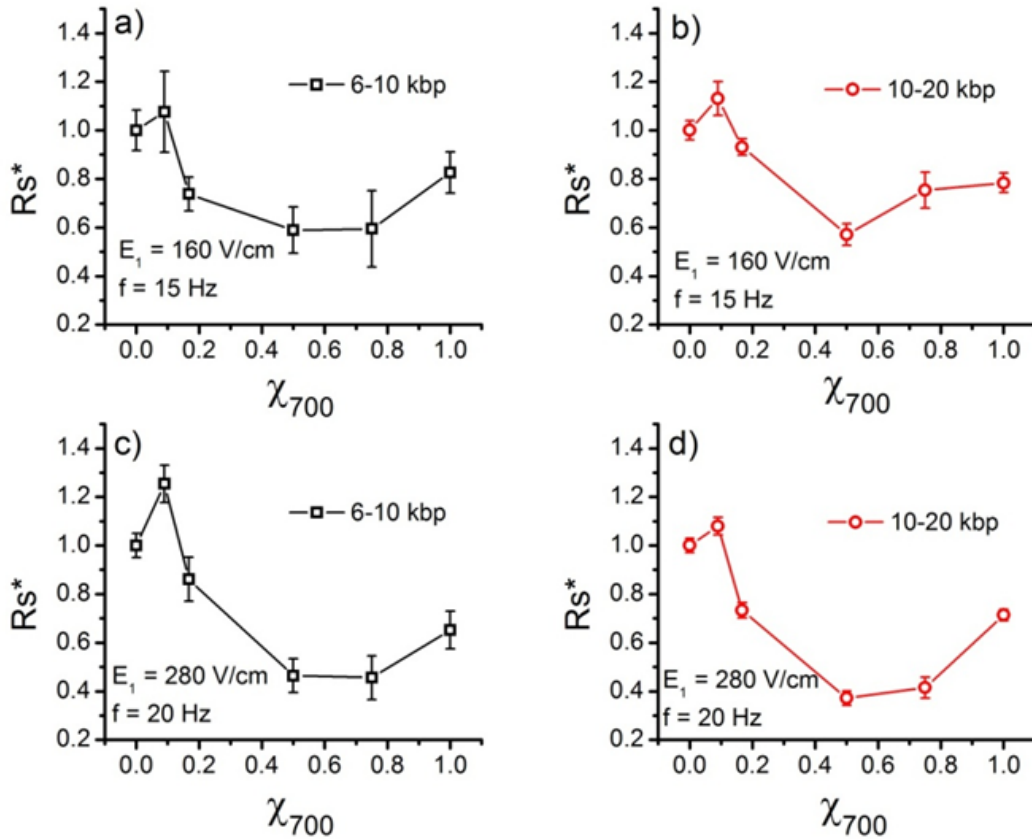


**Figure 3.9.** Variation of scaled and bed corrected resolution  $R_s^* = R_s/R_{s\chi_{700}=0}$ , with respect to  $\chi_{700}$ . ( $R_{s\chi_{700}}$  for a)  $0.81_3 \pm 0.06_8$  b)  $1.72_6 \pm 0.06_8$  c)  $1.36_5 \pm 0.06_8$  d)  $2.52_0 \pm 0.07_3$

are all smaller than the initial pore size (LLLL  $\sim 105$  nm). As stated in the literature [1] as well as shown in Figure 3.9, separation resolution decreases by increasing the pore size. By changing the structure from  $\chi_{700} = 0$  to  $\chi_{700} = 0.5$ , both the greater disorder and greater pore sizes could contribute to decreasing the separation resolution. On doping the structure from  $\chi_{700} = 1$  to  $\chi_{700} = 0.5$ , the pore sizes decrease while the order decreases too. Moreover, resolution is higher at  $\chi_{700} = 1$  compared to  $\chi_{700} = 0.5$ . These observations show that the effect of order must dominate, since the

resolution decreases with increasing disorder, overcoming the effect of decreasing pore size on separation resolution.

### **3.4 Conclusions**

In this work, the effect of matrix disorder on the separation of long DNA molecules under pulsed electric fields is studied. The behavior of both peak distance and band broadening are investigated in structures with varying degrees of disorder. Mono and binary self-assembled colloidal crystals are used to create highly ordered as well as disordered matrices for DNA separations. Various quantitative parameters are employed to measure the degree of disorder in the binary packed structures. It is shown that by introducing the second particle to the hexagonally packed structure of the primary particle, two major changes occur: i) the hexagonal lattice arrangement of the primary particles diminishes with increasing the concentration of the second particles, and ii) different pore sizes would appear in the structure which initially posed just a single pore size.

To evaluate the separation performance of such artificially induced pore size heterogeneity, DNA separations were conducted in each structure and fluorescent intensity profiles were obtained for each DNA band. Using image analysis techniques, the peak distance and band broadening were calculated for each DNA band and used to calculate the separation resolution between different sizes of DNA molecules. Our results show that

peak distance between the DNA molecules decreases by increasing the degree of disorder in the separation matrix. The corresponding band broadening with degree of disorder is more complicated and is a non-monotonic function of the degree of disorder in separation matrix.

Compared to ordered structures, separation resolution is significantly lower in structures with long range disorder. It is also shown that as long as the local order is preserved, the presence of small scale disorder or scattered defects might even improve the separation resolution.

The effect of disorder on DNA separation resolution was studied numerically for one-dimensional DNA electrophoresis in sparse arrays [16, 17]. In those studies, it was concluded that although the short term order might increase the resolution, disorder is necessary to increase the collision frequency of the DNA with obstacles and, in turn, to increase the separation resolution. A comparison between those results and our study shows that although local order improves resolution, the effect of long range disorder on separation resolution is different between the two studies. This indicates that the influence of disorder on the separation resolution is dependent on the separation mechanism of a particular technique, and is not universal.

Our results show that the decline of separation resolution in highly disordered structures is more pronounced for longer DNA molecules and at higher electric fields. This is a significant result since the current trend in DNA separation technology is to accelerate the separation process of long

DNA molecules by increasing the electric fields. Our results show that by transitioning from a highly disordered structure to a structure with local order, the separation resolution can be improved up to three folds. This suggests that dynamics of DNA undergoing pulsed-field electrophoresis is more straightforward in the ordered structure than in highly disordered structures like gels. The motion in an ordered structure is more uniform with less trapping frequency and lower probability of hairpin formation leading to an increase in peak distance and improved resolution. To our knowledge, this work is the first systematic, experimental study on the effect of disorder of the separation medium on DNA separation resolution during pulsed field electrophoresis.

### 3.5 References

1. Viovy, J.L., *Electrophoresis of DNA and other polyelectrolytes: Physical mechanisms*. Reviews of Modern Physics, 2000. **72**(3): p. 813-872.
2. Schwartz, D.C. and C.R. Cantor, *Separation of yeast chromosome-sized DNAs by pulsed field gradient gel-electrophoresis*. Cell, 1984. **37**(1): p. 67-75.
3. Gunderson, K. and G. Chu, *Pulsed-field electrophoresis of megabase-sized DNA*. Molecular and Cellular Biology, 1991. **11**(6): p. 3348-3354.
4. Volkmuth, W.D. and R.H. Austin, *DNA electrophoresis in microlithographic arrays*. Nature, 1992. **358**(6387): p. 600-602.
5. Bustamante, C., S. Gurrieri, and S.B. Smith, *Towards a molecular description of pulsed-field gel-electrophoresis*. Trends in Biotechnology, 1993. **11**(1): p. 23-30.
6. Duke, T.A.J., et al., *Pulsed-field electrophoresis in microlithographic arrays*. Electrophoresis, 1996. **17**(6): p. 1075-1079.

7. Chui, M.M., R.J. Phillips, and M.J. McCarthy, *Measurement of the porous microstructure of hydrogels by nuclear-magnetic-resonance*. Journal of Colloid and Interface Science, 1995. **174**(2): p. 336-344.
8. Pernodet, N., M. Maaloum, and B. Tinland, *Pore Size of Agarose Gels By Atomic Force Microscopy*. Electrophoresis, 1997. **18**(1): p. 55-58.
9. Volkmuth, W.D., et al., *DNA electrodiffusion in a 2d array of posts*. physical review letters, 1994. **72**(13): p. 2117-2120.
10. Minc, N., et al., *Quantitative microfluidic separation of DNA in self-assembled magnetic matrixes*. Analytical Chemistry, 2004. **76**(13): p. 3770-3776.
11. Heller, C., C. Pakleza, and J.L. Viovy, *DNA separation with field-inversion capillary electrophoresis*. electrophoresis, 1995. **16**(8): p. 1423-1428.
12. Sudor, J. and M.V. Novotny, *Pulsed-field capillary electrophoresis - optimizing separation parameters with model mixtures of sulfonated polystyrenes*. Analytical Chemistry, 1994. **66**(13): p. 2139-2147.
13. Mathew, M.K., C.L. Smith, and C.R. Cantor, *High-resolution separation and accurate size determination in pulsed-field gel-electrophoresis of DNA .2. effect of pulse time and electric-field strength and implications for models of the separation process*. Biochemistry, 1988. **27**(26): p. 9210-9216.
14. Doggett, N.A., C.L. Smith, and C.R. Cantor, *The effect of DNA concentration on mobility in pulsed field gel-electrophoresis*. Nucleic Acids Research, 1992. **20**(4): p. 859-864.
15. White, H.W., *Rapid separation of DNA-molecules by agarose-gel electrophoresis - use of a new agarose matrix and a survey of running buffer effects*. Biotechniques, 1992. **12**(4): p. 574-579.
16. Patel, P.D. and E.S.G. Shaqfeh, *A computational study of DNA separations in sparse disordered and periodic arrays of posts*. Journal of Chemical Physics, 2003. **118**(6): p. 2941-2951.
17. Mohan, A. and P.S. Doyle, *Effect of disorder on DNA electrophoresis in a microfluidic array of obstacles*. Physical Review E, 2007. **76**(4).
18. Dorfman, K.D., *DNA electrophoresis in microfluidic post arrays under moderate electric fields (vol 73, art no 061922, 2006)*. Physical Review E, 2008. **77**(1).
19. Ou, J., et al., *DNA electrophoresis in a sparse ordered post array*. Physical Review E, 2009. **79**(6).
20. Zeng, Y. and D.J. Harrison, *Self-assembled colloidal arrays as three-dimensional nanofluidic sieves for separation of biomolecules on microchips*. Analytical Chemistry, 2007. **79**(6): p. 2289-2295.
21. Zeng, Y., M. He, and D.J. Harrison, *Microfluidic self-patterning of*

- large-scale crystalline nanoarrays for high-throughput continuous DNA fractionation.* Angewandte Chemie-International Edition, 2008. **47**(34): p. 6388-6391.
22. Dias, R.P., et al., *Particulate binary mixtures: Dependence of packing porosity on particle size ratio.* Industrial & Engineering Chemistry Research, 2004. **43**(24): p. 7912-7919.
  23. Dias, R., et al., *Tortuosity variation in a low density binary particulate bed.* Separation and Purification Technology, 2006. **51**(2): p. 180-184.
  24. Song, M., K.T. Chuang, and K. Nandakumar, *A theoretical correction of the Ouchiyama and Tanaka formula for predicting average porosity of packed beds consisting of nonuniform spheres.* Industrial & Engineering Chemistry Research, 1998. **37**(8): p. 3490-3496.
  25. Aste, T., *Variations around disordered close packing.* Journal of Physics-Condensed Matter, 2005. **17**(24): p. S2361-S2390.
  26. Bevan, M.A., et al., *Structural evolution of colloidal crystals with increasing ionic strength.* Langmuir, 2004. **20**(17): p. 7045-7052.
  27. Clarke, A.S. and H. Jonsson, *Structural-Changes Accompanying Densification of Random Hard-Sphere Packings.* Physical Review E, 1993. **47**(6): p. 3975-3984.
  28. Halperin, B.I. and D.R. Nelson, *Theory of 2-Dimensional Melting.* Physical Review Letters, 1978. **41**(2): p. 121-124.
  29. Andrade, J.S., *Hydrodynamic Dispersion in Binary Packings of Spheres.* Physica A, 1993. **199**(3-4): p. 431-444.
  30. Gurrieri, S., et al., *Real-time imaging of the reorientation mechanisms of YOYO-labelled DNA molecules during 90 degrees and 120 degrees pulsed field gel electrophoresis.* Nucleic Acids Research, 1996. **24**(23): p. 4759-4767.
  31. Lucy, C.A., L.L.M. Glavina, and F.F. Cantwell, *A laboratory experiment on extracolumn band broadening in liquid-chromatography.* Journal of Chemical Education, 1995. **72**(4): p. 367-374.
  32. Hickey, O.A. and G.W. Slater, *The diffusion coefficient of a polymer in an array of obstacles is a non-monotonic function of the degree of disorder in the medium.* Physics Letters A, 2007. **364**(6): p. 448-452.
  33. Mercier, J.F. and G.W. Slater, *Universal interpolating function for the dispersion coefficient of DNA fragments in sieving matrices.* Electrophoresis, 2006. **27**(8): p. 1453-1461.
  34. Tinland, B., N. Pernodet, and A. Pluen, *Band broadening in gel electrophoresis: Scaling laws for the dispersion coefficient measured by FRAP.* Biopolymers, 1998. **46**(4): p. 201-214.
  35. Meistermann, L. and B. Tinland, *Band broadening in gel*

*electrophoresis of DNA: Measurements of longitudinal and transverse dispersion coefficients.* Physical Review E, 1998. **58**(4): p. 4801-4806.

36. Popelka, S., et al., *Peak dispersion due to geometration motion in gel electrophoresis of macromolecules.* Journal of Chromatography A, 1999. **838**(1-2): p. 45-53.

# Chapter 4

## The Effect of Media Order in DNA Capillary Zone Electrophoresis\*

---

### 4.1 Introduction

Electrophoretic size oriented separation of DNA is a major pillar of DNA analysis and biotechnology downstream. The continuous development of applications in research [1-5] demands improvement of DNA separation speed, throughput, resolution, and cost [6-9]. Electrophoresis relies on the size-dependent mobility of DNA in a sieving matrix, and the separation mechanism rises from the interaction of DNA molecules with the porous structure [10-13]. Electrophoresis in gel, agarose or polyacrylamide, is the most widely used technique, in either slab-gel or capillary configurations [14-16]. Despite its great success over decades, gel electrophoresis (GE) can not easily resolve DNA with size larger than 10 kbp [17, 18]. As a substitute, the method known today as pulse field electrophoresis (PFE), invented in 1984, conquered a size range up to 50 Mbp [19, 20]. The two techniques employ different underlying

---

\* \* A version of this chapter has been published as an extended abstract in MicroTAS 2012, Okinawa, Japan.

mechanisms: GE separation lies in the Ogston sieving regime where DNA's gyration diameter is smaller than the pore size of the media. PFGE functions in the reptation regime, where DNA molecules are significantly stretched and cannot be separated by GE. The resolving power of PFGE comes from size-based differences in the reorientation of elongated DNA chains due to the shift in field directions [10].

With advances in micro and nanofabrication techniques during the last decade, a variety of novel micro- and nano-fluidic devices have been investigated as electrophoresis media, such as the "DNA prism" designed by Austin's group [21, 22], the entropic trapping separation by Craighead's group [23-25], magnetic field induced assembly of paramagnetic particles invented by Viovy's group [26, 27], and the nanopillar sieving array in a quartz microchip developed by Baba's group [28, 29]. Miniaturized devices have advantages such as less Joule heating [21, 26, 30], faster separation, smaller sample amount [31], and an ability to integrate and to make portable [32-34], although the fabrication process may be complicated and expensive.

Colloidal self-assembly (CSA) was employed within microfluidic devices to create a sieving matrix for separation, as these are much easier to fabricate and lower in cost compared with nano-fabricated configurations. Wirth's group established that a slab format of self-assembled inorganic particles can serve as replacement to gels for electrophoresis [35]. Our

group has developed CSA of monodisperse silica particles within microfluidic devices as a powerful tool to fabricate highly ordered nanoporous media, and accomplished DNA capillary zone electrophoresis and pulsed field electrophoresis [36, 37]. With this breakthrough in monodisperse CSA structures, some other combinations were studied in our group to further explore aspects of the DNA separation mechanisms. Structures with a pore size step gradient could be formed as zones of monodisperse arrays of different particle sizes (Chapter 2). More interestingly, the self-assembly approach provides an opportunity to systematically study the effect of matrix order on DNA separation. Monodisperse particle suspensions form uniform, ordered structures similar to microfabricated arrays, while bidisperse particle suspensions, exhibit disorder as a function of the particle ratio, and have some similarity to the disordered structure of gels. By changing the ratio of the particle concentrations in bidisperse system, structures with different degrees of disorder can be fabricated easily and reproducibly (Chapter 3). Two-dimensional asymmetric pulsed field electrophoresis (APFE) of DNA within our ordered and disordered arrays has shown a non-monotonic dependence of the resolution on the media order. An ordered matrix is up to 3 times more efficient than a disordered matrix, with an optimal on short-range order [38]. That report was the first systemically experimental investigation on the effect of matrix order in DNA electrophoresis.

It should be noted that the literature are still contradicting about the influence of order in sieve-based electrophoresis. Hickey and Slater suggested by Monte Carlo simulation that their non-monotonic change in diffusion coefficient of DNA chains with order is because of the competition of two opposite dependencies upon order: increasing order favors reptation, while decreasing order favors entropic trapping [39]. Since our APFE separation relies on the reorientation of elongated molecules and the reptation mechanism, the presence of disorder is believed to be unfavorable, due to higher frequency of analyte-media interaction such as collisions, hooking and hernia. In another simulation of collision induced separation in sparse post arrays, Patel and Shaqfeh [40] concluded random arrangements would produce better separation than ordered. Mohan and Doyle [41] refined that model and claimed that sparse post arrays with local order but long range disorder, would give the best separation, following by disordered arrays, with ordered arrays the worst. Wirth and colleagues [35] speculated in their experiments that high efficiencies in CSA devices was obtained as a result of the high degree of order, while Ahn and coworkers [42] thought defects had prevented them from achieving high efficiencies, paradoxically. It is credible to assert, however, that the effect of order upon electrophoresis depends crucially on the separation mechanism, likely explaining the partial agreement and the discrepancies among models and experiments.

Within the Ogston regime, where the sieving mechanism dominates, Slater's simulation indicated that in an ordered obstacle lattice with gaps much larger than the analytes, the electrophoretic mobility is smaller and has a more curved dependence on the gel concentration than would a random lattice with similar density [43]. Locke proposed a correction to the Ogston dispersion coefficient involving media geometry and field distribution in porous media by a volume averaging model [44]. Their simulation of particle diffusion among obstacles also confirmed the dependence on the obstacle geometry, arrangement and dimension [45]. Those models, although intriguing, have not been tested experimentally. With the advantages of our binary CSA structures, the effect of matrix order in one-dimensional DNA capillary zone electrophoresis (CZE) within the Ogston regime is investigated systematically in this chapter. The degree of order is quantified as well as pore size distribution, and the two major indicators, electrophoretic mobility and dispersion coefficient, are explored in regard to the effect of matrix order on their behavior.

## **4.2 Experimental**

### **4.2.1 Microfluidic chip fabrication**

DNA CZE was conducted in poly(dimethylsiloxane) (PDMS) microchips with a double T injection design (Figure 4.1 a, b), with channels

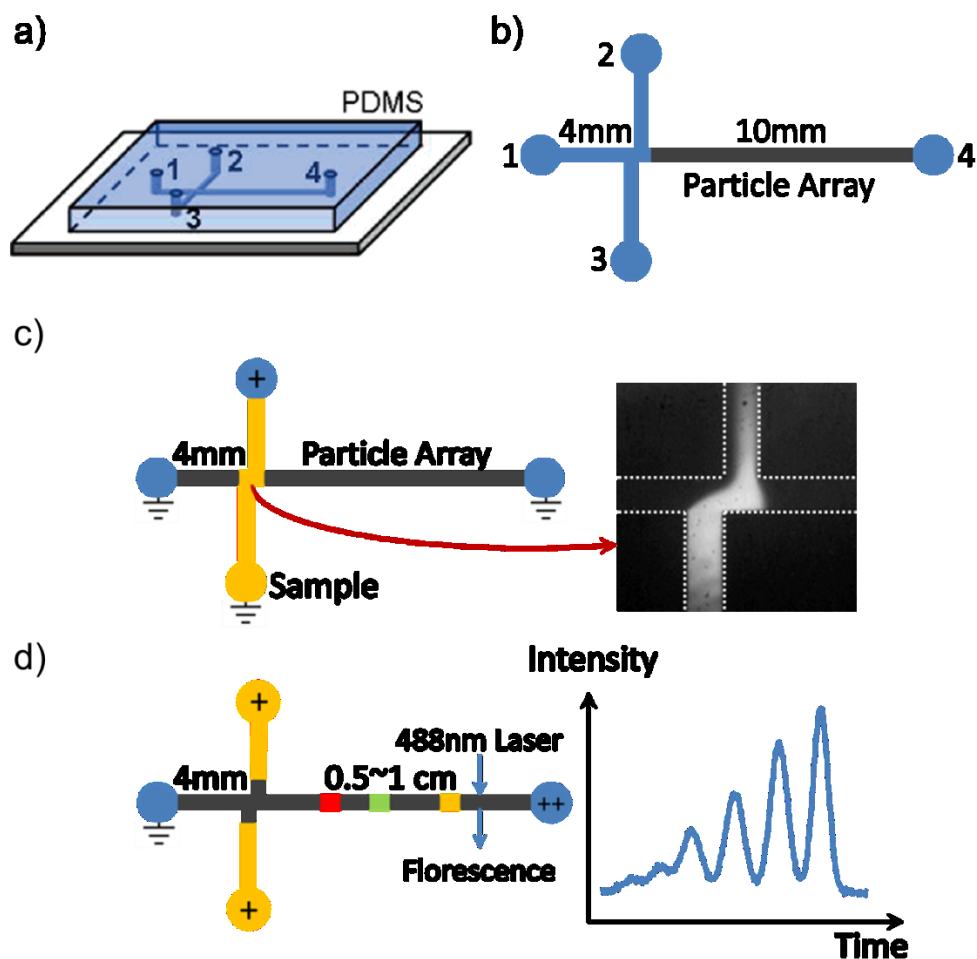


**Figure 4.1.** Chip structure and experimental setup. a) A PDMS chip on a glass slide. b) Chip design and reservoirs. c) Injection, the picture on the right is the fluorescent image at the crossing region. d) Separation, the right image is the intensity profile from fluorescent imaging signals.

~100  $\mu\text{m}$  wide and ~20  $\mu\text{m}$  deep. The length was 4 mm for buffer and injection channels and 5~10 mm for the separation channel. Chips were fabricated through standard soft-lithography [46]. A positive photoresist (AZ-4620, Clariant Corporation, Charlotte, NC) was patterned by UV on a 4-inch silicon wafer, and silanized to facilitate the removal of PDMS. A 10:1 (m:m) mixture of PDMS base with the curing agent (PDMS kit

purchased from Sylgard 184, Dow Corning, Midland, MI) was poured over the wafer mold, and incubated at 60°C overnight to form negative PDMS copies. After PDMS was removed from the master and reservoir holes were punched, devices were assembled by sealing PDMS replicas to glass slides pre-cleaned with piranha solution.

Aqueous suspensions of monodisperse spherical silica particles of 540, 690, and 900 nm in diameter (10% v/v, Bang Laboratories, Inc., Fishers, IN) were used to form self-assembled particle arrays. For binary packed arrays, two monodisperse suspensions were mixed in advance according to the volume ratio required. All suspensions were ultrasonicated for 10 min prior to use.

The process of microfluidic colloidal self-assembly is as follows. A 10-15  $\mu\text{L}$  suspension was injected into reservoirs 1,2, and 3 (Figure 4.1b). The suspension flowed through the channels spontaneously, forming a liquid meniscus at the outlet of the channel to reservoir 4. Reservoirs 1, 2, and 3 were covered with a piece of PDMS to prevent water evaporation once all channels were filled, while reservoir 4 was left open, so that colloidal self-assembly from the opening was induced by solvent evaporation. The growth of the array can be stopped by replacing the suspension in the reservoirs with water.

Subsequent steps depend on the goal. For SEM, the chip was dried completely and the PDMS on top was removed, leaving the glass substrate

with a dehydrated particle array on it. Then the chip was sputter coated with Cr before SEM observation.

For electrophoresis, the water in the reservoirs was substituted with the running buffer and the device was allowed to equilibrate under saturated water vapour environment overnight before separation.

#### **4.2.2 DNA Zone Electrophoresis**

All reagents and samples were prepared with deionized water (18.2 M $\Omega$ ) obtained from an ultrapure water system (Millipore, Milford, MA). The low DNA mass ladder is from Invitrogen. 4 kbp and 10 kbp DNA were obtained from Fermentas (Thermo Fisher Scientific). The intercalating fluorescent dye YOYO-1 (Molecular Probes, Eugene, OR) was used to label DNA samples, at a dye-to-base pair ratio of  $\sim$ 1:10 in 4xTBE buffer (356 mM Tris-borate, 8 mM EDTA, pH=8.3, I=0.12 M) with 4% (v/v) 2-mercaptoethanol as anti-photobleaching agent. The final DNA concentration in buffer was  $\sim$ 50 ng/ $\mu$ L.

4 $\times$ TBE buffer with 2-mercaptoethanol was also used to reduce the electroosmotic flow (EOF). The packed chips were pre-equilibrated under  $\sim$ 20V/cm electric field before separation. Samples were injected from reservoir 2, by applying a 60-80 V potential to reservoir 3 with the other reservoirs grounded to form an injection plug at the crossing region. (Figure 4.1c) Separation was conducted under a field 18.4 V/cm with a pull-back

voltage applied to reservoirs 2 and 3 to prevent leakage from the injection channels to the separation channel. (Figure 4.1d)

With 488 nm argon laser excitation, the separation was detected with a sensitive CCD camera (Astrovid, StellaCam) associated with a lab-built epifluorescence microscope composed of a 550DRLP dichroic mirror, 515 nm long-pass filter, and a 40x planachromat objective (0.6 N.A., LDN, Carl Zeiss). A 4x objective (0.1 N.A., Olympus) was used for imaging under low-magnification. Videos were captured by VirtualDub (1.9.11, Avery Lee) and analyzed by ImageJ (1.44p, NIH, USA). The electrophoresis experiment in each CSA structure was repeated three times in different chips.

### **4.2.3 Differential Scanning Calorimetry (DSC)**

The experimental procedure for DSC deviated from the method developed by Ishikiriyama et al. [47, 48]. Each sample was prepared by drying a 40  $\mu$ L portion of particle suspension in a hermetic aluminum pan for more than 3 h under normal pressure and room temperature. 20  $\mu$ L deionised water was then added into the completely dried pan, a vacuum was applied for 1 h to remove air trapped in the pores and the lid was sealed onto the pan with the sample saturated by water prior to measurement. The empty pan with lid was weighed before sample preparation.

A Q1000 DSC by TA Instruments was used in our experiments. The

temperature sequence is as following: 1) 1st cooling: from room temperature to -30 °C by -10 °C/min; 2) equilibrate at -3 °C for 5 min; 3) 1<sup>st</sup> heating: from -3 °C to 3 °C by 0.05 °C/min; 4) rapidly cool -30 °C; 5) sweep at 1 °C/min to 0.1 °C and equilibrate for 5 min; 6) 2nd cooling: from -0.1 °C to -3 °C by -0.05 °C/min. A ramping rate as slow as 0.05 °C/min was used to avoid thermal and time delays in the DSC curve. The heat flow and temperature of the DSC curves were calibrated by the melting of pure water. Each type of structure was measured twice. Data was processed by TA Universal Analysis 2000 (V 4.5A, TA Instruments).

At the end of each DSC experiment, holes were punched on the sealed pan to assist the sample drying under vacuum, at room temperature for more than 4 h. The dried sample with pan was weighed after drying, to determine the mass of silica in the structure.

## **4.3 Results and Discussion**

### **4.3.1 Characterization of the Matrix Order**

The mixing of binary packed structures is described by the ratio noted as X:Y, equal to the volume ratio between total volumes of 540 nm and 900 nm particles in the mixture. The volume fraction of 900 nm particles  $\chi_{900}$  is calculated as  $Y/(X+Y)$ .

All CSA structures were characterized by SEM images. (Figure

4.2a) With the help of image analysis, the centers of all particles in the images were identified, and the coordinates of the centers were then extracted and analyzed. The degree of hexagonal order in those two-dimensional images can be evaluated by the global bond orientational order parameter,  $\psi$ , defined as

$$\psi = \frac{1}{N_p} \left| \sum (\cos 6\omega + i \sin 6\omega) \right| \quad (4.1)$$

where  $i$  is the imaginary unit,  $\omega$  is the angle between a line bonding nearest particles and an arbitrary reference axis, and  $N_p$  is the total number of particles.  $\psi$  approaches 1 for perfect hexagonal order and trends to zero for completely random arrangements[49, 50]. In order to prevent bias to the most extent, images containing more than a hundred particles were taken at different locations on each chip, a  $\psi$  value was measured for 10-20 central particles randomly picked in each image, and all values obtained through the whole structure were averaged.

The variation of  $\psi$  was calculated with respect to  $\chi_{900}$  of the binary packing (black squares shown in Figure 4.2b) forms a concave shAPFE, with a maximum disorder in 1:1 structure ( $\chi_{900} = 0.5$ ). In monodisperse packing (red circles in Figure 4.2b) the degree of order is relatively high, even though smaller than the ideal case of 1, due to particle size variation and defects. Despite those arguments: i) none of the mixed packing represent a fully random arrangement with  $\psi = 0$ , ii) the order quantified is

limited within short range since only the immediate neighbours to each central particle are considered by the  $\psi$  function, iii)  $\psi$  only represent hexagonal order and may be misleading when other types of order presents such as cubic symmetry, and iv) the non-monotonic change of  $\psi$  suggests different degrees of disorder can be introduced and controlled systemically. Overall,  $\psi$  can be qualified as a descriptive parameter for the matrix order.

The long-range colloidal order in two-dimensional images can be

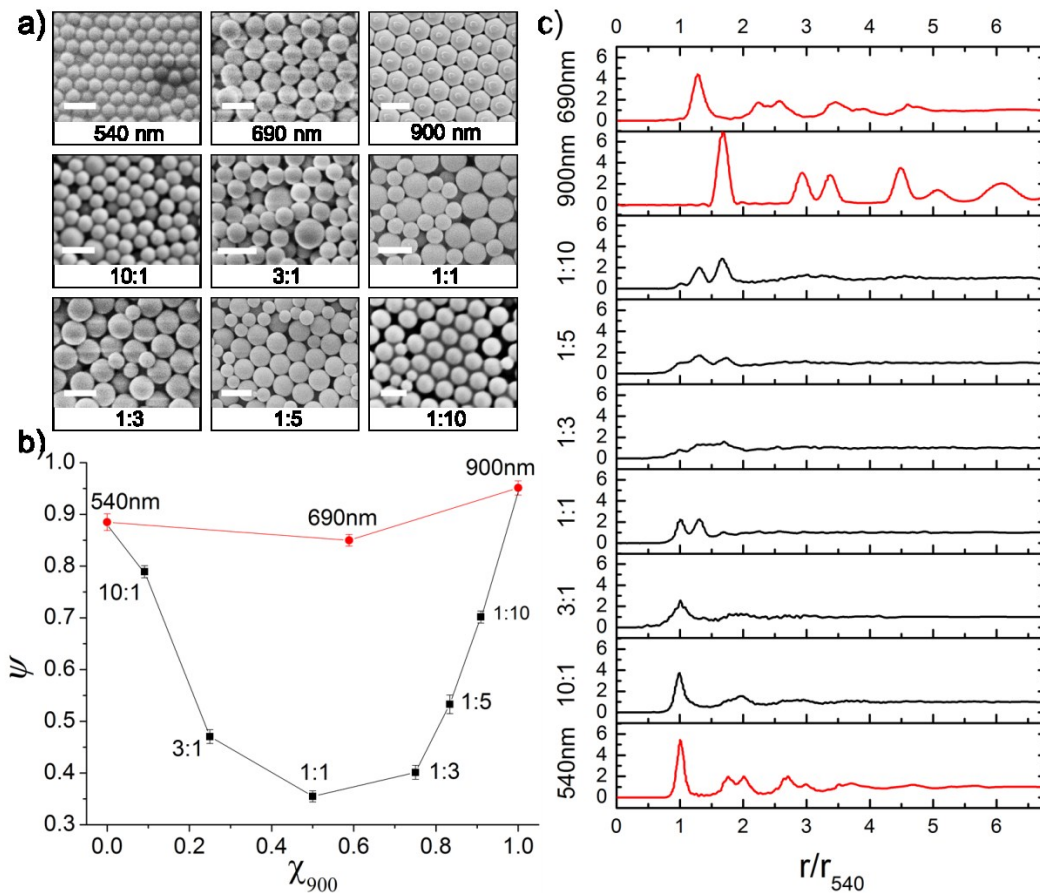


**Figure 4.2.** a) SEM images, scale bars represent 1  $\mu\text{m}$ , b) orientational order parameter of CSA structures, and c) radial distribution function, the distance,  $r$ , is scaled by the radius of the 540 nm particles,  $r_{540}$ . All ratios are the volume ratio between the 540 and 900 nm particles.

evaluated by the radial distribution function,  $g(r)$ . Figure 4.2c shows plots of  $g(r)$  calculated for the particle centers determined for each corresponding SEM image. The number and magnitude of the peaks in the plot of  $g(r)$  with respect to the distance,  $r$ , represent the degree of order in the structures [49, 51, 52]. The  $g(r)$  curve of each structure is consistent with its corresponding  $\psi$  value, although it can only characterize the CSA structures qualitatively. The  $g(r)$  curves of binary packed beds (black curves in Figure 4.2c) exhibit less and flatter peaks, and the peak height attenuates faster as distance increases, too. Highly-ordered monodisperse arrays (red curves in Figure 4.2c) have multiple intense peaks, in agreement with their high  $\psi$  values. However,  $g(r)$  always becomes flat if the distance is long enough ( $r/r_{540} > 6$  in Figure 4.2c), indicating that even in monodisperse beds, the order is limited to a certain distance. This may be because defects are present in the long range order, and the different orientations present in polycrystalline packing.

### **4.3.2 Model of Pore Size Distribution for Binary Packed Structures**

The mixing in binary packed structures may also alter the pore size distribution (PSD). Intuitively, PSD is very sharp in mono-packed structures, and broader in binary packed structures. A number of mathematical models have been proposed to describe the PSD in binary

packing.

The Dodds' model for the pore size distribution of binary packed structures is built on a geometric representation of the packing [53, 54]. A basic assumption involved is the packing is compact. In other words, all particles closely touch each other. Each pore is the void space confined by four adjacent particles, and the packing space can be entirely divided into tetrahedral subunits by connecting the center of the four spherical particles around each pore. The packing is composed of five possible types of subunits of different combinations of size (1st row in Table 4.1) in terms of small (S) and large (L) particles, i.e., 540 nm and 900 nm particles, respectively, in our work. The tetrahedron frequency distribution  $p$  can be determined by a binomial expression of the appearance probabilities of small,  $f_S$ , and large particles,  $f_L$ , both dependent to the particle size ratio, S/L, and the number ratio related with the volume ratio.

The algorithm to quantify pore size is to represent the network of pores as connection of cylindrical tunnels with the same volume and surface area. The equivalent pore radius,  $R_p$ , could then be derived from the pore volume,  $V_p$ , and the surface area,  $A$ , of the subunit.

**Table 4.1.** Probability and scales of five types of subunits combinations.

Combination	SSSS	SSSL	SSLL	SLLL	LLLL
$P$	$f_S^4$	$4f_S^3f_L$	$6f_S^2f_L^2$	$4f_Sf_L^3$	$f_L^4$
$V_T/\mu\text{m}^3$	0.01856	0.02732	0.03993	0.05827	0.08591
$V_p/\mu\text{m}^3$	0.004089	0.005772	0.008358	0.01240	0.01893
$A/\mu\text{m}^2$	0.1206	0.1534	0.1889	0.2489	0.3349

$$R_p = \frac{2V_p}{A} \quad (4.2)$$

Thus, the pore size distribution is a discrete pentamodal model and the average pore size from Dodds' model  $a(\text{DM})$  is given by:

$$a(\text{DM}) = \frac{2 \sum PV_p}{\sum PA} \quad (4.3)$$

The calculated average pore size is plotted against  $\chi_{900}$  for the 540/900 nm combination ( $\varphi = 0.6$ ) in Figure 4.3. The average pore size increases monotonically with the volume fraction of the larger particle. Also shown in Figure 4.3 is the probability,  $P$ , of each of the five tetrahedral combinations. While in mono-packed structures only one type

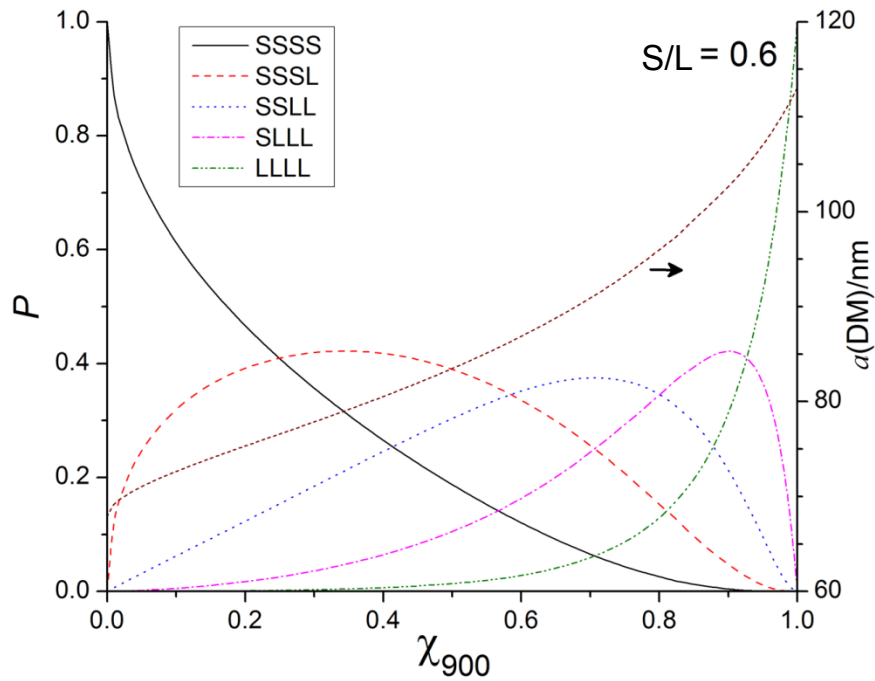


**Figure 4.3.** The calculated average pore size ( $a$ ) and pore size frequency distribution ( $P$ ) in 540/900 nm binary packed structures.

of pore presents, in binary packed structures Figure 4.3 shows there can be up to five different types present, of considerable amount at certain volume fractions (e.g.,  $\chi_{900} = 0.7$ ).

### 4.3.3 Thermoporosimetry

Thermoporosimetry is a technique alternative to gas absorption or mercury intrusion methods used to characterize the texture of porous materials. The melting point of a liquid confined in pores, water for example, shifts downward relative to its normal value, described quantitatively by the Gibbs-Thomson equation [55, 56]

$$\Delta T = T_p - T_0 = \frac{2\gamma_{sl}T_0 \cos \iota}{\Delta H_{\text{fus}}\rho_s r_w} = \frac{\alpha}{r_w} \quad (4.4)$$

where  $\Delta T$  is the difference between the melting temperature of confined liquid,  $T_p$ , and the normal melting point of the same liquid,  $T_0$ ,  $\gamma_{sl}$  is the surface energy of the solid-liquid interface,  $\iota$  is the contact angle,  $\Delta H_{\text{fus}}$  is the enthalpy of fusion,  $\rho_s$  is the density of the ice, and  $r_w$  is the radius of the confined lump of freezable water.

It is also known, however, that not all the liquid participates in the phase transition and a significant amount remains absorbed on the pore surface. Hence the radius from the Gibbs-Thomson equation should be increased by the thickness,  $\beta$ , of the absorbed solvent layer to reach the total pore radius [57]:

$$R_p = r_w + \beta = \frac{\alpha}{\Delta T} + \beta \quad (4.5)$$

Given the preliminarily determined coefficients of the solvent in use, this equation makes it possible to determine the pore size distribution (PSD) of materials by simply measuring  $\Delta T$ . The  $\alpha$  value is obtained from the optimization done by Ishikiryama et al. [48]. It has been proposed that the absorbed non-freezable water layer contains 2~3 monolayers of water molecules. Thus  $\beta$  could be assumed to be 1.0 nm, which corresponds to nearly three monolayers of water[58].

Both Differential scanning calorimetry (DSC) [59] and NMR [60, 61] could accomplish the PSD quantification of pore radius higher than 1 nm [62]. In the DSC method we used, heat flow is recorded during the cooling and heating cycles around the melting point of water. A typical DSC scan for 540 nm silica CSA filled with water is shown in Figure 4.4. The first cooling scan produces a huge exothermic peak starting below -10 °C, which represents the supercooling effect of both bulk water and confined water since no bulk ice is present in the system and the pore size is larger than that of bulk ice nuclei[48]. In the heating scan, two endothermic peaks can be observed for all samples. The peak of higher temperature starting at around 0 °C corresponds to the melting of bulk water, while the smaller peak on the lower temperature side could be attributed to the melting of freezable water confined in CSA pores. The

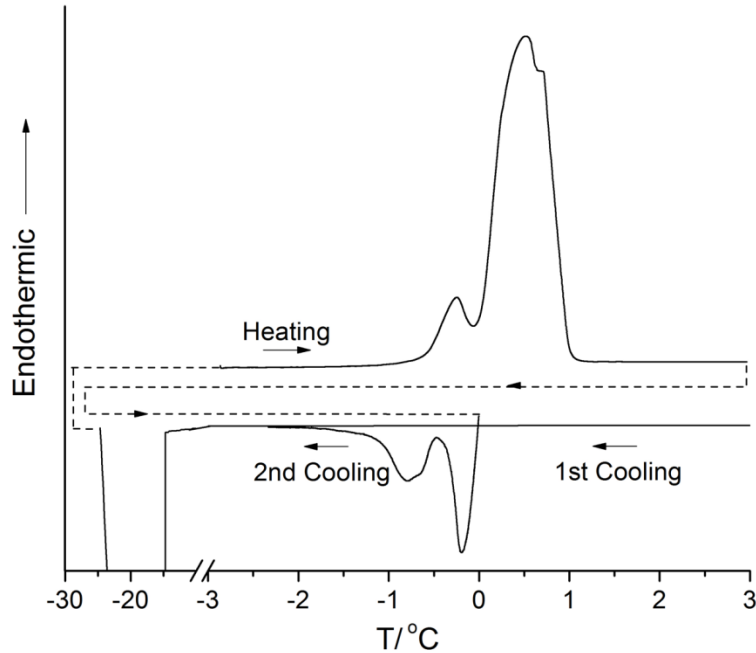


**Figure 4.4.** DSC curve for 540 nm monodisperse particle array, arrows indicate the direction of scans.

sample is then cooled again to freeze all the water, and heated up to 0.1 °C, under which the bulk water is only partially melted, still with ice presents in the system, in order to prevent the water from being supercooled in the following freezing scan. With bulk ice, water then freezes at 0 °C for bulk, and the freezing peak for confined water is observed at a lower temperature as predicted.

Only the freezing peak is used to calculate the pore size distributions, because the melting peak of water in pores is closer to and overlapping more significantly with the bulk. The heat flow signal,  $dQ/dt$ , in a DSC curve is transformed into the pore volume distribution (PVD) by the equation:

$$PVD(R) = \frac{dV}{dR} = \frac{dQ}{dt} \frac{dt}{dR} \frac{1}{m\Delta H_{\text{fus}}\rho_w} \frac{R^\nu}{r_w^\nu} \quad (4.6)$$

where  $m$  is the weight of silica, and  $\rho_w$  is the density of water.  $\nu$  is the exponential factor of the pore shAPFE. Cylindrical pores are used here with  $\nu=2$  in order to be consistent with the Dodds' model.

The PVD of total pore sizes,  $dV_t/dR_t$ , should be derived by employing the total pore radius,  $R_t$ , as  $R$  in equation 4.6. The total pore volume,  $V_p$ , and surface area,  $A$ , are:

$$V_p = \int \frac{dV_p}{dR_p} dR_p \quad (4.7)$$

$$A = \int \frac{2}{R_p} \frac{dV_p}{dR_p} dR_p \quad (4.8)$$

and the average pore size is calculated by:

$$a = \frac{2V_p}{A} \quad (4.9)$$

The pore volume distribution, average pore size and some other descriptive statistics are shown in Figure 4.5. The DSC average pore size  $a(\text{DSC})$  (Figure 4.5b) and the peak pore diameter  $R(\text{peak})$  (Figure 4.5c) both increase with the average pore size from Dodds' model, consistent with the shift of the PVD curves in Figure 4.5a.

The apparent agreement between pore size estimates from DSC and

the theoretical model is surprising. In the case of Dodds' calculation, the close-packed assumption would be expected to underestimate the pore size and porosity, because of defects and cracks in the actual structures. Moreover, this geometric interpretation as a framework of tetrahedral subunits ignores the larger octahedral voids that are also present. One third of the pores have to be octahedral in a monodisperse close-packing. This is geometrically proved as regular tetrahedron cannot tessellate 3-dimensional Euclidean space. The presence of certain types of irregular tetrahedrons in binary packing may loosen, but cannot completely cancel, the demand for octahedrons. Hence the calculated pore size is subject to downward bias since octahedral spaces are ignored. It should also be noted that the model does not take into account the import of particle size variation in the real sample.

In the case of thermoporosity, on the other hand, it is reasonable to expect corresponding pore size estimates to be larger because water expands when freezing, possibly increasing pore size by altering the conformation of the structure. This problem could be corrected at least partially since the  $\alpha$  value used was optimized towards the PSD from gas absorption, which should not suffer from the expanding issue, but the difference still needs consideration [48]. From another perspective, the pore size range we were trying to measure is close to the upper limit of thermoporosity, the largest ever to our knowledge. As the tail of the bulk

water freezing peak always extends to  $-0.5\text{ }^{\circ}\text{C}$ , the freezing signal of confined water cannot be distinguished beyond this temperature, making any pore radius more than about 110 nm undetectable. This helps to eliminate the upward error from cracks introduced in sample preparation. Nevertheless, the average pore size may still be underestimated because a certain portion of the pore distribution at the large end is cut off. In Figure 4.5b, the effect of expansion and the tail cut off in DSC seem to correct each other. Thus, the measured average pore size,  $a(\text{DSC})$ , agrees well with the modeled pore size,  $a(\text{DM})$ , in the size range smaller than  $\sim 95\text{ nm}$ . When 900 nm particles are in majority, however, the portion of large pores is higher. In this case, the tail cut off effect outweighs, and  $a(\text{DSC})$  is more underestimated compared to  $a(\text{DM})$ . This could explain the downward bend of the points on the large end in Figure 4.5b.

Several other statistical descriptive factors of the pore volume distribution are plotted versus the modeled pore size,  $a(\text{DM})$ , in Figure 4.5 d, e and f. The standard deviation,  $\sigma(\log R)$ , is positively correlated with  $a(\text{DM})$  (Figure 4.5d), which represents the peak width. The distribution is always leptokurtic, with excess kurtosis,  $\text{Kurt}(\log R)$ , larger than zero, the benchmark of normal distribution. Kurtosis is larger for sharper peaks. The decreasing trend of  $\text{Kurt}(\log R)$  shows that the distribution approaches normal distribution as the pore size goes up (Figure 4.5e). The skewness,  $\text{Skew}(\log R)$ , measuring the peak symmetry, changes from negative to zero

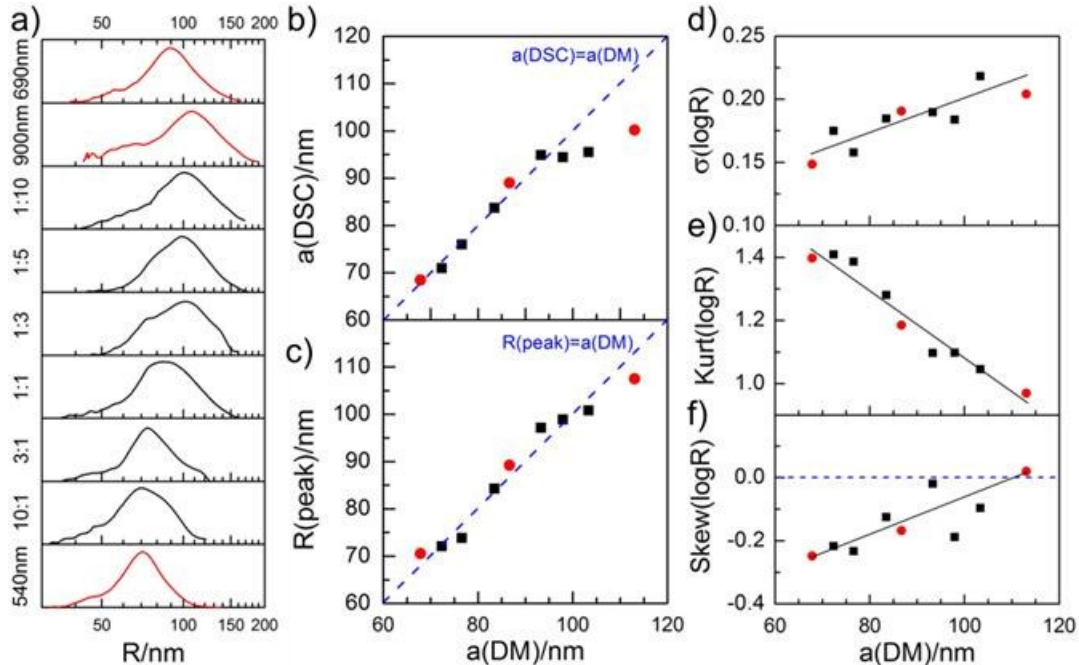


**Figure 4.5.** Pore volume distribution, average pore size,  $a(\text{DSC})$  and several descriptive statistics parameters: peak diameter,  $R(\text{peak})$ , standard deviation,  $\sigma(\log R)$ , excess kurtosis,  $\text{Kurt}(\log R)$ , and skewness,  $\text{Skew}(\log R)$ , of the distribution over the logarithm of pore diameter,  $\log R$ , obtained from DSC for CSA structures. Red color corresponds to monodisperse structures.

(Figure 4.5f), showing a more and more symmetric distribution. All the DSC parameters shown, the measured average pore size, peak pore size, standard deviation, kurtosis, and skewness, correlate monotonically with the pore size calculated by Dodds' model,  $a(\text{DM})$ . Since  $a(\text{DM})$  is calculated rather than measured experimentally, it is also free from many practical issues. For example, the packed structures for DSC, subject to the coffee ring effect and the absence of support from channel walls on chip, can be readily argued to give different pore distribution. According to all these discussions, it is valid and expedient to regard  $a(\text{DM})$  as a

representative description of a group of media properties related to pore size distribution.

#### 4.3.4 Porosity and the Accessible Fraction

The overall porosity,  $\varepsilon$ , can be averaged from the volumes of the five types of subunits in Dodds' model:

$$\varepsilon = \frac{\sum PV_p}{\sum PV_T} \quad (4.10)$$

And From DSC measurements, the porosity of the packed structure is:

$$\varepsilon = \frac{V_p}{V_p + 1 / \rho_{\text{SiO}_2}} \quad (4.11)$$

$\rho_{\text{SiO}_2}$  is the density of amorphous silica.

As in Figure 4.6a, the Dodds' model porosity follows a slightly concave trend similar to other models in the literature [63, 64], but all data are consistently smaller than 0.26—the porosity of face-centered cubical (fcc) or hexagonal close packing (hcp) of uniform particles, because of taking the gapless assumption and ignoring the octahedral voids. The porosity from DSC measurement, however, is always larger than 0.3. This indicates the presence of defects and perhaps the systemic error from expansion on freezing. While showing different absolute values, both of the traces of porosity are almost flat. This relative uniformity means that the addition of the second particle to the primary particles will affect the

average porosity far less than the degree of order, and thus the porosity change should not be a significant contributor to the variation of separations.

At the pH in our experiments, DNA molecules and the silica surface are both negatively charged, causing a non-accessible layer on the surface due to electrostatic repulsion [65] and the immobile Stern layer on the surface [66]. The scale of this electrostatic interaction is estimated to be about 1 nm, accounting for the Debye length under the ionic strength of the buffer we used [67]. Moreover, since it is assumed in the Ogston-Morris-Rodbard-Chrambach (OMRC) model that the DNA chain coils as a rigid globular particle (Section 1.3.2.2), its mass center could not approach the surface within a distance smaller than its radius of gyration [68, 69]. Thus in evaluating the pore size predicted by Dodds' model, the effective void volume should be reduced to estimate the accessible pore volume  $V_A$  for each analyte. The accessible volume fraction of the whole packed array is:

$$f_A = \frac{\sum_{R_p > R_g} PV_A}{\sum PV_T} \quad (4.12)$$

The accessible fraction estimated by DSC requires similar corrections. The pore size should be also modified, being reduced by the effect of the electric double layer,  $\gamma$ , and the gyration radius,  $R_g$ , of the DNA:

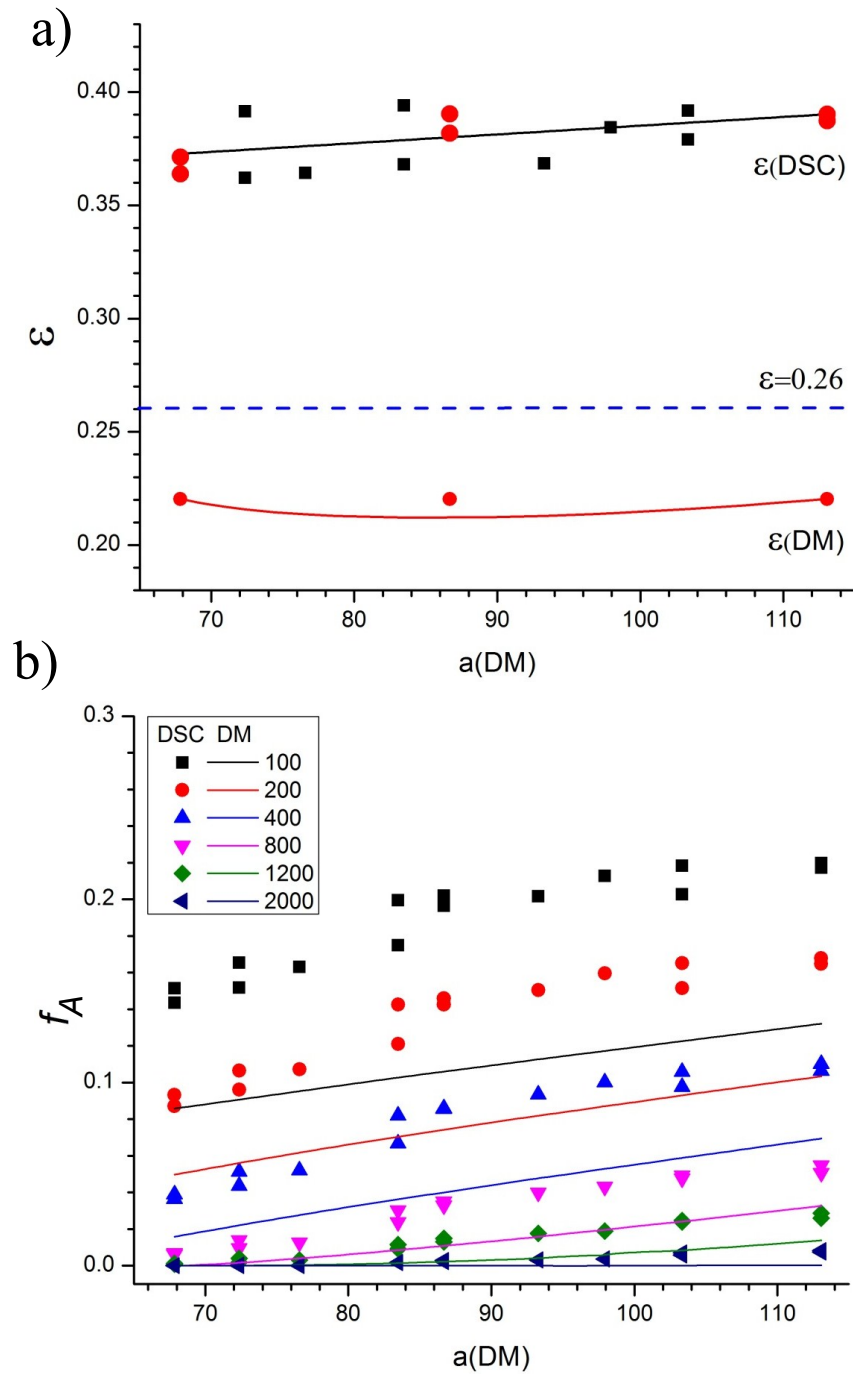


**Figure 4.6.** a) Porosity from DSC,  $\epsilon(\text{DSC})$ , and Dodds' model,  $\epsilon(\text{DM})$ , red circles represent the monodispersed structures, the blue dashed line is the porosity of fcc or hcp packing; b) accessible volume fraction ( $f_A$ ) from DSC (dots) and Dodds' model (lines), with different color for each DNA size.

$$R_A = \frac{\alpha}{\Delta T} + \beta - \gamma - R_g \quad (4.13)$$

$\gamma$  is estimated to also be about 1 nm as discussed, commensurate with  $\beta$ . So the  $\beta$ - $\gamma$  term is negligible. When the accessible radius  $R_A$  is used as  $R$  in equation 4.6, it gives a specific accumulative accessible pore volume,  $V_A$ , and the accessible volume can be obtained through integration:

$$V_A = \int \frac{dV_A}{dR_A} dR_A \quad (4.14)$$

The DSC accessible fraction:

$$f_A = \frac{V_A}{V_p + 1/\rho_{\text{SiO}_2}} \quad (4.15)$$

The accessible fraction is plotted against  $a(\text{DM})$  in Figure 4.6b. The accessible fraction obtained from DSC is unsurprisingly much larger than the one modeled for every DNA size, given the same reasons discussed before. All the fraction values in Figure 4.6b are smaller than about 0.2 in general, which means the packing, with more than 80% of the total volume obscured, is much denser than in hydrogels or structures modeled by Slater and Doyle et al. [70, 71]. The accessible fraction is a monotonic function of the DNA size and pore size, larger for smaller molecules and larger pore size, and is above zero up to 2000 bp of DNA size, which is regard as the upper bound of Ogston regime in our electrophoresis.

### 4.3.5 DNA Electrophoretic Mobility

Ogston regime applies in gel electrophoresis when the analyte is smaller than the pore size. The macromolecule chain is assumed to coil as a rigid globular particle with no conformation changes during electromigration and the separation is treated as a filtration process [10]. The classic OMRC model [72-75], valid for random media with small obstacle concentration and porosity much smaller than the percolation threshold, states that the scaled mobility, i.e., the ratio between the mobility  $\mu$  in the separation media and the free-solution mobility  $\mu_0$ , is equal to the fraction of accessible gel volume fraction,  $f_A$ . The accessible volume depends on the gel concentration,  $C$ , and the DNA size,  $N$ . In random gel,  $f_A$  is determined by the gyration radius of DNA,  $R_g$  and the average pore size of the gel,  $a$ , described in equation:

$$\frac{\mu}{\mu_0} = f_A = \exp\left(-\frac{\pi R_g^2}{4a^2}\right) \quad (4.16)$$

This equation can be derived to the form of Ferguson plot ( $\log \mu$  vs.  $C$ ), which is linear and used as a standard method to determine molecular weight in gel electrophoresis of small analytes including DNA. Equation 4.16 can also be rewritten as:

$$\log \mu = \log \mu_0 - kN \quad (4.17)$$

indicating a linear dependence to the molecular size.

However, it is known that not all Ferguson plots are linear on the semi-logarithm scale [76], and the Ogston mechanism is challenged because many of its simplifying assumptions do not hold in reality, such as inert media surface, no steric effects, and uniform field[44, 77, 78]. Through a series of lattice model simulations [43, 70, 71, 79-81], Slater et al. describe the scaled mobility as a power series:

$$\frac{\mu}{\mu_0} = 1 + a_1 c + a_2 c^2 + a_3 c^3 + \dots (c = 1 - f_A) \quad (4.18)$$

where  $c$  is the obstacle concentration or obstructed volume fraction due to the gel itself. Differing from the OMRC expression, in this model the media texture becomes influential since the magnitude and sign of the coefficients depend on the media geometry, including the crystallographic arrangement of obstacles, and the degree of randomness. The curvature of the plot is positively correlated with the degree of order of the gel structure [43].

To justify our separation mechanism, the logarithmic scaled mobility,  $\log \mu/\mu_0$ , is plotted first over the DNA size,  $N$ , in Figure 4.7. From the curves, it is quite evident that the dependence of  $\mu$  on the DNA size is linear in the size range below 2000 bp. Thus, the Ogston mechanism is valid up to 2000 bp, in agreement with the data on accessible volume fractions in Figure 4.6b. Data points deviate from linear and reach a plateau when the molecular size (4000 and 10000 bp) extends towards the reptation regime.

A nonlinear model was employed in the regression analysis of our mobility data based on the Equation 4.19. Data corresponding to 4000 and 10000 bp DNA was not included since these molecules lie outside the Ogston regime. 100 bp data were also excluded because free solution mobility becomes size dependent for molecules below 200 bp [82, 83].

$$\log \mu = -k_1 \frac{N^{k_2}}{a(\text{DM})^{k_3}} + k_4 \psi + \log \mu_0 \quad (4.19)$$

According to the t-statistics shown in Table 4.2, all fitting parameters are statistically significant different from zero at the 95% confident level. The  $\mu_0$  from the regression  $(1.3_5 \pm 0.1_2) \times 10^{-4} \text{ cm}^2/\text{V}\cdot\text{s}$  is comparable with the size-independent free-solution mobility [84]. The regression has a quite large F value of 61.28 and  $R^2$  of 0.982, both showing a good fitting quality.

The DNA size,  $N$ , and average pore size of the media,  $a(\text{DM})$ , are dominant variables, as together they attributes to 89.9% of the total variance of the mobility data. This observation is consistent with the OMRC model except for unequal exponential powers. While it is not clear

**Table 4.2.** Regression results of equation 4.19.

	Estimate	t, t(95%)= 1.97	Statistics
$k_1$	$(1.7_4 \pm 0.5_8) \times 10^2$	3.0	F = 61.28, F(95%) = 2.28
$k_2$	$0.27_4 \pm 0.01_9$	14.4	$R^2 = 0.982$
$k_3$	$1.7_0 \pm 0.1_2$	14.2	$R^2(N, a(\text{DM})) = 0.899$
$k_4$	$0.26_7 \pm 0.01_2$	22.3	$R^2(\psi) = 0.053$
$\mu_0$	$(1.3_5 \pm 0.1_2) \times 10^{-4}$	11.3	

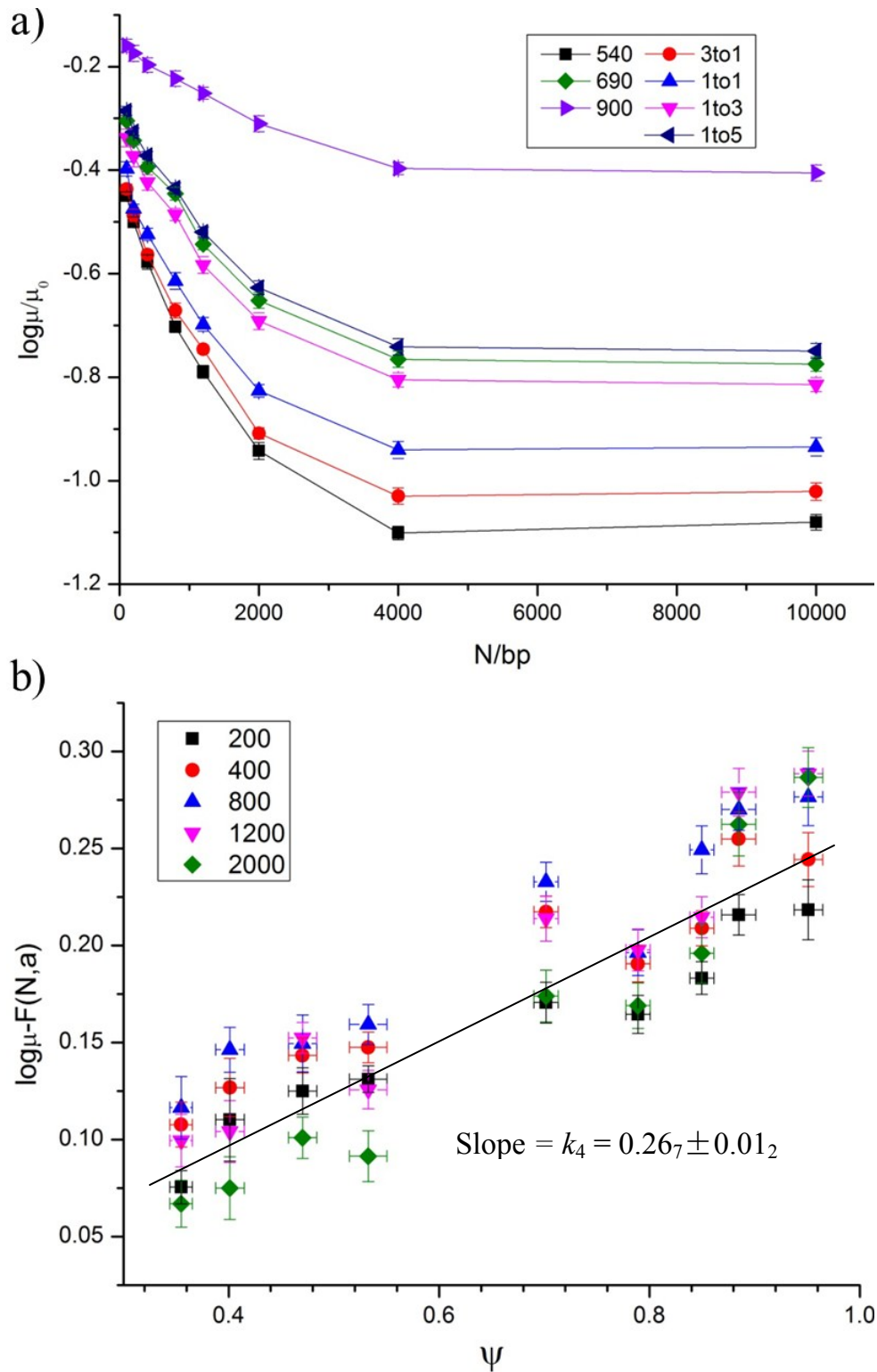


**Figure 4.7.** a)  $\log \mu / \mu_0$  vs.  $N$ . The data of 1:10 and 10:1 binary bed is not shown due to the lack of data for 4 and 10 kbp DNA. b) The left side of Equation 4.20 plotted over  $\psi$ . Error bars represent standard deviations.

how the following factors would influence the exponentials, there are certain strong structural differences in the CSA arrays. These differences include: i) the CSA structures used here do not exhibit complete randomness, with a minimum of 0.3 in  $\psi$  (Figure 4.2b). Slater et al. have calculated that ordered media would show a different dependence than the OMRC exponents in a less dense ordered media [43]. ii) As discussed in Section 4.3.3, the average pore size used,  $a(\text{DM})$ , is biased. This may lead to a compensation in the fitting that adjust the exponent. iii) The packed structures are much more condensed than either hydro gel or obstacle networks simulated in the literature [43, 70, 71]. So the media surface becomes more influential, and distorts the field line more significantly. This may also contribute to the discrepancy about the fitting exponents.

Equation 4.19 can be rearranged to isolate the dependence on order:

$$\log \mu - \log \mu_0 + k_1 \frac{N^{k_2}}{a(\text{DM})^{k_3}} = k_4 \psi \quad (4.20)$$

This allows a plot of  $\psi$  dependence, which shows the residue variation assigned to the lattice order. The values on the left side of Equation 4.20 are plotted against  $\psi$  in Figure 4.7b. The upward trend, together with the slope of  $0.26_7 \pm 0.01_2$  ( $t=22.3$ ), illustrates that mobility is higher when the structure is more ordered. This result is in accordance with Slater's simulation, for which the mobility curve in a random structure is lower than for periodic obstacles [43]. A fraction of 5.3% of the total variance is

assigned to the degree of order quantified by  $\psi$ . This result identifies the influence of the degree of order, which is a considerable supplement to  $N$  and  $a(\text{DM})$ . Thus our data support the effect of media order on electrophoretic mobility. Clearly, efforts to improve the mobility by tuning or reorganizing the media architecture to a greater level of order are warranted.

### 4.3.6 Dispersion Coefficient

The term dispersion coefficient used here is defined as the total band broadening effect during the separation, exclusive of the effects of the width of injection plug and detection window. The term contains components from thermal diffusion, field-induced dispersion, media effects including pore size, order, tortuosity, packing quality, etc. and other parameters such as temperature gradients, buffer viscosity, etc.

The Zimm friction dynamics predicts the diffusion coefficient of diluted long DNA [85] and other polymers [86], where  $\eta$  is the solvent viscosity,  $R_g$  is the radius of gyration:

$$D_0 = \frac{k_B T}{6\pi\eta R_g} \quad (4.21)$$

It is found that this thermal diffusion term remains the governing phenomenon in free-solution electrophoresis [87]. Since molecular diffusion arises from hydrodynamic interactions with the solvent and obeys

the fluctuation-dissipation theorem, while the electrophoretic mobility comes from electrostatic interactions with the electric field, the Nernst-Einstein equation for dispersion coefficient

$$D_E = \frac{\mu k_B T}{N q_e} \quad (4.22)$$

where  $q_e$  is the effective charge density of each base pair, is not valid in free-flow electrophoresis except for molecules smaller than the persistent length ( $\sim 100$  bp for double stranded DNA [88]) and low field. The situation within porous media is different due to the sieving or screening effect from the obstacles. Theory [10, 89] and experimental data [90, 91] both agree that i) the Nernst-Einstein relation is generally not valid in gel electrophoresis, except for very small molecules and very low field, and ii)  $D$  increases with the field intensity and is a weak function of the molecular size in practice.

According to Slater's investigation in 2006 [92], in the Ogston regime, when the size of analytes is much smaller than the pore size (called the Zimm-Ogston regime), the hydrodynamic interaction still dominates, but the media slows down the larger molecules more than the smaller ones, because of the increased probability of collisions. Thus both mobility and diffusion decrease relative to the free-flow case.

When the size of the molecule becomes comparable to the pore size (called the Rouse-Ogston regime), the analyte feels significant excluded

volume interactions and the hydrodynamic interactions are shielded by the obstacles [93], Under this condition, the Zimm model is replaced by the Rouse model, which neglects hydrodynamic interactions to predict a diffusion coefficient as:

$$D = \frac{k_B T}{N \xi_e} \quad (4.23)$$

where  $\xi_e$  is the friction coefficient per base pair.

Accounting for diffusion alone underestimates the observed band broadening [94]. The observed enhancement to the diffusion under electric field was calculated from the scaled Nernst-Einstein relationship:

$$\frac{D_E}{D_0} = \frac{\mu_E}{\mu^*} \quad (4.24)$$

The static diffusion coefficient,  $D_0$ , and the dispersion coefficient,  $D_E$ , are related by the ratio of the mobilities in the presence  $\mu_E$  and absence of an electric field  $\mu^*$  extrapolated from the Ogston relationship. This is a fundamental law of thermodynamics and should be valid near equilibrium. The Nernst-Einstein equation is proved to be valid in low field intensities, when the field lines are parallel to each other [95, 96], or even when the field line is distorted in low fields [80], at least in the Rouse-Ogston sub-regime [92]. However, this equation has been criticized by a number of researchers, pointing out it does not apply in either the Ogston or reptation regime, because electrophoresis is a highly non-equilibrium process [87,

94, 97, 98].

All models mentioned above, valid or not, do not consider the media architecture. Using a volume averaging model, Locke [44] found the dispersion coefficient in porous media is given by:

$$\frac{D_E}{D_0} = f_A + S_1 + S_2 \quad (4.25)$$

where  $S_1$  is a function of the local media geometry and  $S_2$  is a function of the local electrical field and geometry, i.e. an electrical field induced dispersion. Their Monte Carlo simulation of particle diffusion among obstacles also confirmed the dependence on the obstacle geometry, arrangement and dimension [45].

Complementary to the published theoretical studies, the disorder systematically introduced in our CSA structure offers us an opportunity to experimentally learn about the effect of media order on dispersion. To calculate the dispersion coefficient, the electrophoretic peak variance was first corrected for the variance introduced by injection plug, measured from the fluorescent profile captured in the separation channel at a distance of  $\sim 20 \mu\text{m}$  downstream to the double-T crossing region. The variance of detection, along a straight line vertical to the channel in images captured, is negligible since the width is limited to one pixel, equivalent to  $\sim 0.5 \mu\text{m}$ . So the net variance in length due to the separation process is

$$\sigma_{other}^2(x) = \{\sigma_{total}^2(t) - \sigma_{inj}^2(t)\}(\mu E)^2 \quad (4.26)$$

Dispersion coefficients were obtained from the net peak variances.

$$D_E = \frac{\sigma_{other}^2(x)}{2t} \quad (4.27)$$

The effect of pore size and molecular size should be considered when examining the net effect of matrix order on dispersion. If our  $\log D_E$  data are plotted with  $a(\text{DM})$  as the horizontal axis in Figure 4.8a, the binary particle matrix group shows a difference compared with the monodisperse group. It is convenient to calibrate the effect of pore size on dispersion coefficient with arrays of monodisperse 540, 690 and 900 nm particles, but those structures are still subject to a certain degree of disorder, as evidenced by their  $\psi$  values being smaller than one and the scattered defects in the SEM images (Figure 4.2). Multiple regression analysis was used instead, by fitting the dispersion coefficient linearly:

$$\log D_E = k_1 a(\text{DM}) + k_2 N + k_3 \psi + k_4 \quad (4.28)$$

According to the t-statistics in Table 4.3, all fitting parameters are significantly different from zero at the 95% confidence level. The regression has a large F value of 585.18 and  $R^2$  of 0.931, both showing the fitting is quite effective. 88.9% of the variance of the dispersion coefficient can attribute to DNA size,  $N$ , and average pore size,  $a(\text{DM})$ . After the terms containing  $N$  and  $a(\text{DM})$  are netted from  $\log D_E$  in Equation 4.28,

**Table 4.3.** Regression results of equation 4.28.

	Estimate	t, t(95%) = 1.97	Statistics
$k_1$	$0.0141_4 \pm 0.0003_9$	36.3	$F = 585.18, F(95\%) = 2.28$
$k_2$	$-(1.71_9 \pm 0.08_6) \times 10^{-4}$	20.0	$R^2 = 0.931$
$k_3$	$-0.22_5 \pm 0.02_6$	8.7	$R^2(N, a(\text{DM})) = 0.889$
$k_4$	$-8.06_8 \pm 0.03_9$	206.9	$R^2(\psi) = 0.058$

$$\log D_E - k_1 a(\text{DM}) - k_2 N - k_4 = k_3 \psi \quad (4.29)$$

the residue data on the left side of Equation 4.29 is plotted against  $\psi$  in Figure 4.8b. Although the change is ambiguous for each single DNA size, the dependence to  $\psi$  of the entire sample pool is confirmed by statistics, as the slope is significantly negative  $-0.22_5 \pm 0.02_6$  ( $t = 8.7$ ). This trend demonstrates that coherent, ordered structures separate DNA more efficiently than random porous media with comparable average pore size, because of a lower dispersion coefficient. According to the analysis of variance, 5.8% of the variance corresponds to  $\psi$ . The degree of order is again a considerable supplementary to DNA size and average pore size. Doors are open to improve electrophoresis separations further by attenuating the dispersion through tuning the media towards greater levels of order.

## 4.4 Conclusions

The DSC characterization used in this chapter showed its capacity to measure pores with hundreds nanometers' size with ramping rate about 10

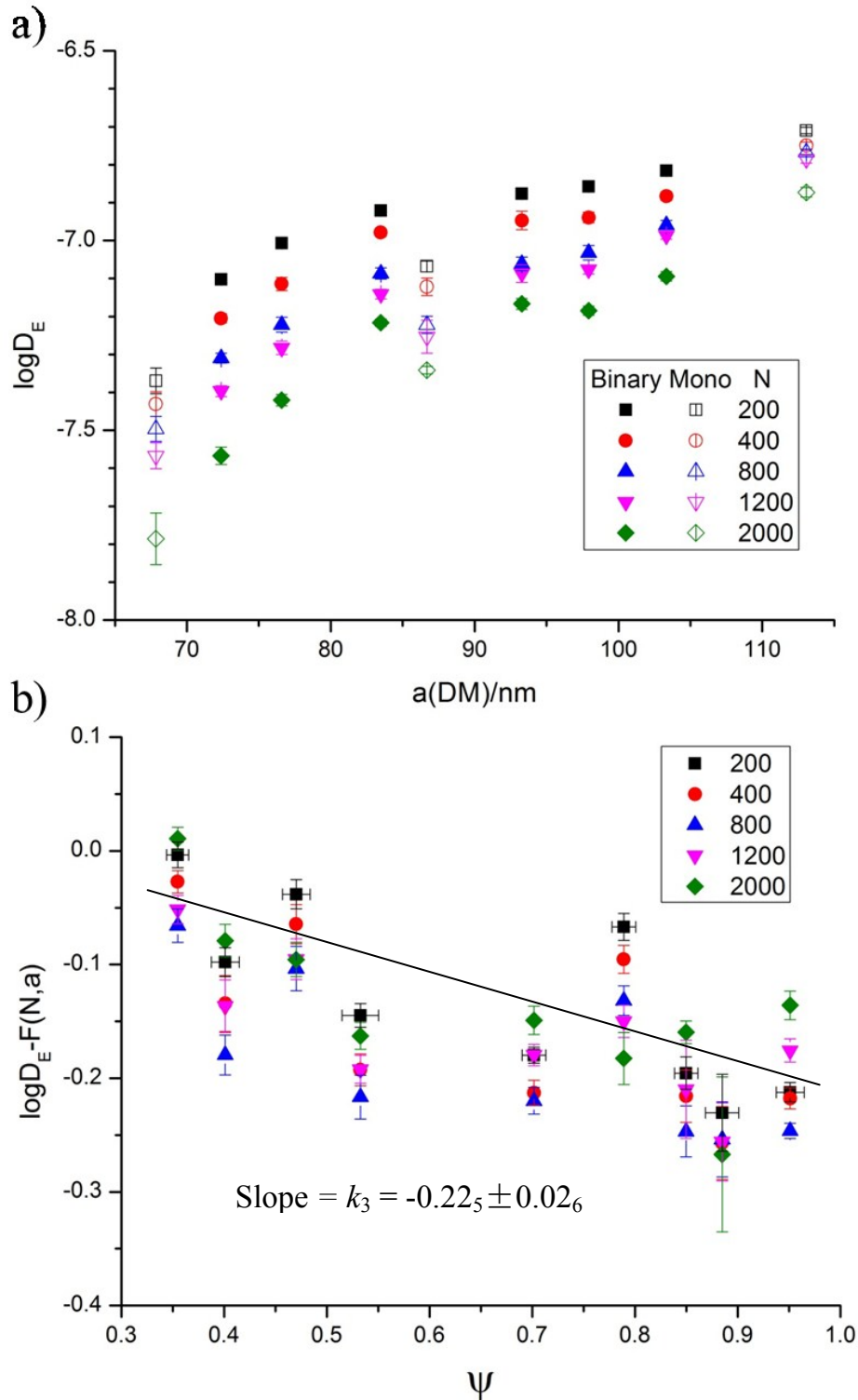


**Figure 4.8.** a)  $\log D_E$  vs.  $a(\text{DM})$ , solid points represent binary packed structures, hollow points represent pure structures; b) the left side of Equation 4.29 plotted over  $\psi$ . Error bars represent standard deviations.

times slower, 0.05 °C /min, to compensate the tiny freezing point depression in this size range. To our knowledge, this chapter reports the largest pore size range DSC has measured. The sample preparation for DSC is subject to more cracks due to the absence of support from channel walls since any substrate would attenuate the sensitivity because of thermal resistance. Nevertheless, this thermoporosity method is still the technique most suited to these samples given the quantity and fragility of the sample. The apparent pore size obtained from electrophoretic mobility using the Ferguson equation is an unacceptable approach here, because its application to this data set requires circular reasoning, and so proves nothing [99, 100]. The sample amount required by mercury incursion or gas absorption is relatively large, and the self-assembled array on a chip is too delicate for mechanical perturbation. SEM, although convenient, can only produce planar images rather than three dimensional characterizations. Light diffraction pattern is not feasible either because it is challenging to interpret the scattering in the UV or visible light region.

Both the mobility and dispersion coefficient are believed to be affected by multiple factors simultaneously. This feature makes the analysis of the influence of media challenging, because the contribution from other parameters have to be eliminated or separated properly. Several parameters such as field strength, solvent viscosity, buffer pH, ionic strength, and media surface charge, are consistent throughout our experiments. The

temperature gradient is negligible in microchips, and injection and detection bandwidth is eliminated through the data processing.

Factors left could be sorted into two groups: the analyte properties with molecular size, gyration radius and flexibility as examples, and the media properties including pore size distribution, media order, porosity, tortuosity, packing quality, etc. All DNA can be considered as rigid spheres since only the data in the Ogston regime is used. The gyration radius is strongly dependent on DNA size. Thus, the molecular size,  $N$ , could be employed as the major parameter describing the molecule property. As to the media factors, according to the data from both Dodds' model and differential scanning calorimetry as discussed, properties about pore size distribution and accessible volume fraction correlate monotonically with the average pore size  $a(\text{DM})$  from Dodds' model, while the porosity barely changes and the matrix order is characterized by the orientational order parameter,  $\psi$ .

With  $a(\text{DM})$ ,  $N$  and  $\psi$  as major independent variables, the regression of mobility and dispersion coefficient both demonstrate that besides average pore size and molecular size as major determinants, the degree of order is also a considerable factor. The electrophoretic mobility increases, while the dispersion coefficient decreases as the level of order goes up, holding other factors constant. Hence, our study demonstrates that order impacts dispersion, and higher ordered structures are favored because of

greater mobility and less dispersion. This encouraging signal shows DNA separation can be improved further by introducing ordered materials in dense porous matrix.

Our observation is consistent with Slater's simulation in the Ogston regime with a 2D lattice [43] showing the ordered structure has greater mobility, and also support Locke's standpoint [44, 45] that the dispersion coefficient in porous media depends on the obstacle geometry, arrangement and dimension. The conclusion of this chapter is also in accord with our APFE results [38] and Slater's calculations [39] to the extent that disorder is not favorable to DNA separation efficiency, but here no favor is assigned to the short range ordered structure with scattered defects which gave the best efficiency in APFE. Our results contrast with the simulation by Patel and Shaqfeh [40], which suggested disorder was better for separation than order. We partially agree with the model of Mohan and Doyle [26], who concluded that a non-monotonic dependence on order should arise, with short range order providing the best separation. In our monodisperse binary packing, higher  $\psi$  indicates higher short range order. The long range order is limited even in structures in with high  $\psi$  value because of defects and multiple orientation of polycrystalline in long range.

Regarding the difference in separation mechanism in our experimental study versus theoretical analysis, several other issues should be pointed out. As mentioned in the literature [10], the concept of pore size

and the parameter describing order are delicate matters. The pore size used in this article accepts the averaging algorithm similar to hydraulic radius, the ratio between void volume and surface area. However, other average definitions would give different values of the same pore size distribution. People are still arguing that the average itself cannot capture all the properties of the packing, such as tortuosity and pathway complexity, which is believed to be the source of Eddy diffusion. The quantification of order in models were defined as the probability or root mean square of the displacement from a predesigned ordered lattice, different from the parameters used in experimental measure, and the change of order in short range and long range, although correlated, still requires more carefully investigation. Thus observations and theoretical predictions may remain a matter of debate until the media characteristics are unified.

## 4.5 References

1. Sharon, D., R. Chen, and M. Snyder, *Systems biology approaches to disease marker discovery*. Disease Markers, 2010. **28**(4): p. 209-224.
2. Moreno, C., et al., *Comparative genomics for detecting human disease genes*. Genetic Dissection of Complex Traits, 2nd Edition, 2008. **60**: p. 655-697.
3. Michlmayr, A. and R. Oehler, '*OMICS*': *state of the art in vitro techniques employed in surgical research*. European Surgery-Acta Chirurgica Austriaca, 2010. **42**(3): p. 127-133.
4. van't Veer, L.J., et al., *Gene expression profiling predicts clinical outcome of breast cancer*. Nature, 2002. **415**(6871): p. 530-536.
5. Hedenfalk, I., et al., *Gene-expression profiles in hereditary breast cancer*. New England Journal of Medicine, 2001. **344**(8): p. 539-548.

6. Wang, D.J. and S. Bodovitz, *Single cell analysis: the new frontier in 'omics'*. Trends in Biotechnology, 2010. **28**(6): p. 281-290.
7. van den Berg, A., H.G. Craighead, and P.D. Yang, *From microfluidic applications to nanofluidic phenomena*. Chemical Society Reviews, 2010. **39**(3): p. 899-900.
8. Lee, C.C., T.M. Snyder, and S.R. Quake, *A microfluidic oligonucleotide synthesizer*. Nucleic Acids Research, 2010. **38**(8): p. 2514-2521.
9. Wan, F., J. Zhang, and B. Chu, *Advances in electrophoretic techniques for DNA sequencing and oligonucleotide analysis*. Advances in Chromatography, Vol 47, 2009. **47**: p. 59-125.
10. Viovy, J.L., *Electrophoresis of DNA and other polyelectrolytes: Physical mechanisms*. Reviews of Modern Physics, 2000. **72**(3): p. 813-872.
11. Noolandi, J., et al., *Self-trapping and anomalous dispersion of DNA in electrophoresis*. Physical Review Letters, 1987. **58**(23): p. 2428-2431.
12. Slater, G.W. and J. Noolandi, *The biased reptation model of DNA gel-electrophoresis - Mobility vs molecular-size and gel concentration*. Biopolymers, 1989. **28**(10): p. 1781-1791.
13. Zimm, B.H., *Lakes-straits model of field-inversion gel-electrophoresis of DNA*. Journal of Chemical Physics, 1991. **94**(3): p. 2187-2206.
14. Southern, E.M., *Detection of specific sequences among DNA fragments separated by gel-electrophoresis*. Journal of Molecular Biology, 1975. **98**(3): p. 503-517.
15. Panyim, S. and R. Chalkley, *High resolution acrylamide gel electrophoresis of histones*. Archives of Biochemistry and Biophysics, 1969. **130**(1-2): p. 337-346.
16. Loening, U.E., *Fractionation of high-molecular-weight ribonucleic acid by polyacrylamide-gel electrophoresis*. Biochemical Journal, 1967. **102**(1): p. 251-257.
17. Laurell, C.B., *Quantitative estimation of proteins by electrophoresis in agarose gel containing antibodies*. Analytical Biochemistry, 1966. **15**(1): p. 45-52.
18. Peacock, A.C. and C.W. Dingman, *Resolution of multiple ribonucleic acid species by polyacrylamide gel electrophoresis*. Biochemistry, 1967. **6**(6): p. 1818-1827.
19. Schwartz, D.C. and C.R. Cantor, *Separation of yeast chromosome-sized DNAs by pulsed field gradient gel-electrophoresis*. Cell, 1984. **37**(1): p. 67-75.
20. Bustamante, C., S. Gurrieri, and S.B. Smith, *Towards a molecular description of pulsed-field gel-electrophoresis*. Trends in

- Biotechnology, 1993. **11**(1): p. 23-30.
21. Duke, T.A.J., et al., *Pulsed-field electrophoresis in microlithographic arrays*. Electrophoresis, 1996. **17**(6): p. 1075-1079.
  22. Huang, L.R., et al., *A DNA prism for high-speed continuous fractionation of large DNA molecules*. Nature Biotechnology, 2002. **20**(10): p. 1048-1051.
  23. Han, J. and H.G. Craighead, *Separation of long DNA molecules in a microfabricated entropic trap array*. Science, 2000. **288**(5468): p. 1026-1029.
  24. Han, J.Y. and H.G. Craighead, *Characterization and optimization of an entropic trap for DNA separation*. Analytical Chemistry, 2002. **74**(2): p. 394-401.
  25. Levy, S.L., et al., *Entropic Unfolding of DNA Molecules in Nanofluidic Channels*. Nano Letters, 2008. **8**(11): p. 3839-3844.
  26. Doyle, P.S., et al., *Self-assembled magnetic matrices for DNA separation chips*. Science, 2002. **295**(5563): p. 2237-2237.
  27. Minc, N., et al., *Quantitative microfluidic separation of DNA in self-assembled magnetic matrixes*. Analytical Chemistry, 2004. **76**(13): p. 3770-3776.
  28. Kaji, N., et al., *Separation of long DNA molecules by quartz nanopillar chips under a direct current electric field*. Analytical Chemistry, 2004. **76**(1): p. 15-22.
  29. Tabuchi, M., et al., *Nanospheres for DNA separation chips*. Nature Biotechnology, 2004. **22**(3): p. 337-340.
  30. Chou, H.P., et al., *A microfabricated device for sizing and sorting DNA molecules*. Proceedings of the National Academy of Sciences of the United States of America, 1999. **96**(1): p. 11-13.
  31. Margulies, M., et al., *Genome sequencing in microfabricated high-density picolitre reactors*. Nature, 2005. **437**(7057): p. 376-380.
  32. Hopwood, A.J., et al., *Integrated microfluidic system for rapid forensic DNA analysis: sample collection to DNA profile*. Analytical Chemistry, 2010. **82**(16): p. 6991-6999.
  33. Liu, P. and R.A. Mathies, *Integrated microfluidic systems for high-performance genetic analysis*. Trends in Biotechnology, 2009. **27**(10): p. 572-581.
  34. Zeng, Y., et al., *High-performance single cell genetic analysis using microfluidic emulsion generator arrays*. Analytical Chemistry, 2010. **82**(8): p. 3183-3190.
  35. Zhang, H. and M.J. Wirth, *Electromigration of single molecules of DNA in a crystalline array of 300-nm silica colloids*. Analytical Chemistry, 2005. **77**(5): p. 1237-1242.
  36. Zeng, Y. and D.J. Harrison, *Self-assembled colloidal arrays as*

- three-dimensional nanofluidic sieves for separation of biomolecules on microchips*. Analytical Chemistry, 2007. **79**(6): p. 2289-2295.
37. Zeng, Y., M. He, and D.J. Harrison, *Microfluidic self-patterning of large-scale crystalline nanoarrays for high-throughput continuous DNA fractionation*. Angewandte Chemie-International Edition, 2008. **47**(34): p. 6388-6391.
  38. Nazemifard, N., et al., *A systematic evaluation of the role of crystalline order in nanoporous materials on DNA separation*. Lab on a Chip, 2012. **12**(1): p. 146-152.
  39. Hickey, O.A. and G.W. Slater, *The diffusion coefficient of a polymer in an array of obstacles is a non-monotonic function of the degree of disorder in the medium*. Physics Letters A, 2007. **364**(6): p. 448-452.
  40. Patel, P.D. and E.S.G. Shaqfeh, *A computational study of DNA separations in sparse disordered and periodic arrays of posts*. Journal of Chemical Physics, 2003. **118**(6): p. 2941-2951.
  41. Mohan, A. and P.S. Doyle, *Effect of disorder on DNA electrophoresis in a microfluidic array of obstacles*. Physical Review E, 2007. **76**(4).
  42. Park, J., et al., *Fully packed capillary electrochromatographic microchip with self-assembly colloidal silica beads*. Analytical Chemistry, 2007. **79**(8): p. 3214-3219.
  43. Slater, G.W. and H.L. Guo, *An exactly solvable Ogston model of gel electrophoresis .1. The role of the symmetry and randomness of the gel structure*. Electrophoresis, 1996. **17**(6): p. 977-988.
  44. Locke, B.R., *Electrophoretic transport in porous media: A volume-averaging approach*. Industrial & Engineering Chemistry Research, 1998. **37**(2): p. 615-625.
  45. Trinh, S., B.R. Locke, and P. Arce, *Diffusive-convective and diffusive-electroconvective transport in non-uniform channels with application to macromolecular separations*. Separation and Purification Technology, 1999. **15**(3): p. 255-269.
  46. Effenhauser, C.S., et al., *Integrated capillary electrophoresis on flexible silicone microdevices: Analysis of DNA restriction fragments and detection of single DNA molecules on microchips*. Analytical Chemistry, 1997. **69**(17): p. 3451-3457.
  47. Ishikiriyama, K. and M. Todoki, *Pore-size distribution measurements of silica-gels by means of differential scanning calorimetry .2. Thermoporosimetry*. Journal of Colloid and Interface Science, 1995. **171**(1): p. 103-111.
  48. Ishikiriyama, K., M. Todoki, and K. Motomura, *Pore-size distribution (PSD) measurements of silica-gels by means of differential scanning calorimetry .1. Optimization for determination of PSD*. Journal of Colloid and Interface Science, 1995. **171**(1): p.

- 92-102.
49. Bevan, M.A., et al., *Structural evolution of colloidal crystals with increasing ionic strength*. Langmuir, 2004. **20**(17): p. 7045-7052.
  50. Halperin, B.I. and D.R. Nelson, *Theory of 2-dimensional melting*. Physical Review Letters, 1978. **41**(2): p. 121-124.
  51. Aste, T., *Variations around disordered close packing*. Journal of Physics-Condensed Matter, 2005. **17**(24): p. S2361-S2390.
  52. Clarke, A.S. and H. Jonsson, *Structural-changes accompanying densification of random hard-sphere packings*. Physical Review E, 1993. **47**(6): p. 3975-3984.
  53. Dodds, J.A., *The porosity and contact points in multicomponent random sphere packings calculated by a simple statistical geometric model*. Journal of Colloid and Interface Science, 1980. **77**(2): p. 317-327.
  54. Andrade, J.S., *Hydrodynamic dispersion in binary packings of spheres*. Physica A, 1993. **199**(3-4): p. 431-444.
  55. Gibbs, J., *Collected works*. 1928, New Haven, CT: Yale University Press.
  56. Thomson, S.W., *Philosophical Magazine*, 1871. **42**: p. 448.
  57. Jackson, C.L. and G.B. McKenna, *The melting behavior of organic materials confined in porous solids*. Journal of Chemical Physics, 1990. **93**(12): p. 9002-9011.
  58. Ishikiriya, K., et al., *Pore-size distribution measurements of poly(methyl methacrylate) hydrogel membranes for artificial-kidneys using differential scanning calorimetry*. Journal of Colloid and Interface Science, 1995. **173**(2): p. 419-428.
  59. Brun, M., et al., *New method for simultaneous determination of size and shape of pores - Thermoporometry*. Thermochimica Acta, 1977. **21**(1): p. 59-88.
  60. Derouane, E.G., *High resolution nuclear magnetic resonance of adsorbed states .3. Evidence of freezing points and interpretation*. Bulletin Des Societes Chimiques Belges, 1969. **78**(1-2): p. 111-115.
  61. Strange, J.H., M. Rahman, and E.G. Smith, *Characterization of porous solids by NMR*. Physical Review Letters, 1993. **71**(21): p. 3589-3591.
  62. Nedelec, J.M., J.P.E. Grolier, and M. Baba, *Thermoporosimetry: A powerful tool to study the cross-linking in gels networks*. Journal of Sol-Gel Science and Technology, 2006. **40**(2-3): p. 191-200.
  63. Dias, R.P., et al., *Particulate binary mixtures: Dependence of packing porosity on particle size ratio*. Industrial & Engineering Chemistry Research, 2004. **43**(24): p. 7912-7919.
  64. Song, M., K.T. Chuang, and K. Nandakumar, *A theoretical correction of the Ouchiyama and Tanaka formula for predicting*

- average porosity of packed beds consisting of nonuniform spheres.* Industrial & Engineering Chemistry Research, 1998. **37**(8): p. 3490-3496.
65. Hiemenz, P.C., *Principles of Colloid and Surface Chemistry*. 1977, New York: Marcel Dekker.
  66. Stern, O.Z., *Electrochemistry*, 1924. **30**: p. 508.
  67. Napoli, M., J.C.T. Eijkel, and S. Pennathur, *Nanofluidic technology for biomolecule applications: a critical review*. Lab on a Chip, 2010. **10**(8): p. 957-985.
  68. Giddings, J.C., *Unified Separation Science*. 1991, New York: Wiley.
  69. Giddings, J.C., et al., *Statistical Theory for Equilibrium Distribution of Rigid Molecules in Inert Porous Networks . Exclusion Chromatography*. Journal of Physical Chemistry, 1968. **72**(13): p. 4397-4408.
  70. Mercier, J.F. and G.W. Slater, *An exactly solvable Ogston model of gel electrophoresis IV: Sieving through periodic three-dimensional gels*. Electrophoresis, 1998. **19**(10): p. 1560-1565.
  71. Slater, G.W. and H.L. Guo, *An exactly solvable Ogston model of gel electrophoresis .2. Sieving through periodic gels*. Electrophoresis, 1996. **17**(9): p. 1407-1415.
  72. Ogston, A.G., *The spaces in a uniform random suspension of fibres*. Transactions of the Faraday Society, 1958. **54**(11): p. 1754-1757.
  73. Morris, C.J., ed. *Protides of the Biological Fluids*, ed. H. Peeters. Vol. 14t. 1967, Elsevier: New York. 543-551.
  74. Rodbard, D. and Chrambac. A, *Unified theory for gel electrophoresis and gel filtration*. Proceedings of the National Academy of Sciences of the United States of America, 1970. **65**(4): p. 970-977.
  75. Chrambach, A., *The practice of quantitative gel electrophoresis*. 1985, Weinheim: VCH Verlagsgesellschaft.
  76. Butterman, M., et al., *Ferguson plots based on absolute mobilities in polyacrylamide-gel electrophoresis - Dependence of linearity of polymerization conditions and application to the determination of free mobility*. Electrophoresis, 1988. **9**(7): p. 293-298.
  77. Locke, B.R. and S.H. Trinh, *When can the Ogston-Morris-Rodbard-Chrambach model be applied to gel electrophoresis?* Electrophoresis, 1999. **20**(17): p. 3331-3334.
  78. Tietz, D., *Evidence against recent challenges of the extended ogston model*. Electrophoresis, 1995. **16**(3): p. 460-461.
  79. Boileau, J. and G.W. Slater, *An exactly solvable Ogston model of gel electrophoresis - VI. Towards a theory for macromolecules*. Electrophoresis, 2001. **22**(4): p. 673-683.
  80. Mercier, J.F., F. Tessier, and G.W. Slater, *An exactly solvable*

- Ogston model of gel electrophoresis: VIII. Nonconducting gel fibers, curved field lines, and the Nernst-Einstein relation.* Electrophoresis, 2001. **22**(13): p. 2631-2638.
81. Slater, G.W. and H.L. Guo, *Ogston gel-electrophoretic sieving - how is the fractional volume available to a particle related to its mobility and diffusion coefficient(S).* Electrophoresis, 1995. **16**(1): p. 11-15.
  82. Mohanty, U. and N.C. Stellwagen, *Free solution mobility of oligomeric DNA.* Biopolymers, 1999. **49**(3): p. 209-214.
  83. Hoagland, D.A., E. Arvanitidou, and C. Welch, *Capillary electrophoresis measurements of the free solution mobility for several model polyelectrolyte systems.* Macromolecules, 1999. **32**(19): p. 6180-6190.
  84. Ou, J., et al., *DNA electrophoresis in a sparse ordered post array.* Physical Review E, 2009. **79**(6).
  85. Smith, D.E., T.T. Perkins, and S. Chu, *Dynamical scaling of DNA diffusion coefficients.* Macromolecules, 1996. **29**(4): p. 1372-1373.
  86. Doi, M., Edwards, S.F., *The theory of polymer dynamics.* 1986, New York: Oxford University.
  87. Nkodo, A.E., et al., *Diffusion coefficient of DNA molecules during free solution electrophoresis.* Electrophoresis, 2001. **22**(12): p. 2424-2432.
  88. Bednar, J., et al., *Determination of DNA persistence length by cryoelectron microscopy - Separation of the static and dynamic contributions to the apparent persistence length of DNA.* Journal of Molecular Biology, 1995. **254**(4): p. 579-591.
  89. Slater, G.W., P. Mayer, and P.D. Grossman, *Diffusion, joule heating, and band broadening in capillary gel-electrophoresis of DNA.* Electrophoresis, 1995. **16**(1): p. 75-83.
  90. Tinland, B., *Dispersion coefficients of lambda DNA in agarose gels during electrophoresis by fringe recovery after photobleaching.* Electrophoresis, 1996. **17**(10): p. 1519-1523.
  91. Tinland, B., L. Meistermann, and G. Weill, *Simultaneous measurements of mobility, dispersion, and orientation of DNA during steady-field gel electrophoresis coupling a fluorescence recovery after photobleaching apparatus with a fluorescence detected linear dichroism setup.* Physical Review E, 2000. **61**(6): p. 6993-6998.
  92. Mercier, J.F. and G.W. Slater, *Universal interpolating function for the dispersion coefficient of DNA fragments in sieving matrices.* Electrophoresis, 2006. **27**(8): p. 1453-1461.
  93. Long, D. and A. Ajdari, *A note on the screening of hydrodynamic interactions, in electrophoresis, and in porous media.* European Physical Journal E, 2001. **4**(1): p. 29-32.

94. Gibson, T.J. and M.J. Sepaniak, *Examination of band dispersion during size-selective capillary electrophoresis separations of DNA fragments*. Journal of Chromatography B, 1997. **695**(1): p. 103-111.
95. Tsai, D.S. and W. Strieder, *Effective conductivities of random fiber beds*. Chemical Engineering Communications, 1986. **40**(1-6): p. 207-218.
96. Mercier, J.F., G.W. Slater, and H.L. Guo, *Numerically exact diffusion coefficients for lattice systems with periodic boundary conditions. I. Theory*. Journal of Chemical Physics, 1999. **110**(12): p. 6050-6056.
97. Slater, G.W., P. Mayer, and G. Drouin, *Migration of DNA through gels*. High Resolution Separation and Analysis of Biological Macromolecules, Pt A, 1996. **270**: p. 272-295.
98. Stellwagen, E., Y.J. Lu, and N.C. Stellwagen, *Unified description of electrophoresis and diffusion for DNA and other polyions*. Biochemistry, 2003. **42**(40): p. 11745-11750.
99. Chiari, M., et al., *New types of large-pore polyacrylamide-agarose mixed-bed matrices for DNA electrophoresis - Pore-size estimation from ferguson plots of DNA fragments*. Electrophoresis, 1995. **16**(8): p. 1337-1344.
100. Stellwagen, N.C., *Apparent pore size of polyacrylamide gels: Comparison of gels cast and run in Tris-acetate-EDTA and Tris-borate-EDTA buffers*. Electrophoresis, 1998. **19**(10): p. 1542-1547.

# Chapter 5

## Conclusions and Future Work

---

### 5.1 Concluding Remarks

The study presented in this thesis focuses on the analysis and investigation of the separation of DNA molecules in different types of self-assembled nanoparticle arrays and the key parameters affecting separation efficiency in a microfluidic platform. The results demonstrate the flexibility of colloidal self-assembled arrays to produce various separation media with different architectures and pore sizes for a given size range of DNA molecules. The important conclusions based on the work described in this thesis are:

The colloidal self-assembly (CSA) approach is capable of producing crack-free, large scale structures of nanoparticle arrays in a microfluidic chip for DNA separation. Using monodisperse particle suspensions, ordered arrays with pore sizes in nanometers' scale were fabricated, which is much less time and money consuming than conventional nanolithography techniques.

A sequential or step-wise experimental procedure was developed to

fabricate CSA structures with a pore size gradient. Examination by SEM indicated that the gradient is formed by regions of highly-ordered monodisperse arrays with different pore sizes and an interface of several micrometers' width. Gradients in pore size can be created in a size regime as small as tens to a hundred nanometer pores, much smaller than could be readily accomplished using nanolithography of pillars and posts.

The pulsed field electrophoresis of DNA in the gradient CSA arrays showed that optimal separation could be achieved for each DNA size range by taking advantage of both larger and smaller pore sizes within one device. The separation accomplished by the upstream region could then be retained as DNA moves across the zone boundary, even when the molecules have the same deflection angle in the downstream region. The peak capacity can be improved due to the employment of such a pore gradient. Hence, in addition to electric field, frequency and pore size, gradients or steps can be tuned to improve the separation of DNA mixtures with a wide size distribution.

Using the self-assembly approach (CSA), a new experimental procedure was developed to fabricate nanoporous structures with systematically tuned degrees of crystalline order. Using SEM images of the structures, the degree of order was characterized in each structure by a radial distribution function, as well as an orientation order parameter. It was observed that the structures made with monodisperse particle suspensions

have the highest degree of order, while structures made with bidisperse particle suspensions have different degrees of order, depending on the volume fractions of each particle type in the suspension.

The effect of separation media order on two-dimensional DNA pulsed field electrophoresis was investigated. Peak separation distance, band width, and resolution were calculated for different sizes of DNA in structures with different degrees of order. It was observed that all three separation parameters are affected by the degree of order and vary in a non-monotonic fashion with degree of order in separation media. To our knowledge, this is the first experimental evaluation of the effect of order on separation efficiency of DNA pulsed field electrophoresis, indicating that the structure with high short range order but scattered defects in long range yields the highest efficiency.

An important difference between mono and binary packed structures is their pore size distribution. The pore size distribution of monodisperse and binary mixed particle arrays in our one-dimensional capillary zone electrophoresis was characterized by both a theoretical model and differential scanning calorimetry. Both methods produced similar average pore size for mono and binary packed structures, despite approximations such as the close-packing assumption and discrete distribution in the model, and the potential expansion of the lattice by solvent in DSC measurements. More importantly, the average pore size can be used as a representative of

the pore volume distribution because of a high correlation with typical descriptive parameters of the distribution. This result is consistent with gel-based sieving media results.

Capillary zone electrophoresis of DNA in mono and binary packed particle arrays were conducted to examine the effect of order in sieving-based separation. Statistical models were employed to distinguish the influence of the pore size, DNA size and media order. Statistical tests confirmed that the matrix order is a significant contributor to the electrophoretic mobility and the dispersion coefficient. Generally, a higher degree of order is preferred for higher mobility and lower dispersion. This result demonstrates that the degree of order does impact the separation efficiency in capillary zone electrophoresis, and controlling the order with a separation matrix should provide a fruitful means to improve separation performance.

## **5.2 Future Work**

Several suggestions and recommendations are presented here for future research in this field, based on the observations and experience from the study of this thesis.

Chapter 3 and 4 concluded that the matrix order is an important parameter affecting the separation efficiency in both pulsed field electrophoresis and capillary zone electrophoresis of DNA. However, the

mechanism of this effect is still open to question and examination. A complete understanding of the influence of order might be achieved by numerical simulation of the DNA separation process in structures with varying degrees of order. Models were developed for DNA diffusion and separation in sparse array and gel structures, but the sparse array differs significantly from the separation conditions in our experiments. For example, 70% or more of the volume is occupied by particles in our CSA separation media, which is much denser than the sparse arrays or gels used in published experiments or simulations. A simulation more specific to our case might provide an insight into the reasons behind the variation of separation parameters with order.

SEM and thermoporosimetry by DSC were used to investigate the geometry of our particle arrays. SEM, however, could only observe the particles on the top layer or outer surface of the packed beds. The pore size distribution measured by thermoporosimetry is only a bulk property, and we have to consider the potential destructive effect of the repeated heating-cooling cycles. Therefore, more reliable methods are necessary to characterize the three dimensional architecture of the packed media with particles up to hundreds of nanometers' size. It would be ideal if we could prepare CSA arrays with the sample amount required in conventional porosimetry methods such as mercury incursion and gas absorption, and with the stability to survive those methods. The wavelength corresponding

to the scale of the structure lies mostly in the UV range, making the instrumentation challenging for diffraction experiments. Use of a corrosion casting technique might be an interesting alternative: if the void space between particles is filled with monomer solution, after polymerization, the particles could be removed by certain etching reagent. The polymer material left could represent the network of pores, which could be imaged or measured by conventional methods.

All self-assembled arrays were made with unmodified silica particles in this thesis. Since surface chemistry affects the interactions of DNA and particles, it would be worthwhile to investigate arrays of particles with a variety of materials and functional groups. These structures can then be used for separation of DNA and other biomolecules to study the effect of surface chemistry of the porous structures on mobility, conformation, and separation efficiency. Such a study might also help to solve the trapping of large DNA molecules at high electric fields, by tuning the surface property of the separation media.

In our binary packed arrays, the size of the smaller particles is still larger than the threshold required to fill the pores formed by greater particles. In this case, the presence of smaller particles disrupts the ordered packing formed by the larger particles. When the smaller particles are tiny enough to fit into the voids between the larger ones, the order formed by the larger particles is retained and denser structures might be produced,

with significantly decreased pore size. More interestingly, nanoparticles with proper size ratio, shAPFE, and charge might be built to mimic various structures of ionic crystals in meso- or macro-scale. These novel structures may be feasible as a new family of porous matrix needed in separation science and the ionization phase of mass spectrometry.

The success of our microchip to separate a wide range of DNA molecules leads to the prospect of further integration in miniaturized total analysis devices for DNA and other biomolecules. Other modules of DNA analysis, such as polymerase chain reaction (PCR), DNA microarray and DNA sequencing, can be combined with our separation devices to form an integrated DNA analysis microsystem. It has been shown that colloidal self-assemblies can serve as sample pre-concentrators or used in solid phase extraction. Those approaches have the potential to be commercialized for mass production of disposable bioanalytical devices.

# Appendix

## Experimental Setup

---

### A.1 Generating Pulsed Electric Field

Pulsed electric fields were generated across the separation chamber by applying alternating square waves to buffer reservoirs using platinum electrodes as shown in Figure A.1. A four-channel function generator (TGA 1244, Thurlby Thandar Instruments Limited, Cambridgeshire, UK) was used to generate square wave signals. The outputs of the function generator were connected to two lab-made linear voltage amplifiers to form the alternating signals shown in Figure A.1. The outputs of amplifiers were monitored continuously using an oscilloscope with sampling rate of 1 Gs/s (TDS2004C, Tektronics Inc., Beaverton, OR, USA). A negative DC voltage is applied to the injection reservoir to push DNA samples into the separation chamber during separation.

### A.2 Generating a DC Field

DC electric fields were generated by the circuit shown in Figure A.2 and applied to the reservoirs using platinum electrodes.

### A.3 Fluorescent Microscopy

The separation experiments were observed through a fluorescent microscopy build in our lab with epifluorescent (Figure A.3a) and non-epifluorescent setups (Figure A.3b).

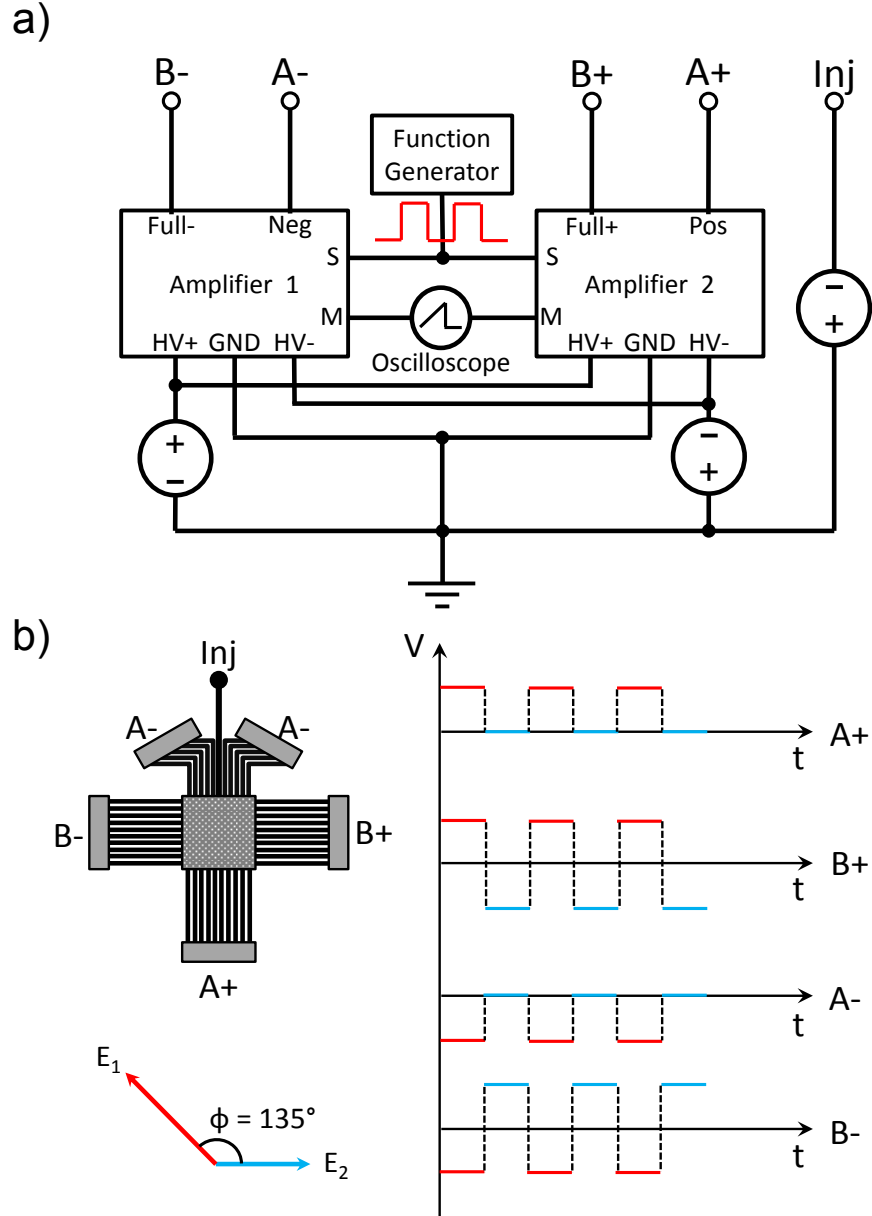


**Figure A.1.** Generation of obtuse angle pulsed electric field across the separation chamber. a) A schematic diagram of the circuit. b) Square wave signals applied to each buffer reservoirs in order to form electric fields in the directions of  $E_1$  and  $E_2$ .

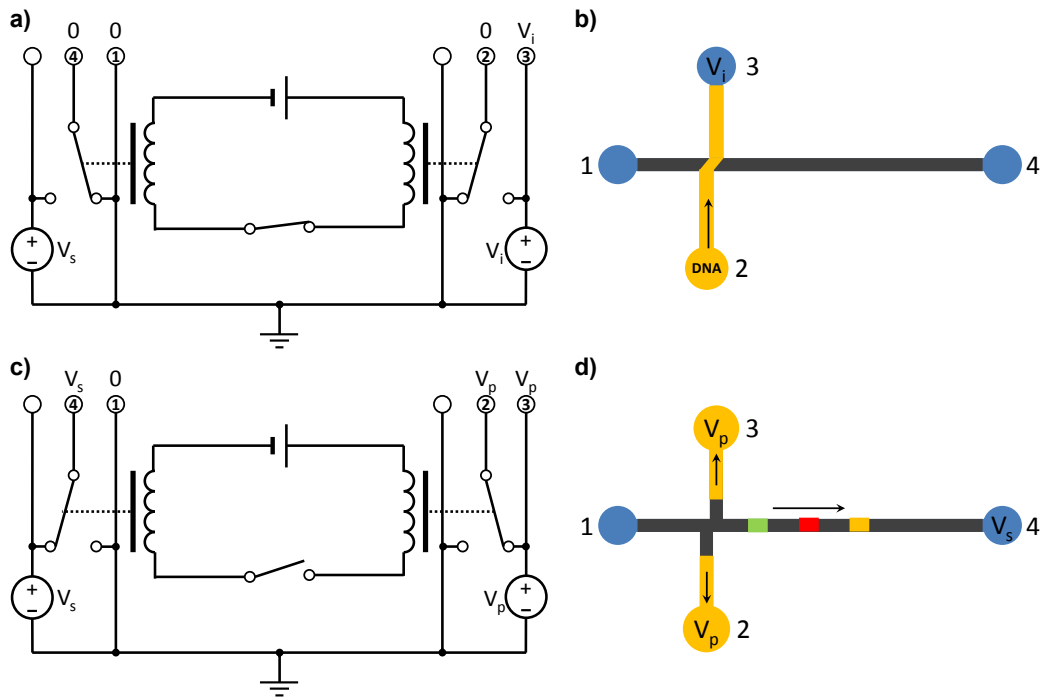


**Figure A.2.** The diagrams of the circuit and the voltage applied for a) b) injection and c) d) separation modes in DNA capillary zone electrophoresis.

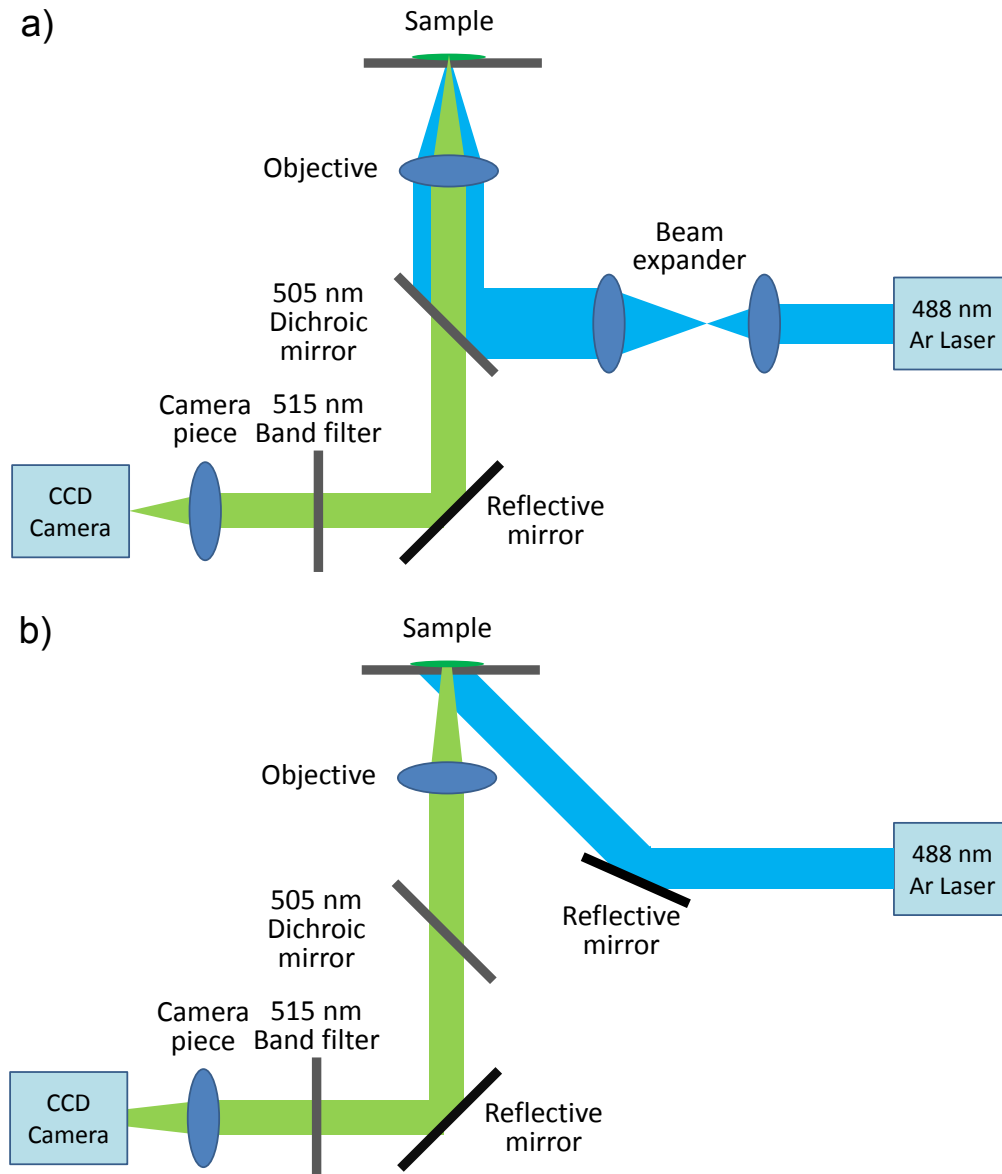


**Figure A.3.** The schematic illustration of the lab-built fluorescent microscopy for imaging under a) epifluorescent and b) non-epifluorescent setups